POSTIRRADIATION EXAMINATION RESULTS FROM THE LP-FP-2 CENTER FUEL MODULE

Steven M. Jensen and Douglas W. Akers
Idaho National Engineering Laboratory
EG&G Idaho
Idaho Falls, Idaho, United States

EGG-M--90152

DE90 012966

ABSTRACT

The LP-FP-2 experiment was conducted on July 9, 1985 in the Loss of Fluid Test (LOFT) facility located at the Idaho National Engineering Laboratory (INEL). The primary purpose of this experiment was to provide information on the release, transport, and deposition of fission products and aerosols during a severe core damage event performed in a large scale nuclear reactor facility. Postirradiation nondestructive and destructive examinations of the fuel bundle provided information to assist in achieving this objective, as well as providing information on the material behavior and interactions that occurred within the fuel bundle during this severe core damage experiment. This was a large-scale integral test, incorporating an 11 X 11 array of fuel rods, control rods, and instrumentation tubes, with an active core length of 1.68 m. Peak temperatures in the fuel bundle exceeded 2100 K for approximately 4.5 min, with localized peak temperatures exceeding the melting point of the UO_2 fuel (3120 K). Large amounts of zircaloy oxidation and material relocation occurred during the experiment. The transient phase was terminated by a rapid reflood of cooling water, which resulted in significant oxidation and hydrogen generation. Zircaloy oxidation during the reflood period caused a rapid temperature excursion to occur in the upper two-thirds of the fuel bundle. This article summarizes the data and analysis from the postirradiation examinations of the LP-FP-2 fuel bundle.

DISCLAIMER

I. Introduction

Following the successful completion of the LP-FP-2 experiment it was decided to perform postirradiation examinations of the fuel bundle to provide additional information to assist in determining the factors that may have influenced the thermal-hydraulic and fission product behavior. These postirradiation examinations also expanded the scope of this experiment to include material behavior and interactions occurring within a fuel bundle during a severe core accident. Due to the size of the LP-FP-2 fuel assembly, the results from these examinations provided an important link between smaller-scale severe fuel damage experiments [1,2,3,4] and the Three Mile Island accident [5].

The objectives of the postirradiation examinations were to provide data on 1) the final distribution of fuel and control rod materials; 2) the posttest metallurgical and chemical form of materials; 3) the maximum temperatures achieved as a function of position in the fuel bundle; and 4) to determine the fission product distribution in both fueled and nonfueled materials. This article summarizes the data which was obtained to successfully meet all these objectives.

A schematic cross-section through the LP-FP-2 fuel bundle is shown in Figure 1. The fuel assembly consisted of 100 UO_2 fuel rods with zircaloy cladding, eleven (Ag,In,Cd) control rods with stainless steel cladding surrounded by zircaloy guide tubes, six empty zircaloy guide tubes, and various instrumentation tubes. ZrO_2 insulation was sandwiched between a zircaloy inner liner and the zircaloy outer shroud. The fuel was 9.74 wt.% enriched and 94.7% of theoretical density. Additional fabrication details are provided elsewhere [6].

Both nondestructive and destructive examinations of the center fuel bundle were performed. The nondestructive examinations included visual examinations of the exterior surface, gross and isotopic gamma scans of the overall fuel bundle, and neutron radiographs at two perpendicular orientations through the fuel bundle. The fuel bundle was then sectioned to provide 21 transverse cross-sectional surfaces. These were quartered and polished to provide 84 samples for examination and photography, of which 42 samples were examined in detail on the metallograph. Approximately thirty small core bore samples were obtained from these metallographic samples for scanning electron microscope/wavelength dispersive spectroscopic examination, as well as elemental and radiochemical analyses.

This article summarizes the major results from these postirradiation examinations. Additional detailed information are provided elsewhere [6]. Related information on other aspects of this experiment are also provided elsewhere [7,8,9,10], as are comparisons of the LP-FP-2 results with other severe core damage integral tests [11].

II. Qualitative Analysis

This section describes in general the overall condition of the LP-FP-2 fuel bundle following irradiation. This description is primarily based upon visual examinations, gross and isotopic gamma scans, neutron

radiography, and representative metallographic cross sections through the fuel bundle. This is followed by descriptions of specific types of material behavior, such as control rod behavior, zircaloy and fuel behavior, melt behavior, etc. These descriptions are based primarily upon the detailed metallography and SEM/WDS examinations.

2.1 Visual Examinations

The LP-FP-2 fuel module was vertically lifted out of its underwater storage location in the TAN water pit for visual examinations in January 1986. A photograph of the fuel bundle portion is shown in Figure 2 (the upper support structure above the upper end box is not visible). The fuel bundle was slightly discolored, and slight oxidation of the zircaloy shroud was apparent in the area slightly above core midplane. A portion of the shroud in the northeast corner had cracked and broken off, exposing the ZrO_2 insulation layer. It is not clear whether the broken shroud occurred during irradiation, or whether it occurred after the test when the module was removed from the reactor and transported to the TAN water pit.

Figure 3 shows ceramic debris which were observed in the upper end box. Subsequent analyses indicated these were fuel and melt particles which were blown upward by the large amount of steam generated during the reflood stage.

Examinations of the bottom of the fuel module indicated that no material had relocated out the bottom.

2.2 Gross and Isotopic Gamma Scans

Gross and isotopic gamma scans of the LP-FP-2 fuel bundle were conducted in September 1986 to provide some early insights into the posttest internal condition of the fuel bundle. As such, many of the conclusions and observations from these examinations [6] were supported by subsequent examinations or the reasons for observed behavior are now better understood. As a result, only two particularly pertinent facts from these examinations are discussed here.

Significant amounts of material were no longer present on the upper portion of the bundle on the eastern side. This was later observed in the neutron radiographs and the metallographic cross sections, but the significance is that the module was always in the vertical position until after the gamma scans were completed. It had to be laid horizontal prior to neutron radiography and sectioning. This indicates that fuel handling did not significantly affect the posttest distribution of material in the fuel bundle.

Only a small fraction of the total fission product bundle inventory was released and deposited in the upper support structure above the fuel bundle.

2.3 Neutron Radiography

Neutron radiography was performed at ANL-W in September 1987 at two perpendicular orientations over the entire fuel bundle and a portion of the

upper support structure. These neutron radiographs are shown in Figures 4 and 5. The north and east orientations can be referenced to Figure 1 and refer to that face which the neutron beam first intercepted on its passage through the fuel module. The east face is therefore on the left side of the north-face view. Axial elevations in the neutron radiographs are referenced from the bottom of the 25 instrumented fuel rods, which were 0.1 m above the bottom of the fuel module. The bottom of the instrumented fuel rods was 2.54 cm above the bottom of the 75 uninstrumented fuel rods. This reference system is used throughout this article.

Six distinctive regions were identified from the radiographs, and representative metallographic cross sections are used in the following discussion to illustrate these various regions.

Region 1 (<0.1 m)

The region below approximately 0.1 m encompasses the bottom spacer grid and below. The material in this region was intact and only minor amounts of control rod droplets had relocated and solidified in this region. A representative quarter section of the transverse section through the lower spacer grid is shown in Figure 6. Some of the insulation on this sample, and other samples from the lower half of the fuel bundle, fell out during bundle sectioning and handling of the samples. It is known to have been intact because the inner liner was still intact in these regions, and the neutron radiographs showed the insulation to be intact prior to sectioning.

Region 2 (~0.1-0.23 m)

Relocated material solidified in the region above the bottom spacer grid, forming a large blockage from approximately 0.1 - 0.23 m. This blockage was composed of metallic melts and small fuel debris. The metallic melts were primarily composed of Ag-Zr, with smaller amounts of iron, chromium, and nickel mixed in. A representative quarter section through this blockage region is shown in Figure 7. The relocated material was generally not hot enough to damage the rods in this region, with the exception of a few rods near the center of the bundle.

Region 3 (~0.23-0.44 m)

The rod array was essentially intact throughout this region, with only small amounts of metallic melt between the rods. Only two fuel rods near the center of the fuel bundle had failed. A representative quarter section is shown in Figure 8.

Region 4 (~0.44-0.85 m)

Relocating material resulted in the formation of a large blockage throughout this region. The second spacer grid was at the lower extent of this blockage region, and metallic melt and fuel debris much like that found in the lower blockage region had accumulated on this spacer grid. However, unlike the situation at the lower spacer grid, the relocated material at this spacer grid was hot enough to cause significant liquefaction as a result of Ni-Zr eutectic interactions. A representative quarter section through the second spacer grid is shown in Figure 9. The spacer grids impeded material relocation, and as discussed in Section 3.1.8, the largest flow blockages were located through, or just above, the two remaining spacer grids.

Above the second spacer grid the relocated material was composed of high temperature $(U,Zr)O_2$ ceramic melt. The full cross section through the middle of this ceramic blockage region is shown in Figure 10. The ceramic melt surrounded the remaining fuel rod remnants, except in the central region where temperatures were sufficient to completely melt the fuel and oxidized cladding (>3120 K). Temperatures in this region are discussed in more detail in Section 3.3, but the metallographic evidence indicates a temperature gradient existed, with lower temperatures towards the periphery of this ceramic melt region. This suggests the formation of a solidified crust of $(U,Zr)O_2$ surrounding a central pool of molten $(U,Zr)O_2$, much like what occurred during the TMI-2 accident [5].

In the region above the second spacer grid the inner liner was completely liquefied and melt was able to penetrate into the insulation. Zircaloy oxidation also became significant above this elevation, and essentially all the remaining zircaloy at and above 0.66 m was completely oxidized. Cladding ballooning and rupture also became significant above the second spacer grid, reflecting the increased cladding temperatures associated with zircaloy oxidation. At and above the 0.58 m elevation all the control rods had completely failed, releasing all the (Ag,In,Cd) control material above this location.

Region 5 (~0.85-1.15 m)

The rod array in this region above the upper blockage exhibited extensive cladding ballooning and rupture. Rod to rod contact and fusion of oxidized cladding remnants was observed. Relocated $(U,Zr)O_2$ ceramic melt surrounded some of the fuel rods and partially blocked the flow channels. A representative quarter section is shown in Figure 11.

Region 6 (~1.15-1.70 m)

This region consisted primarily of a rubble bed of fuel pellets without any intact cladding to restrain them. Ceramic melts, from molten zircaloy cladding and the upper tie plate, had flowed down around the fuel debris. A lot of material was missing on the eastern side of the fuel module, including much of the insulation. Some fuel pellet stacks (without any intact cladding) remained intact on the western side of the module. As described in Section 2.2, comparison of the gamma scan results with the observed material distribution indicates that posttest handling did not affect the posttest configuration within the module; the solidified ceramic melt held the fuel debris in place. A representative quarter section through this region is shown in Figure 12.

Upper End Box Region (~1.8 m)

Relocated material was observed in the upper end box during both the visual examinations and in the subsequent neutron radiographs. Figure 13 shows a representative quarter section through the middle of the stainless steel upper tie plate. The upper tie plate was only intact on the periphery of the bundle; in the center it had liquefied and oxidized. Intact fuel pellet fragments were also observed in this area. As described in more detail elsewhere [7,8], the liquefaction and oxidation of the upper tie plate, and the relocation of melt and fuel debris to this region, could only have occurred during the reflood period. During the transient the

temperatures and steam mass flow rates were too low to account for the observed behavior, but during the reflood period both the temperature and steam mass flow rates increased dramatically.

2.4 Qualitative Material Descriptions

This section discusses the behavior of specific categories of materials.

2.4.1 Spacer Grids

The LP-FP-2 fuel module contained five Inconel 718 spacer grids. Only the bottom spacer grid was still completely intact at the completion of the experiment. The second highest spacer grid was partially intact, and the other three spacer grids had completely liquefied. Relocating material accumulated at the second spacer grid, which suggests that the spacer grids served as traps for relocating material until they ultimately failed. Both of the large blockage regions were located just above the two remaining spacer grids. Representative photographs of the two remaining spacer grids were presented in Figures 6 and 9.

A typical interaction between melts and the spacer grids is shown in Figure 14. SEM/WDS examinations of similar areas revealed the presence of a Zr-Nb phase along the grain boundaries of the intact spacer grid. The previously molten region adjacent to the intact spacer grid was a complex mixture of zircaloy components (Zr,Sn), interacting with the Inconel components (Ni,Fe,Cr,Nb,Mo,Ti), with small amounts of silver from the control rods.

As shown in the Figures 15 and 16, the Zr-Ni and Zr-Fe phase diagrams indicate that liquid phases between these elements can form at temperatures as low as 1220-1233 K. A series of eutectic melts can also form between Zr and Ni over wide compositional ranges at temperatures between 1233 and 1443 K. Since the majority of Inconel 718 is nickel (~50 wt.%), this suggests that rapid liquefaction of the spacer grids can be expected at temperatures of approximately 1400-1500 K, well below the 1720-K melting point of Inconel 718. This is consistent with the SEM/WDS examinations which show zirconium interacting with the Inconel to form eutectic and multiphase compounds.

2.4.2 Control Rod Behavior

The LP-FP-2 experiment utilized eleven (Ag,In,Cd) control rods. These rods used 304 stainless steel cladding, and each was contained within a zircaloy guide tube. All the control rods were intact at the second spacer grid elevation (0.46 m), but all had failed at the next elevation examined (0.58 m). Approximately 70% of the available control material (10 kg) was therefore released to the bundle either as an aerosol spray when the cladding initially failed, or later as a melt. Approximately 8 kg of silver were therefore available to interact with other bundle constituents. The Ag-Zr phase diagram shown in Figure 17 indicates that silver can dissolve up to 67 at.% zirconium above 1400 K, and that eutectic phases can form as low at approximately 1200 K. This indicates that silver would be expected to liquefy the zircaloy cladding at temperatures well below the

2030 K melting point of zircaloy. As described in Section 2.4.4, the accumulation of large amounts of Ag-Zr bearing melts in the lower region of the bundle indicates this liquefaction process resulted in significant amounts of early material relocation in LP-FP-2.

Figure 18 shows molten (Ag,In,Cd) control material contained within the partially liquefied remains of its stainless steel cladding. Examination of the cladding inner surface indicates that the molten control material did not interact with the cladding. However, metallic melts which flowed down the exterior of the cladding did interact with the stainless steel. An intergranular interaction zone is apparent on the outer surface of the cladding, and the liquefaction of the stainless steel has resulted in the formation of a eutectic melt structure. SEM/WDS examinations of this area revealed the presence of low melting point Zr-Ni intermetallic phases along the grain boundaries. The eutectic melt structure was also composed primarily of zirconium and nickel, with smaller amounts of iron and chromium mixed in. This behavior is consistent with the Zr-Ni phase diagram shown in Figure 15, indicating that zirconium bearing melts were responsible for the liquefaction of the stainless steel cladding.

Another example of melt interactions with stainless steel cladding is shown in Figure 19. SEM/WDS examinations of this area revealed a Zr-Ni intergranular interaction zone and eutectic melts similar to the previous example. However, these photographs also show the multiphase metallic melt structure breaking apart in a laminar structure. Similar laminar structures were observed in the lower blockage region, indicating that some of the material in the lower blockage formed in this manner.

2.4.3 Zircaloy Behavior

At the bottom of the fuel module the zircaloy cladding was in the as-fabricated condition, but recrystallized zircaloy was apparent at and above the 0.12 m elevation. The presence of recrystallized zircaloy indicates temperatures in excess of 925 K. Minor amounts (<100 ppm) of zirconium hydrides were also observed in the recrystallized regions. At higher elevations (0.27-0.58 m) prior-beta zircaloy structure was present, indicating temperatures in excess of 1245 K. At and above the 0.66 m elevation essentially all the remaining zircaloy cladding was fully oxidized to ZrO_2 (the only unoxidized zircaloy was on a few rods in one corner near the very top of the fuel bundle). Minor amounts of zircaloy oxidation were observed below the 0.66 m elevation on the surface of some of the fuel rods and guide tubes. The lowest extent was on some of the centrally located fuel rods at the 0.12 m elevation.

Cladding ballooning and rupture became significant above the second spacer grid. The oxidized cladding shells in this region came into contact and fused together in many instances. Examples of this phenomenon are apparent in Figures 10 and 11. The axial transition in the degree of cladding ballooning was associated with a transition in the amount of zircaloy oxidation. This suggests that the exothermic zircaloy oxidation process caused cladding temperatures to increase and resulted in enhanced ballooning and rupture in these regions of the pressurized fuel rods.

At and above the 0.58 m elevation, fully oxidized cladding shells were all that remained of the zircaloy. An example is shown in Figure 20. During the transient the outer surface of the cladding fully oxidized to ZrO_2, which melts at 2960 K. Under this was a layer of partially oxidized alpha-Zr(O), which melts at approximately 2245 K, and beneath this was the unoxidized zircaloy which melts at 2030 K. As temperatures in the bundle increased, primarily as a result of the exothermic zircaloy oxidation process, the unoxidized zircaloy on the cladding inner surface melted and was able to flow downward. This melt was observed on lower cross sections filling the fuel/cladding gap and penetrating along cracks in the fuel. This molten zircaloy was also able to escape from ruptured portions of the fuel rods.

In regions where the zircaloy cladding was not completely oxidized, relocating metallic melts containing silver were able to interact with the cladding and cause liquefaction below the melting point of the zircaloy. An example of this is shown in Figure 21 at the 0.43 m elevation just below the second spacer grid. This figure shows the formation of the laminar type eutectic structures observed in the lower blockage region. These Ag-Zr laminar structures from zircaloy/melt interactions appear very similar to the Zr-Ni-Fe-Cr laminar melt structures from stainless steel/melt interactions shown in Figure 19, and suggest that both of these interactions were responsible for the early relocation of materials.

The zircaloy inner liner remained intact up through the 0.46 m elevation, but was partially liquefied at the 0.58 m elevation and completely gone at above the 0.66 m elevation. The molten liner and other metallic melts were able to penetrate into the insulation in these regions.

Examinations of the zircaloy shroud indicated only intermittent small oxide layers in the hotter regions near core midplane. Prior-beta zircaloy was observed in the region from 0.77-1.14 m, indicating temperatures in excess of 1245 K. This agrees with peak thermocouple measurements of 1620 K in this region [9]. Examination of the cracked region of the shroud did not reveal any unusual features or evidence of overtemperature conditions.

2.4.4 Behavior in the Lower Blockage Region

The material in the lower blockage region was primarily composed of Ag-Zr-Fe-Cr-Ni metallic melt and fuel debris. Small amounts of oxidized cladding remnants and other metallic melts were also present. A representative photograph of the material is shown in Figure 22, and in more detail in Figure 23. The eutectic metallic melt in this region is very similar to that shown in Figures 19 and 21, which indicates that it resulted from liquefaction of zircaloy, stainless steel, and Inconel. Some laminar melt structure can also be seen separating from the liquefied portion of the zircaloy cladding in Figure 22.

This lower blockage region solidified in an egg-shaped form with a central cavity region containing only the intact fuel rods. There was extensive porosity between the individual particles on a microscopic scale

(as shown in Figure 23), however it was sufficiently agglomerated that the epoxy which was initially poured into the bundle was unable to penetrate into the central cavity region.

2.4.5 Ceramic Melt Behavior

Ceramic melt was not located below the second spacer grid. Most of the $(U,Zr)O_2$ ceramic melt solidified in a large mass to form an upper blockage which extended from approximately 0.58-0.88 m. SEM/WDS quantitative analysis confirmed that the ceramic melt was fully oxidized $(U,Zr)O_2$. $(U,Zr)O_2$ melt was also present around individual rods and fuel debris above the upper blockage. Near the top of the bundle, some of the ceramic melt contained oxidized melt from the stainless steel upper tie plate in addition to $(U,Zr)O_2$.

A representative photograph of the typical ceramic melt structure is shown in Figure 24. It was glassy in appearance with some cracking and porosity. In this photograph the $(U,Zr)O_2$ melt was hot enough to melt the oxidized cladding on one side of the fuel pellet, but not quite hot enough to completely dissolve all the oxidized cladding remnants on the other side of the pellet. Molten $(U,Zr)O_2$ requires temperatures in excess of 2810 K, with temperatures above 2960 K to melt oxidized ZrO_2 cladding. Temperatures were less than the 3120 K required to melt the UO_2 fuel. The melt penetrated along cracks in the fuel and some grain growth in the center of the fuel pellet is apparent.

2.4.6 Fuel Behavior

Several factors affected the behavior of the fuel in the LP-FP-2 experiment. The different aspects of fuel behavior are divided into four categories: (1) grain size, (2) fuel reduction by metallic melts, (3) fuel fragmentation and powdering, (4) fuel liquefaction and melting.

2.4.6.1 Grain size

The nominal as-fabricated fuel grain size was 14 mm. A total of 107 measurements were made in typically representative fuel over the entire axial length of the fuel assembly. These measurements indicated an average grain size of 14 mm, with a 2-sigma standard deviation of $\pm$ 4 mm, indicating that grain growth did not occur in the majority of the fuel. However, grain growth was observed in the center of some of the fuel pellets in the hotter portions of the bundle. Thirty measurements in these grain growth regions indicated an average grain size of 27 mm, with a 2-sigma standard deviation of 17 mm.

2.4.6.2 Fuel reduction by metallic melts

Areas of enhanced grain boundary separation and fragmentation were associated with the presence of metallic melts. Examples of this phenomenon are shown in Figure 25, which shows the affected fuel adjacent to metallic melts which had penetrated along cracks in the fuel. There was evidence that this phenomenon was not simply a thermal effect, because in some instances where ceramic and metallic melts were both in contact with

the fuel, the grain boundary separation was limited to the areas near the metallic melt. An example is shown in Figures 26. This may be due to reduction of the fuel by the zirconium bearing metallic melts, resulting in slightly hypostochiometric fuel along the adjacent grain boundaries. As shown in the U-O phase diagram in Figure 27, this could result in the formation of a uranium-rich liquid phase along the grain boundaries at temperatures above approximately 1470 K. The presence of such a film could result in grain boundary separation and fragmentation, and similar dissolution and breakup of the fuel has been previously observed [12]. In that instance, molten zircaloy contained in a UO_2 crucible resulted in partial disintegration of the crucible. However, any metallic uranium that may have formed on the grain boundaries in LP-FP-2 as a result of this process would have oxidized to UO_2 by the time this sample was prepared and examined and be indistinguishable from the rest of the fuel.

Several SEM/WDS samples were examined to investigate this phenomenon. No second phase material was ever found in the separated grain boundary regions. These examinations did show that the melt was indeed metallic (low in oxygen), that the melt contained significant amounts of zirconium (the only major bundle constituent capable of reducing the fuel), and that uranium was segregated in the melt. These results are consistent with fuel reduction. In all cases the metallic melt did not penetrate into the grain boundary separation regions, which indicates that the melt solidified before the grain boundary separation occurred.

2.4.6.3 Fuel Fragmentation and Powdering

Fuel fragmentation and powdering (the breakup of fuel into individual grains) was observed throughout the LP-FP-2 fuel assembly on failed fuel rods that were exposed to water during reflood. An example is shown in Figure 28. It was not observed on intact portions of fuel rods (in the lower portion of the bundle) or fuel rods that were completely surrounded by melt material that restrained the fuel. This suggests that the thermal shock to the fuel during reflood contributed to breakup of the fuel, however fuel fragmentation and powdering also occurred prior to reflood because fuel debris was intermixed with the melt material in the lower blockage. Fuel fragmentation and powdering would have been particularly susceptible in fuel which had experienced grain boundary separation.

2.4.6.4 Fuel Liquefaction and Melting

Areas of fuel with a foamy morphology were observed on the periphery of some fuel pellets in the midcore region and above. An example of this behavior is shown in Figure 29. It shows that on the outer periphery of the foamy fuel region the grain structure was obliterated, whereas farther inward a grain structure was still apparent in the foamy fuel. Elemental dot maps from SEM/WDS examinations of a similar sample indicated the presence of iron, chromium, and nickel in the fuel. Review of U-Fe-O phase diagrams indicates that eutectic interactions can take place between these materials, although the data is very limited, which suggests that the observed foamy fuel morphology may be due to fuel liquefaction by iron-oxides.

The foamy fuel regions discussed above were no longer surrounded by any molten material. However, porous fuel regions were also observed on some fuel pellets in the high temperature upper blockage region which were surrounded by $(U,Zr)O_2$ ceramic melt. An example of this behavior is shown in Figure 30. Elemental dot maps from SEM/WDS examinations of a similar area indicated that these porous fuel regions did not contain any iron oxides or other elements. This suggests temperatures very near the 3120 K melting point of the fuel, and the lack of oxidized ZrO_2 cladding shells in these regions further indicates temperatures above the 2960 K melting point of ZrO_2. This behavior was observed on many of the fuel pellets in the center of the ceramic upper blockage region, and was a prime indicator of melt temperatures in this region as discussed in Section 3.3.

III. Quantitative Data Analyses

This section discusses the flow blockage and material redistribution measurements, estimation of the oxidation and hydrogen generation, peak bundle temperatures, and the results from the radiochemical and elemental analyses of the retained fission product samples.

3.1 Flow Blockage and Material Redistribution

The cross-sectional areas of various types of materials at each metallographic elevation were measured to provide axial distributions. Interpolation of these values provided integral volumes of materials. Density and elemental analyses of bulk samples were then used to estimate material compositions in the melt regions, and to calculate material balances for uranium and zirconium. Details of the measurement techniques and uncertainties are described elsewhere [6], however in general the uncertainties were <15%.

3.1.1 Intact and Fragmented Fuel

For these purposes, the term intact fuel refers to fuel pieces of sufficient size that they could be accurately characterized; generally on the order of 1/4 to 1/8 the size of a fuel pellet. As used here, this term is not meant to infer that the fuel was not cracked or fragmented; it is only meant to describe a categorical type of material observed metallographically. Fuel fragments refers to a category of material consisting of fuel particles which were too small to accurately reproduce using manual planimetry techniques. This category generally consisted of an agglomeration of very small fuel particles which could not be individually distinguished from the cross-sectional photographs. However, higher magnification photographs showed significant amounts of open porosity separating the individual particles, and consequently the measured cross-sectional areas for these areas were reduced in half, and the remainder was added to the measured open flow values.

The axial distribution of intact and fragmented fuel is shown in Figure 31, as well as the as-fabricated values. Below the second spacer grid the fuel was essentially intact (the bottom two elevations passed through the endcaps of the instrumented fuel rods). Above the second spacer grid (0.58 m), in the region near the bottom of the large ceramic melt region, a lot of the fuel was not surrounded by any relocated melt material. Cladding

ballooning and rupture in this region left the exposed fuel unrestrained and susceptible to fragmentation. Above this region (0.58-0.88 m) there was very little fragmented fuel; most of the fuel rods were surrounded by the ceramic melt which held them in place. Above the upper blockage region, the array of ballooned and ruptured fuel rods was held together by cladding remnants and ceramic melt which surrounded the individual rods and minimized fuel fragmentation. However, above this region the cladding had been completely stripped from the fuel, allowing a debris bed of intact and fragmented fuel particles to form. The fuel from the upper portions of the bundle relocated downward and congregated on top of the remaining rod stubs.

3.1.2 Zircaloy

Zircaloy components included fuel rod cladding, guide tubes, lock rings surrounding the guide tubes at spacer grid locations, and the zircaloy inner liner. The posttest axial distribution of these components is shown in Figure 32, along with the as-fabricated values.

The zircaloy cladding, guide tubes, and lock rings were essentially intact below the second spacer grid. Melting of the cladding inner surface and fragmentation of the oxidized cladding shells accounted for the decrease in the amount of zircaloy above the second spacer grid. At and above the 0.66 m elevation all of the zircaloy was fully oxidized to ZrO_2, except for a minor amount at the 1.45 m elevation. Very little zircaloy remained in the high temperature ceramic melt region (0.58-0.85 m), or in the uppermost region of the bundle, however a significant amount of oxidized cladding surrounded rod stubs in the region between the upper blockage and the debris bed (0.96-1.14 m).

The inner liner, which separated the rod array from the insulation region, was also intact below the second spacer grid, but was completely liquefied at and above the 0.66 m elevation except for a minor amount in one corner at the 1.45 m elevation (the same region a minor amount of unoxidized zircaloy was located).

3.1.3 Control Rod Materials

The posttest distribution of (Ag,In,Cd) control rod alloy contained in its stainless steel cladding is shown in Figure 33. The stainless steel cladding was generally intact below the second spacer grid, with partial liquefaction occurring near the second spacer grid. Release of all the control material from all eleven control rods occurred between the 0.46 and 0.58 m elevations.

3.1.4 Insulation

It was necessary to measure the amount of insulation present at each elevation because the inner liner had melted in the upper portion of the fuel bundle and the insulation was able to fall out and relocate into the fueled portion of the bundle. This significantly affected the open flow distribution in the upper portion of the bundle. Melt was also able to penetrate into the low-density (~20%) ZrO_2 insulation where the inner liner had melted. The amount of this melt material had to be accounted for in

the zirconium mass balance estimates for the bundle, and for subsequent estimates of the amount of zircaloy oxidation in the bundle. As described below, the distribution of the melt penetration into the insulation also provides some insight into the sequence of events which occurred during this experiment.

The data for the intact insulation (area unaffected by melt penetration) and the melt/insulation areas are shown in Figure 34. These data show that all the insulation was intact and unaffected by any melt below the second spacer grid; in the regions where the inner liner remained intact. Melt penetration into the insulation occurred throughout the central portion of the fuel bundle, with the greatest amount in the region above the ceramic melt blockage. Only very minor amounts were observed in the topmost regions of the bundle. A possible explanation for this behavior may be that the inner surface of the inner liner was oxidized in the central portion of the bundle, much like the outer surface of the fuel rod cladding in this region. As temperatures increased, the oxide layer on the inner liner would have subsequently held molten unoxidized zircaloy adjacent to the insulation and allowed the melt to penetrate into the insulation. This is analogous to melting of the unoxidized inner surface of the fuel rod cladding. The upper extent to the melt penetration into the insulation also corresponds to the upper extent of oxidized cladding remnants (see Figure 32). The oxidized cladding remnants at these upper elevations were also limited to exterior positions, near the inner liner, which suggests that the steam was diverted to these exterior bundle positions after one or both of the blockages had formed. These data all suggest that the upper extent to zircaloy oxidation of intact rods and liner was near the 1.2 m elevation. Above this elevation the zircaloy cladding and liner was liquefied and relocated before an oxide layer could develop. This liquefaction would have started on the inner surface of the inner liner, and hence melt would not be held against the insulation and have an opportunity to penetrate into the insulation. This liquefaction probably resulted from dissolution of the zircaloy by silver released upon control rod failure, and later perhaps by simple melting of the unoxidized zircaloy.

3.1.5 Ceramic Melt

The majority of the ceramic melt in the LP-FP-2 fuel module was composed of $(U,Zr)O_2$, with relatively small amounts of bundle constituents mixed in. The exception was near the top of the fuel bundle, where the stainless steel upper tie plate had melted, relocated, and oxidized. The material distribution data for the ceramic melt are shown in Figure 35. The melt was only found above the second spacer grid, with the greatest accumulation between approximately 0.66-0.88 m. In this region the melt formed a large solidified mass, whereas above this the melt was limited to isolated regions around the remaining rod stubs and fuel debris.

3.1.6 Eutectic Metallic Melt/Fuel Debris

This material was primarily composed of an agglomeration of very small eutectic metallic melt particles (primarily Ag,In,Zr,Fe,Cr, and Ni), fuel grains and fragments, and small amounts of other assorted fuel bundle debris (cladding remnants, larger metallic melt droplets, and fuel

fragments). On a microscopic scale, there was also considerable porosity between the particles. As shown in Figure 36, this material formed the lower blockage region just above the bottom spacer grid, and it also accumulated on the second spacer grid.

3.1.7 Metallic Melts

Most, if not all, the metallic melts at and below the second spacer grid consisted of droplets of (Ag,In,Cd) control rod alloy. Above this elevation the majority of the metallic melts consisted of multiphase elemental mixtures. As shown in Figure 37, the amount of these melts was relatively small and their distribution was very irregular throughout the fuel bundle. The large increase in metallic melt near the top of the fuel bundle is due to metallic melts relocating from the upper tie plate and other portions of the upper end box.

3.1.8 Open Flow

The measured open flow axial distribution is shown in Figure 38. Near the bottom of the fuel module was the lower blockage region consisting primarily of eutectic metallic melt/fuel debris. The solid line in this region is based solely on the material present, whereas the dotted line takes into account the fact that there was a cavity region within the lower blockage which steam did not have access to. The flow impedance in this region corresponds to 86% of the area within the inner liner, assuming that steam was diverted around the lower blockage.

The second greatest flow impedance was through the second spacer grid and corresponded to 78% of the area within the inner liner. The reduction in open flow due to the presence of the large solidified ceramic melt can be seen in the region from 0.58-0.88 m. Above this ceramic melt region the open flow increased; the region consisted of ballooned and ruptured rod stubs surrounded by small amounts of ceramic melt. The decrease in open flow at 1.2 m was due to fuel debris resting on top of the rod stubs, and the increase in open flow above this reflects the loss of material from this region.

Integration of the as-fabricated and posttest open flow measurement data indicates an 11% reduction in the open flow volume (using the solid line in Figure 38). This corresponds to a 15% volume expansion of the material initially contained within the inner liner. This is a result of the porosity within the various melt regions. The reduction in the open flow volume is 12%, if it is assumed that steam was diverted around the lower blockage (using the dotted line in Figure 38).

3.1.9 Integral Material Distribution Data

Interpolation of the cross-sectional measurement data provided integral volumes of material in the bundle. These data are provided in Tables 1 and 2, along with upper and lower limits based on the uncertainties in the measurement data. These limits assumed that all the measurement data for a given component were biased high or low; and as such these limits are very conservative.

The integral results indicate that much more zircaloy liquefied than fuel, and that approximately 70% of the control rod material was released to the bundle. All the insulation is generally accounted for, which indicates that very little, if any, was dissolved in the melt regions. This suggests that the insulation relocated after the bundle had cooled, perhaps even during subsequent handling of the fuel bundle. The largest volume of melt was in the ceramic melt regions.

3.1.10 Posttest Mass Balances for Uranium and Zirconium

Core bore samples were obtained from representative regions within the fuel bundle, and elemental analysis was performed on these sample to provide bulk compositional information. Density measurements were also performed on the core bore samples from the ceramic melt and eutectic metallic melt/fuel debris samples to enable estimates to be made of the total amount of material distributed in these regions. From these data it was possible to calculate material balances for the major bundle constituents of uranium and zirconium, as well as providing information on the distribution of uranium and zirconium in the fuel bundle. The zirconium distribution data was subsequently used to calculate zirconium oxidation and hydrogen generation, and the overall mass balances for these elements provided an internal consistency check on the material distribution measurements and methodology.

Details of the analysis methodology are described elsewhere [6], and only the final results are tabulated in Tables 3 and 4. For the nominal conditions the material balance overpredicts the amount of uranium but accurately predicts the amount of zirconium. The overprediction in the uranium mass balance may be partially due to overestimating the amount of fuel present at each metallographic cross section due to the inclusion of fuel cracking and separation of the fuel. These data suggest that the lower estimated values for the cross-sectional and integral volumes of intact and fragmented fuel may be more accurate. However, the overall good agreement in these material balance calculations indicates that the material distribution measurements and methodology provide a reasonable approximation of the actual conditions.

These data also provide information on the amount of molten uranium and zirconium and the partitioning of these elements among the various melts. Approximately 63 wt.% of the zircaloy was liquefied; however, only about 15 wt.% of the fuel was liquefied. Most of these liquefied materials were located in the ceramic melt region, although significant amounts of zirconium were located in the eutectic metallic melt in the lower blockage and in the melt that penetrated the insulation. This reflects the dissolution of unoxidized zircaloy by silver to form the lower blockage, and the melting of the inner liner.

3.2 Oxidation and Hydrogen Generation

Oxidation of zircaloy, stainless steel, and Inconel components all contributed to hydrogen generation in the LP-FP-2 experiment. The zircaloy oxidation was calculated from the postirradiation examination data using two alternative methods; subtraction of unoxidized zirconium from an upper oxidation limit, and addition of oxidized zirconium in the various regions

of the bundle. The first method was considered to provide the best estimate values, however the second method had the advantage of providing information on the distribution of oxidized zirconium, as well as providing a comparison check with the first method. This distribution data was useful for developing a bundle scenario of events, based upon when the zirconium in the various regions probably oxidized. Oxidation of molten stainless steel and Inconel components was also estimated from the postirradiation examination data, to provide an estimate of the total amount of hydrogen generated in LP-FP-2.

3.2.1 Best Estimate of Zircaloy Oxidation and Hydrogen Generation

The best estimate of the zircaloy oxidation was calculated by establishing an upper limit, and then subtracting the unoxidized amounts of zirconium in the various melt regions. This was considered to be superior to the alternative method described in the next section because of reduced uncertainties.

The upper limit for zircaloy oxidation was determined from measurements of the amount of oxidized cladding and guide tube remnants in the bundle, and assuming that all the previously molten zircaloy had fully oxidized. The amount of hydrogen generated as a result of zircaloy oxidation was calculated based upon the following chemical equation:

$$Zr + 2H_2O \rightarrow ZrO_2 + 2H_2$$

Thus for every mole of molten Zr or intact ZrO_2, 2 moles of H_2 could be produced. From this an upper limit of 1226 g of hydrogen from zircaloy oxidation was calculated.

Determination of the amount of unoxidized zirconium in the melt regions was based upon density measurements and elemental analysis of core bore samples from the various melt regions, to provide the total amount of zirconium present, along with SEM/WDS examinations to determine the extent of unoxidized zirconium in those regions. Additional details on the methodology are described elsewhere [6].

Table 5 summarizes the results of this analyses. 862 g of hydrogen from zircaloy oxidation were nominally estimated, with lower and upper limits of 575 and 1064 g respectively. For the nominal case, this corresponds to 49% of the zirconium in the inner liner, cladding, and guide tubes, with the lower and upper limits corresponding to 32% and 60%. The large uncertainties are due to the conservatism incorporated in minimizing and maximizing these estimates. However, as discussed in the following section, good agreement between these calculations and two alternative methods indicates that there is a high probability that the actual amount of hydrogen is near the nominal estimate.

3.2.2 Hydrogen Generation Based Upon Total Oxidized Zirconium

An alternative method for calculating the amount of zircaloy oxidation is based upon summing up the oxidized zirconium in the various regions, as opposed to subtracting the unoxidized zirconium from an upper limit. This method has larger uncertainties associated with it, but it has the

advantage of providing information on the distribution of oxidized zirconium. This information can be used in conjunction with postulated bundle scenarios to provide information on heat generation in the various regions of the bundle at various times during the experiment, and it also provides a check on the amount of zircaloy oxidation and hydrogen generation calculated in the previous section.

The estimated amounts of hydrogen generated from zirconium oxidation in the various regions of the fuel bundle are summarized in Table 6. The total amounts are in very good agreement with the hydrogen estimates based on the alternative methodology (Table 5). The greater limits shown in Table 6 reflect the increased uncertainties associated with calculating the amount of oxidized zirconium in the ceramic melt region, as opposed to calculating the amount of unoxidized zirconium in the smaller metallic melt regions using the first method. The conservatism incorporated in determining the lower and upper limits in Table 6 is apparent in comparing the upper limit of 1204 g of hydrogen in this table, with the absolute fuel bundle upper limit of 1226 g estimated in the previous section. Since there are significant amounts of unoxidized zirconium in the various melt regions, this comparison indicates that the upper and lower limits are indeed very conservative.

The results in Table 6 indicate that very little oxidation was associated with oxidized zircaloy cladding shells. Most of the zircaloy oxidation was associated with previously molten zircaloy in one form or another. The oxidation of the cladding shells had to have occurred relatively early in the test, prior to significant material relocation, because these oxidized shells were surrounded by the melts. It can also be assumed that the oxidation of the zirconium in the eutectic metallic melt regions probably occurred during the transient. This is based upon their position low in the bundle, where they would have been exposed to any steam flow before the rest of the bundle; the probability that they experienced their hottest temperatures as they were relocating to form the lower blockage; and the fact that these would be the first regions quenched by reflood. The data from the melt/insulation regions indicate that a significant amount of the zirconium in these regions was unoxidized. This is probably due to the relatively lower temperatures in these regions of the bundle. These data also indicate that the greatest amount of oxidized zirconium was located in the ceramic melt regions, particularly in the large mass which made up the upper blockage. The partitioning of the zirconium oxidation and hydrogen generation in these various regions provides some valuable information on the possible sequence of bundle events, when these data are compared to measured and calculated hydrogen concentrations in the blowdown suppression tank and the primary coolant system. These comparisons are described in detail elsewhere [7,8].

3.2.3 Oxidation of Stainless Steel and Inconel Components

In addition to the zircaloy, major portions of the type 304L stainless steel upper tie plate were molten and/or oxidized. An example of this is shown in Figure 13. Based upon area fraction measurements, and SEM/WDS examinations that indicated iron and chromium were oxidized in these regions, it was possible to estimate the amount of hydrogen generated from this source. Similar calculations were performed to estimate the hydrogen

generated from the oxidation of iron and chromium in the molten stainless steel cladding and Inconel spacer grids. Details are provided elsewhere [6].

The hydrogen contribution from these sources is shown in Table 7. A total of 163 ± 83 g of hydrogen was calculated from these sources, of which the oxidation of the upper tie plate was the most significant.

3.2.4 Total Hydrogen Generation and Discussion of Results

The best estimate of the total oxidation and hydrogen generation in the LP-FP-2 fuel bundle is the sum of the contributions from the zircaloy components, discussed in Section 3.2.1, and the nonzircaloy components, discussed in Section 3.2.3. These data are summarized in Table 8. It indicates that 1025 g of hydrogen were generated in the nominal case, with lower and upper limits of 655 and 1310 g, respectively. This is in excellent agreement with an independent analysis, based upon grab samples from the blowdown suppression tank and calculated amounts in the primary coolant system, which estimated 1024 ± 364 g of hydrogen. Details of this independent analysis are provided elsewhere [7,8,9], but the results are summarized here to demonstrate the good agreement between the various estimates.

The amount of hydrogen calculated to be in the blowdown suppression tank, based upon grab samples, was 205 ± 11 g. The amount in the primary coolant system, based upon pressure and temperature measurements and calculated gas compositions, was 819 ± 364 g. These values provide an indication of the amount of hydrogen generated during the transient and the reflood period, because the blowdown suppression tank was isolated just prior to reflood.

The data on the distribution of oxidized zirconium in Section 3.2.2 indicated that nominally 181 g of hydrogen were generated from the cladding oxide shells and the oxidized zirconium in the lower blockage, and as discussed in that section these materials had to have oxidized during the transient. This value is in very good agreement with the 205 ±11 g found in the blowdown suppression tank, and which must have been generated during the transient. Correspondingly, 818 g of hydrogen were estimated to have been generated from the ceramic melt regions, the melt which penetrated the insulation, and the oxidation of the nonzircaloy components (Tables 6 and 7), which is also in excellent agreement with the 819 g of hydrogen estimated to be in the primary coolant system, most of which had to have been generated during reflood.

In summary, data from two independent analyses show excellent agreement as to the partitioning of the hydrogen generation between the transient and reflood periods, and in regards to the total amount of hydrogen generated (1024 vs. 1025 g). Excellent agreement was also found between two alternative methods of estimating the zircaloy oxidation and hydrogen generation from the postirradiation examination data (836 vs. 862 g). The agreement between all these values suggests that the best-estimate nominal values closely reflect the actual conditions, and provide a greater degree of confidence in the data than the separate estimates with their individually large uncertainties would imply.

3.3 Estimation of Fuel Bundle Peak Temperatures

Temperatures within the fuel bundle were estimated based upon metallographic observations of changes in the zircaloy microstructure and the presence of molten materials and their interaction with other materials. Thermocouple data obtained during the experiment provided information up until failure and shunting occurred. However, cladding thermocouples in this experiment generally failed at around 2000-2200 K; and only a limited number of fuel centerline thermocouples were available to provide higher-temperature data (up to 2970 K). Consequently, metallographic examinations provided the only data on peak temperatures in many regions of the fuel bundle.

The axial profile of peak bundle averaged temperatures in LP-FP-2 is presented in Figure 39. The primary purpose of this temperature distribution is to provide modelers of this experiment with a single cross sectional average temperature to benchmark their codes. Localized temperatures at a given cross-section varied above and below these peak bundle average temperatures. Details of how this profile was determined are described elsewhere [6], and only a summary of the methodology is provided here.

At and below 0.36 m the peak bundle averaged temperature could be determined from changes in the zircaloy microstructure (recrystallization above 920 K and the formation of prior-beta microstructure above 1245 K). From 0.43-0.46 m the peak bundle average temperatures were based upon material interactions with the spacer grid (primarily Zr-Ni eutectic interactions which become significant above approximately 1400-1500 K).

From 0.58-0.88 m the peak bundle average temperatures were based upon material weighted temperatures for the various regions in the ceramic melt. For example, Figure 10 shows the entire cross section through the 0.77 m elevation through the middle of the ceramic upper blockage region. In the center of this ceramic melt, temperatures were sufficient to cause fuel melting (>3120 K), but on the periphery of the melt the temperatures were above the melting point of $(U,Zr)O_2$ (2810 K) but below the melting point of the oxidized ZrO_2 cladding remnants (2960 K). Fuel centerline thermocouple supported these temperatures, and also indicated that peak temperatures were approximately 2200 K in the peripheral regions of the bundle away from the ceramic melt regions. Average temperatures for each of these temperature regimes were weighted by the amount of material present to calculate the peak bundle average temperature at each cross-section.

In the region above 0.88 m the temperatures were difficult to estimate from the metallographic data because there were very few indicators and the range of possible temperatures was relatively large. Consequently, temperature ranges were based on interpolations between temperatures in the high-temperature ceramic blockage and the upper tie plate. The peak bundle average temperature of 1700 K for the upper tie plate was based upon the fact that the stainless steel plate had melted in the central regions, but was still intact on the periphery; consequently the peak bundle average temperature straddled the 1720 K melting point of the stainless steel. Although the temperature profile must decrease at some point in this region, large uncertainties arise as to the actual shape of the profile,

i.e., whether there is a smooth transition or whether there is an abrupt change at some point.

3.4 Retained Fission Product and Elemental Analysis

Thirty core bores (approximately 6 and 10 mm in diameter) were drilled from specific regions in the metallographic samples for radiochemical analyses. The objective of these analyses were to determine the distribution of core materials and the retention of fission products in various materials.

Elemental analysis (using inductively coupled plasma spectroscopy) was performed for the 27 elements that made up the principal components of the bundle, however only the major constituents of uranium and zirconium were present in sufficient quantities to allow for extrapolation of the data to bundle inventories. This information was used in conjunction with the material distribution data to estimate integral volumes of material and to provide mass balance information as described in Section 3.1.9 and 3.1.10. The zirconium distribution data was also used to determine the distribution of zircaloy oxidation in the fuel bundle as described in Section 3.2.

The radionuclide concentrations were determined from isotopic gamma spectroscopy for ^{110m}Ag, ^{144}Ce, ^{60}Co, ^{134}Cs, ^{137}Cs, ^{152}Eu, ^{54}Mn, ^{144}Pr, ^{103}Ru, ^{106}Ru, and ^{125}Sb; beta spectroscopy for ^{90}Sr; and neutron activation of ^{129}I and subsequent gamma spectroscopy for ^{130}I. The fissile/fertile content was also measured by neutron activation/delayed fission neutron analyses.

Details of these analyses are described elsewhere [6], however the major conclusions and observations are summarized below.

- o Tin apparently concentrated in the metallic melts, as evidenced by Sn/Zr ratios greater than the as-fabricated zircaloy.

- o Fuel and control materials were positively identified in the upper end box, confirming results from the metallographic and SEM/WDS examinations that these material were transported to this region. The fuel materials exhibited low retention of all major fission products, which suggests high temperatures or optimum release conditions.

- o Antimony accumulated in the metallic melt phases in the lower portion of the bundle.

- o Cesium was generally retained within intact and fragmented fuel. Iodine was retained in the intact fuel pellets; however, significant losses were calculated in fragmented fuel at temperatures of approximately 2200-2600 K. Significant losses of both cesium and iodine were measured in partially liquefied fuel.

- o Significant losses of both cesium and iodine were measured in the ceramic melt samples, ranging from essentially complete release to less than 50% retention. These fission product releases could not

be correlated solely to peak temperature, which indicates that other factors (such as time at temperature and surrounding materials) affected the release.

IV. Summary and Conclusions

The major results and conclusions from the postirradiation examinations of the LP-FP-2 fuel bundle are summarized in this section.

The material relocation and stratification in LP-FP-2 resulted in low-melting-point metallic melts near the bottom of the fuel bundle, a high-temperature $(U,Zr)O_2$ ceramic melt region above this, and a debris bed of fuel pellets near the top of the fuel bundle. This is very similar to the result found in smaller scale integral severe fuel damage tests, and from examinations of the TMI-2 core [4,5,11].

Material interactions between silver and zircaloy resulted in liquefaction of the zircaloy well below the melting point of the zircaloy. The zirconium in these Ag-Zr melts interacted with the stainless steel cladding on the control rods and the Inconel spacer grids to cause liquefaction of these materials. Ag-Zr, Zr-Fe, and Zr-Ni interactions can all cause liquefaction of these materials above approximately 1200 K, but they become particularly significant above approximately 1400-1500 K.

The distribution of oxidized cladding shells indicates that the upper extent of significant cladding oxidation, prior to massive material relocation, was approximately 1.04-1.14 m. Above this elevation the cladding shells were limited to a few rods on the periphery of the bundle. Upon control rod failure, silver aerosols were released which liquefied the unoxidized zircaloy in the upper portion of the bundle. The resultant melt relocated to form the lower blockage, diverting steam flow to the periphery of the bundle. The presence of these materials near the bottom of the fuel bundle, and the relatively low temperatures required for their liquefaction, indicates that these were the first materials to massively relocate during the transient.

The largest flow blockages (78-86%) were located through or just above the two remaining spacer grids. This indicates that the spacer grids tended to impede material relocation.

Integration of the posttest open flow measurement data indicated that the total volume of open area within the fuel bundle was reduced by 11% as a result of porosity trapped in the various melt regions. This corresponds to a 15% volume expansion of the material initially contained within the inner liner.

Fuel grain boundary separation was associated with the presence of metallic melts. This suggests that fuel reduction may have occurred adjacent to these metallic melts, resulting in the formation of a liquid uranium phase along these grain boundaries. The effect was not observed where high-temperature ceramic melts were in contact with the fuel. Fuel fragmentation was also observed in areas that were not surrounded by any melt material, which suggests that the thermal shock associated with reflood may have contributed to fuel fragmentation.

Foamy fuel structures occurred as a result of iron oxides liquefying the fuel. However, porous fuel structures were also observed on fuel pellets surrounded by the high-temperature ceramic melt, and SEM/WDS examinations confirmed that this was pure UO_2. This indicates that peak temperatures near the center of the ceramic upper blockage exceeded fuel melting (>3120 K).

The nominal grain size for most of the fuel was the same as in the as-fabricated condition (14 mm), although some grain growth did occur in the center of some of the fuel pellets in the hotter regions of the fuel bundle. The grain size in those regions averaged 27 mm. The relatively large as-fabricated grain size, and general lack of grain growth, may have been an important factor in the small release of cesium and iodine from intact fuel pellets in this experiment.

These postirradiation examinations identified fuel debris and melt materials in the upper end box, as well as extensive melting and oxidation of the upper tie plate. The relocation of these materials, and the damage to the upper tie plate, could only have occurred during the reflood period when steam mass flow rates and temperatures were sufficient to have caused the observed behavior.

Approximately 63% of the zircaloy cladding and inner liner had liquefied, as compared to approximately 15% of the fuel. Most of the molten material was contained in the ceramic melt region, and zirconium was the most abundant element in this region. Large amounts of zirconium were also present in various metallic melts.

The best estimate of the hydrogen generated from zircaloy oxidation was 862 g. This corresponds to 49% of the zircaloy cladding and inner liner. An alternative methodology resulted in an estimate of 836 g, showing good agreement between the two estimates. An additional 163 g of hydrogen was nominally estimated to have been generated from oxidation of stainless steel and Inconel components, resulting in a best estimate total of 1025 g of hydrogen. This total is also in excellent agreement with measurement data based upon grab samples taken from the blowdown suppression tank, which indicated 205 ± 11 g of hydrogen, and from an estimated amount of 819 ± 364 g in the primary coolant system, for a total amount of 1024 g [8,9]. Analysis of the postirradiation examination data also indicated that 181 g of hydrogen were nominally generated during the transient phase from the oxidation of zircaloy cladding and the material in the lower blockage. This is in reasonable agreement with the 205 g in the blowdown suppression tank, which is indicative of the amount of hydrogen generated during the transient because this tank was isolated from the system just prior to reflood. The hydrogen that resulted from the oxidation of the ceramic melt material, the melt which penetrated into the insulation, and the oxidation of the molten stainless steel and Inconel components, totals 818 g, which agrees with the 819 g estimated to be in the primary coolant system, where all the hydrogen generated during reflood would have ended up [8,9]. These data indicate that most of the hydrogen in the LP-FP-2 test was generated during the reflood period.

Cesium was generally retained within intact and fragmented fuel pellets. Iodine was retained in the intact fuel pellets; however, significant losses were calculated in fragmented fuel at temperatures of approximately 2200 to 2600 K. Significant losses of both cesium and iodine were measured in partially liquefied fuel. Significant losses of both cesium and iodine were measured in the ceramic melt regions; ranging from essentially complete release to less than 50% retention. However, fission product release in these melt regions could not be correlated solely to peak temperature, which indicates that other factors (such as time at temperature and the nature of the surrounding material) affected fission product release.

References

[1] A. D. Knipe, S. A. Ploger, D. J. Osetek, "PBF Severe Fuel Damage Scoping Test-Test Results Report", NUREG/CR-4683, EGG-2413, August, 1986.

[2] Z. R. Martinson, D. A Petti, B. A Cook, "PBF Severe Fuel Damage Test 1-1 Test Results Report", Volumes 1 and 2, NUREG/CR-4684, EGG-2463, October, 1986.

[3] Z. R. Martinson, et al., "PBF Severe Fuel Damage Test 1-3 Test Results Report", NUREG/CR-5354, EGG-2565, October, 1989.

[4] D. A. Petti, et al., "PBF Severe Fuel Damage Test 1-4 Test Results Report", NUREG/CR-5163, EGG-2542, May, 1989.

[5] J. M. Broughton, P. Kuan, D. A. Petti, E. L. Tolman, "A Scenario of the TMI-2 Accident", Nuclear Technology, August, 1989.

[6] S. M. Jensen, D. W. Akers, B. A. Pregger, "Postirradiation Examination Data and Analyses for OECD LOFT Fission Product Experiment LP-FP-2", Volumes 1 and 2, OECD LOFT-T-3810, December, 1989.

[7] M. Carboneau, "Highlights of the OECD LOFT LP-FP-2 Experiment, Including Hydrogen Generation, Fission Product Chemistry, and Transient Fission Product Release Fractions", in these same proceedings.

[8] S. M. Modro, M. Carboneau, "The Severe Fuel Damage Scenario. Discussion of the Relative Influence of the Transient and Reflood Phase in Affecting the Final Condition of the Bundle", in these same proceedings.

[9] M. L. Carboneau, et al., "Experiment Analysis and Summary Report for OECD LOFT Project Fission Product Experiment LP-FP-2", OECD LOFT-T-3806, June, 1989.

[10] M. L. Carboneau, et al., "OECD LOFT Fission Product Experiment LP-FP-2 Data Report", OECD LOFT-T-3805.

[11] R. Hobbins, G. D, McPherson, "A Summary of Results from the LOFT LP-FP-2 Test and Their Relationship to Other Studies at the Power Burst Facility and of the Three Mile Island Unit 2 Accident," in these same proceedings.

[12] P. Hofmann, S. Hagen, G. Schanz, A. Skokan, "Reactor Core Materials Interactions at Very High Temperatures", Topical Meeting on the TMI-2 Accident Materials Behavior and Plant Recovery Technology, October 31-November 4, 1988, Washington D. C.

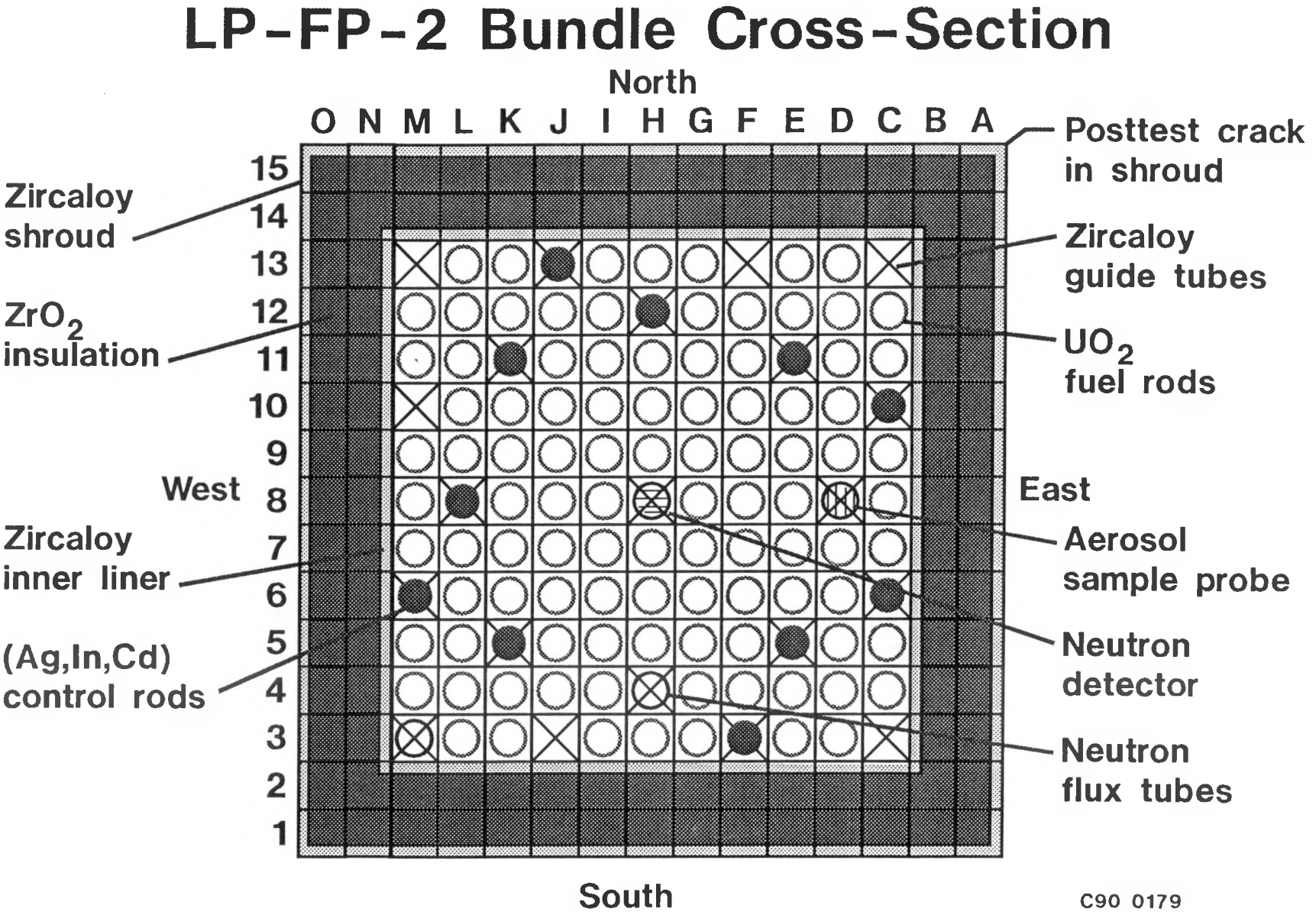

Figure 1. Cross section through LP-FP-2 fuel bundle.

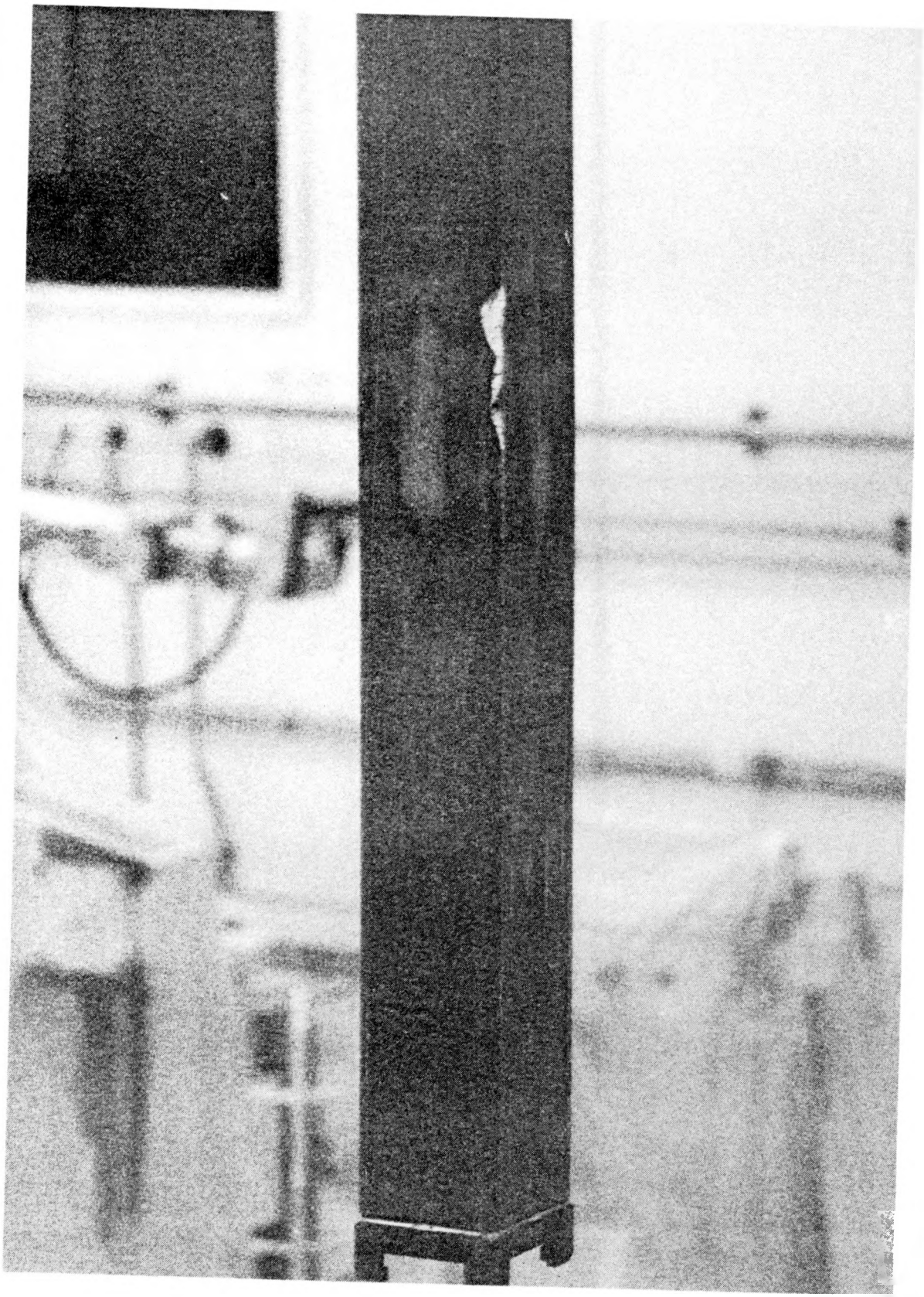

Figure 2. Overall view of the LP-FP-2 fuel module taken during visual examinations.

Figure 3. Close-up view of relocated debris in the LP-FP-2 upper end box.

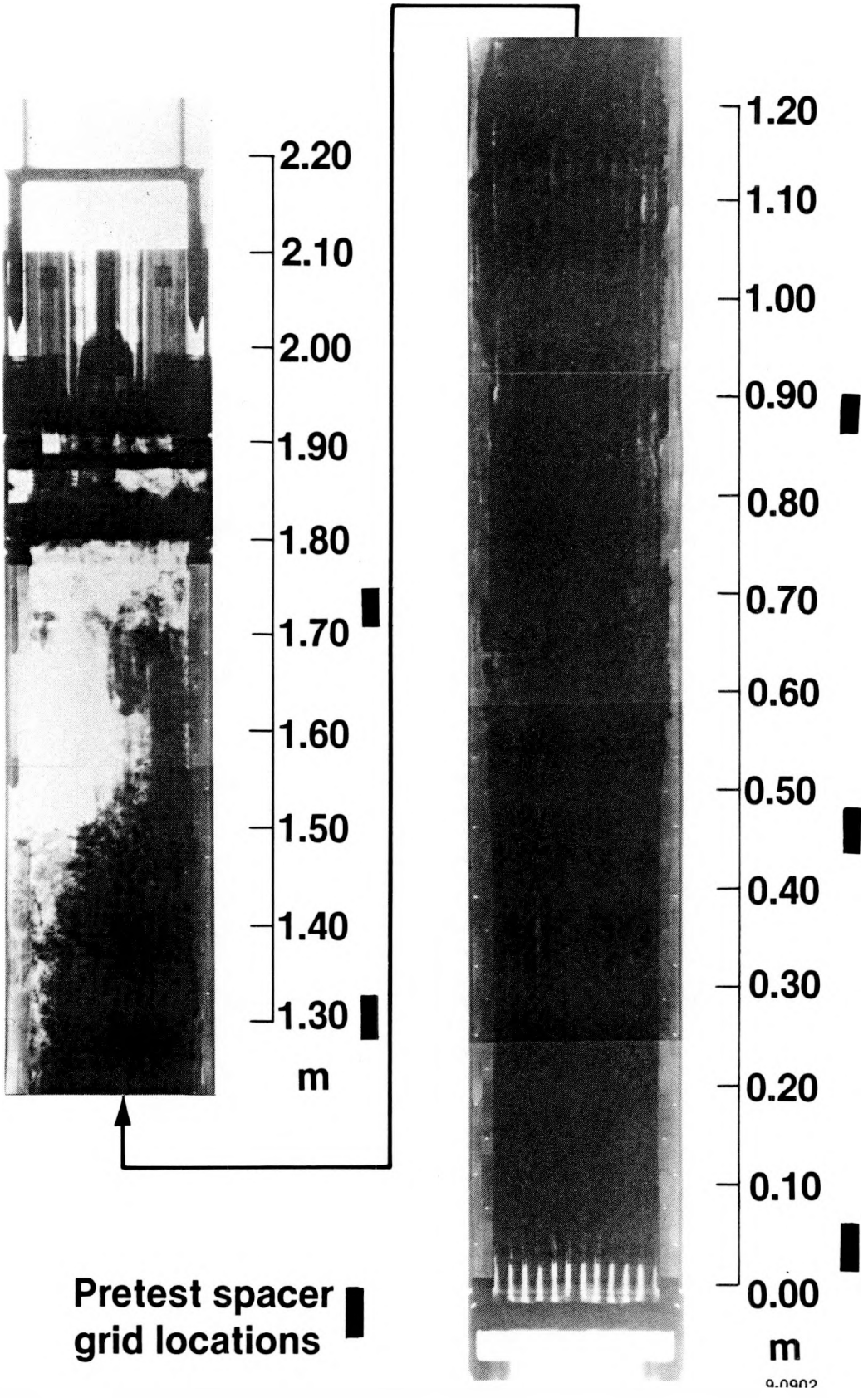

Figure 4. Neutron radiograph of the LP-FP-2 fuel bundle (north view).

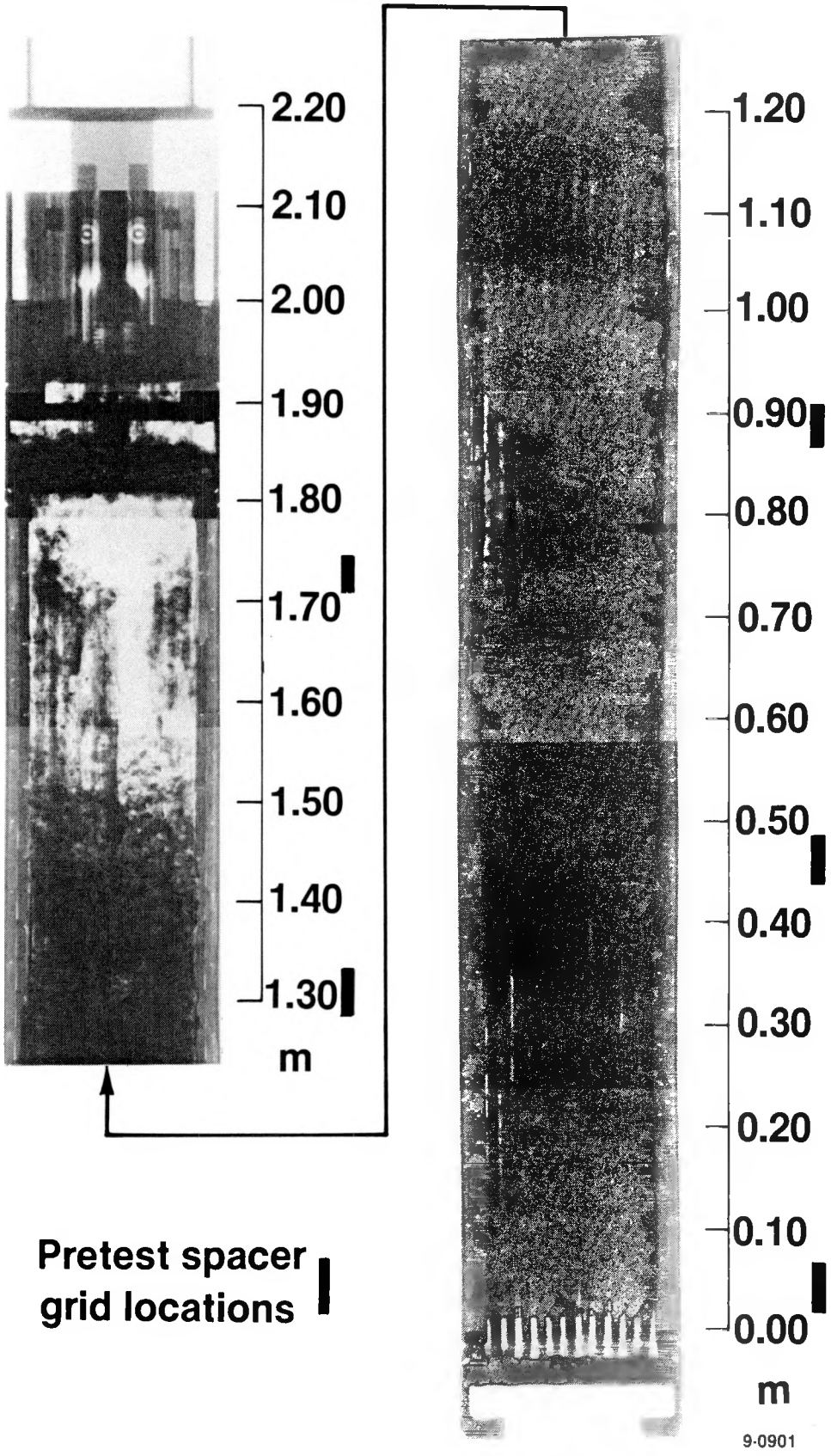

Figure 5. Neutron radiograph of the LP-FP-2 fuel bundle (east view).

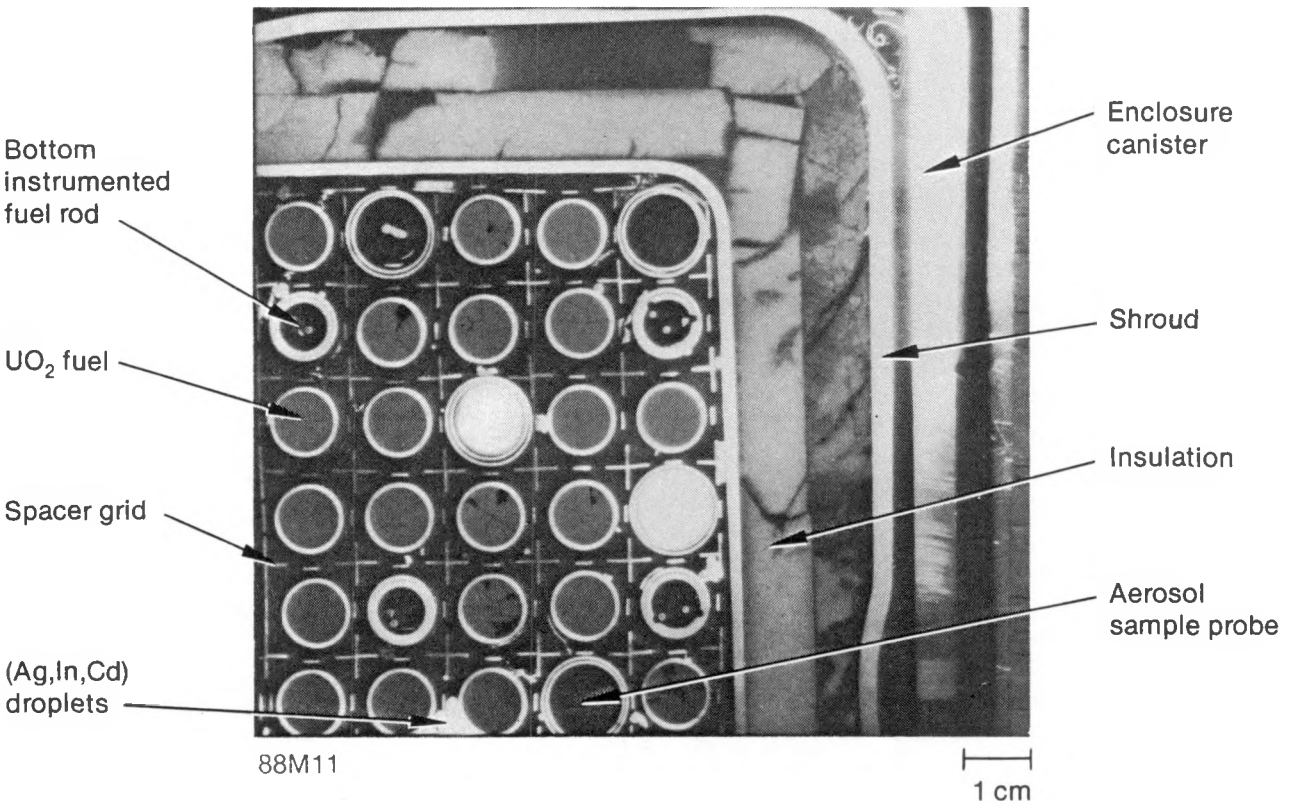

Figure 6. Quarter cross-section through bottom spacer grid (0.03 m).

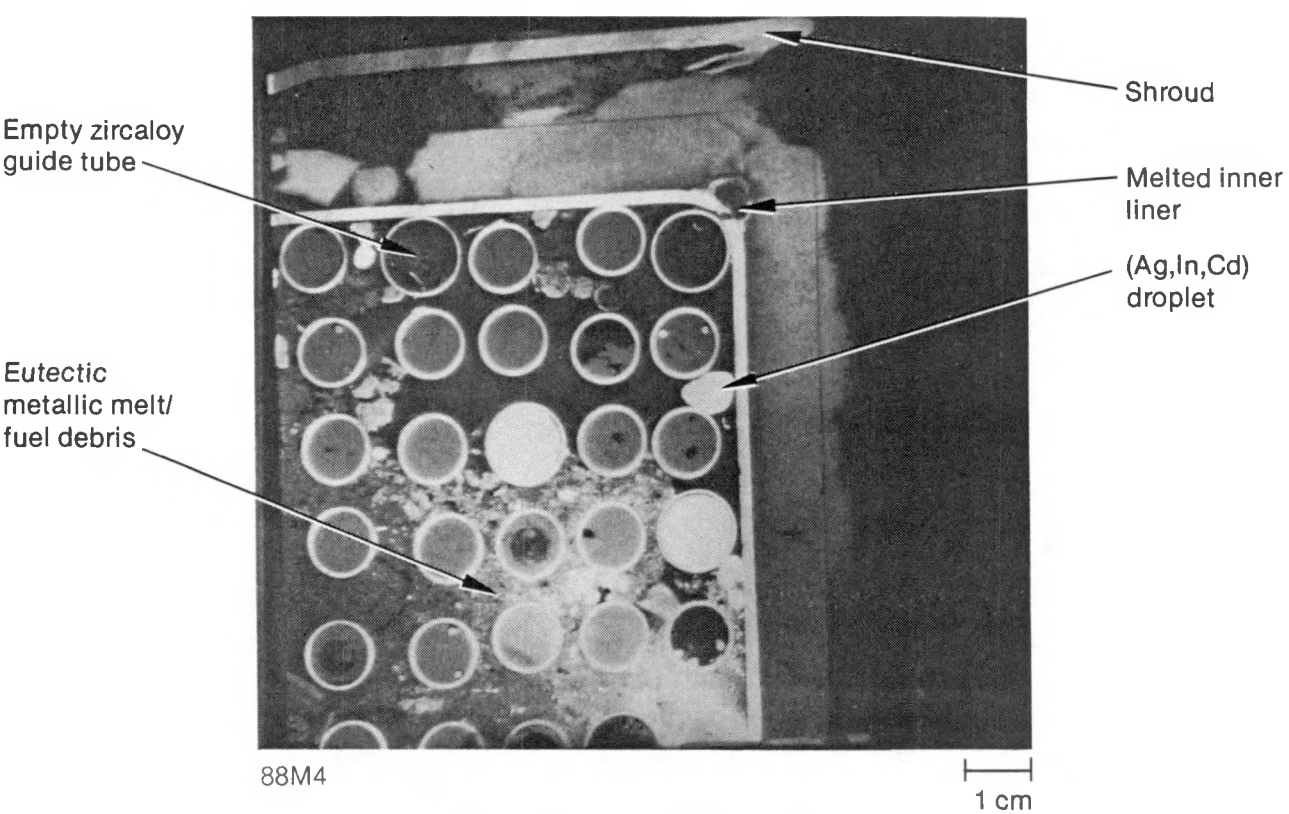

Figure 7. Quarter cross-section through lower blockage (0.22 m).

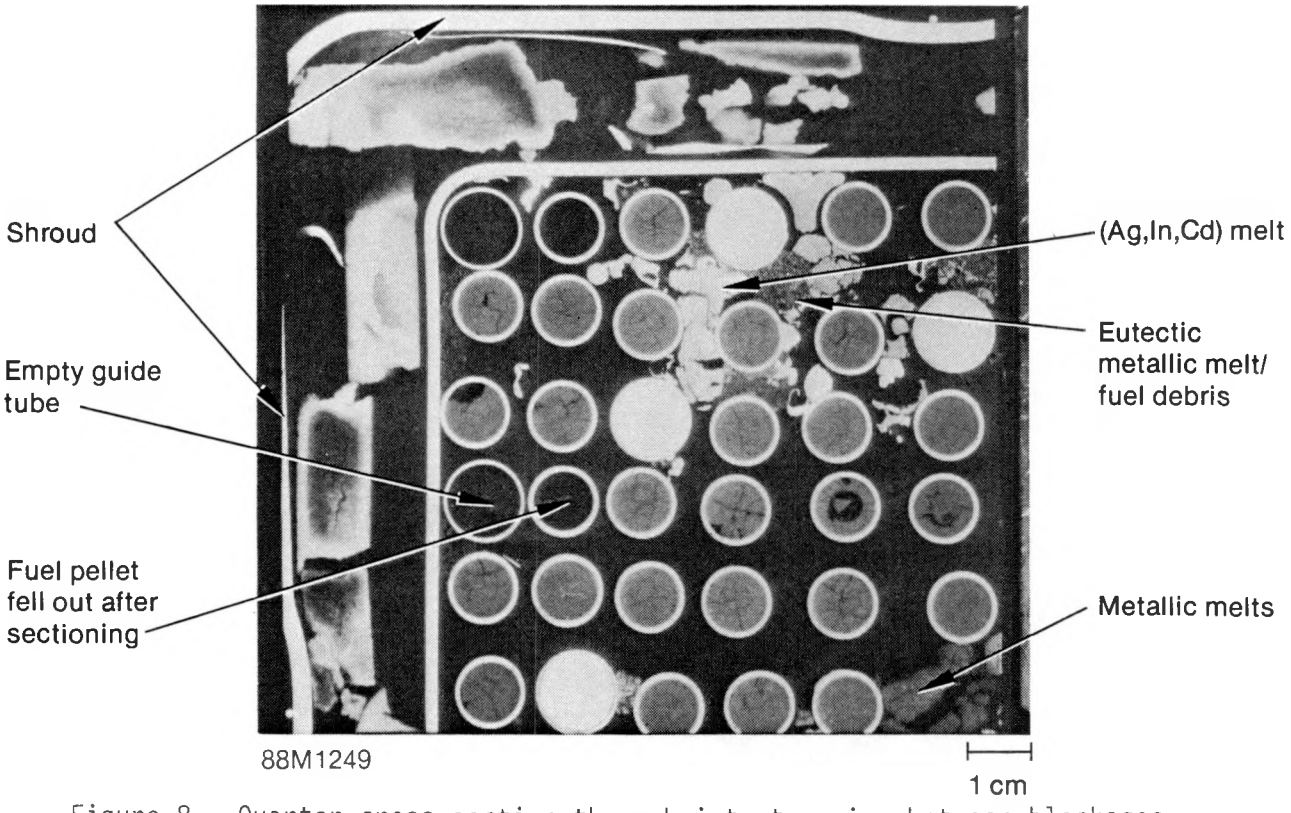

Figure 8. Quarter cross-section through intact region between blockages (0.36 m).

Figure 9. Quarter cross-section through second spacer grid (0.46 m).

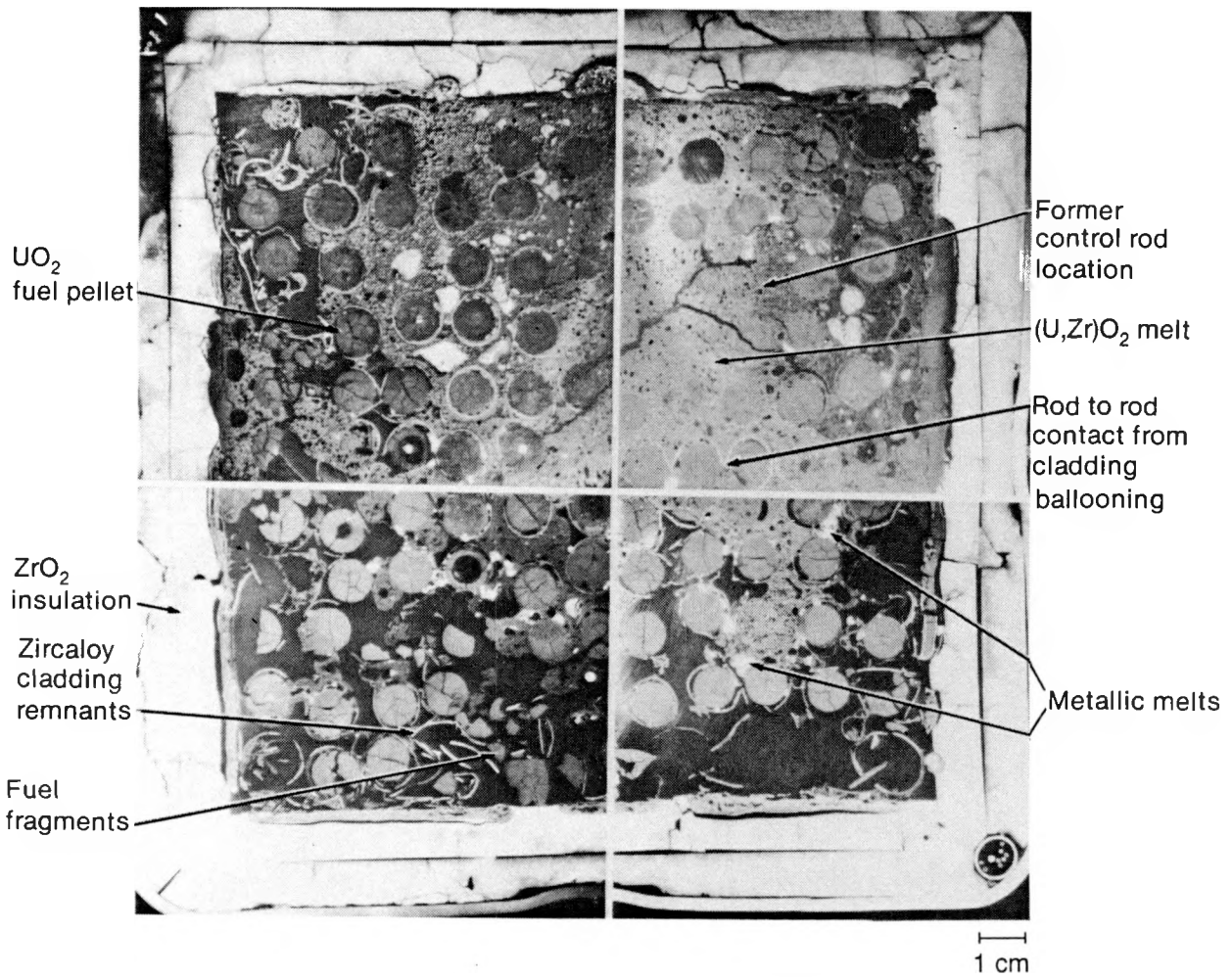

Figure 10. Full-cross section through ceramic upper blockage (0.77 m).

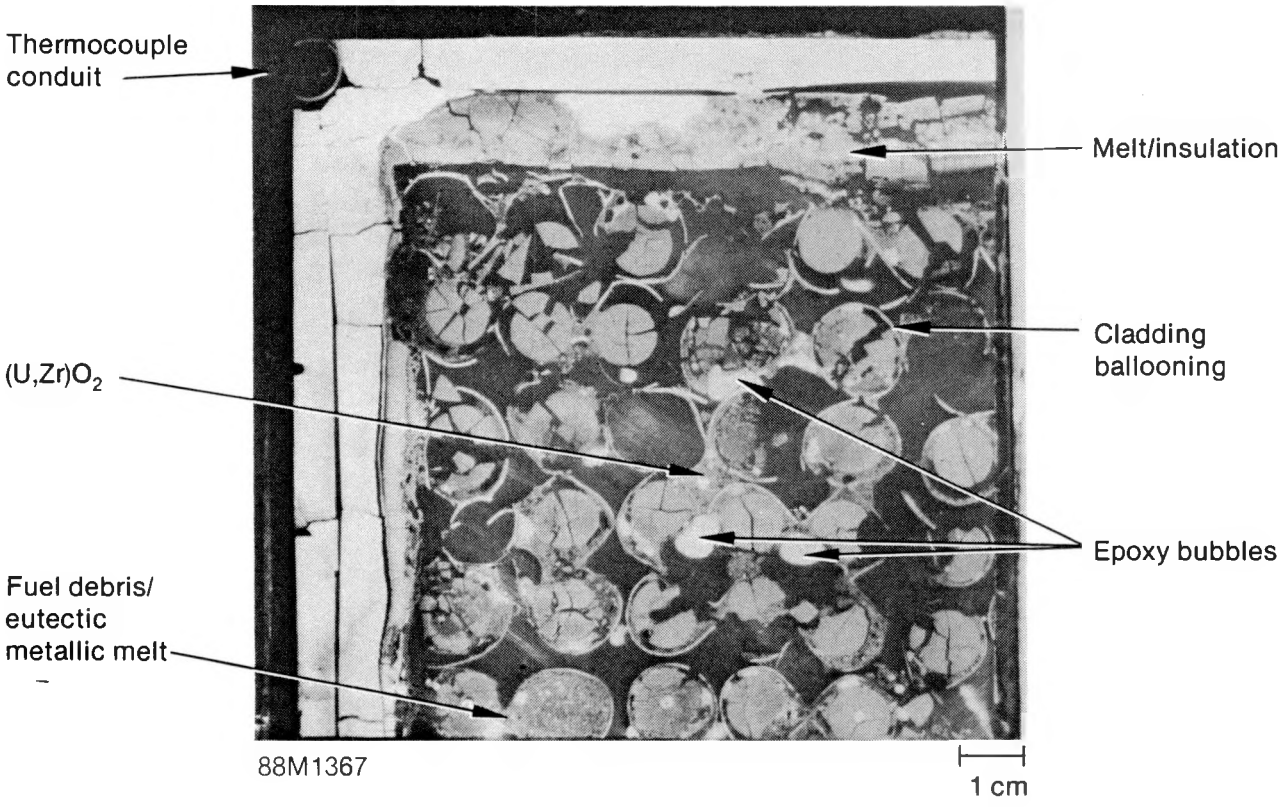

Figure 11. Quarter cross-section through the rod array region above the upper blockage (1.04 m).

Figure 12. Quarter cross-section through the fuel debris bed (1.2 m).

Figure 13. Quarter cross-section through the upper tie plate (1.8 m).

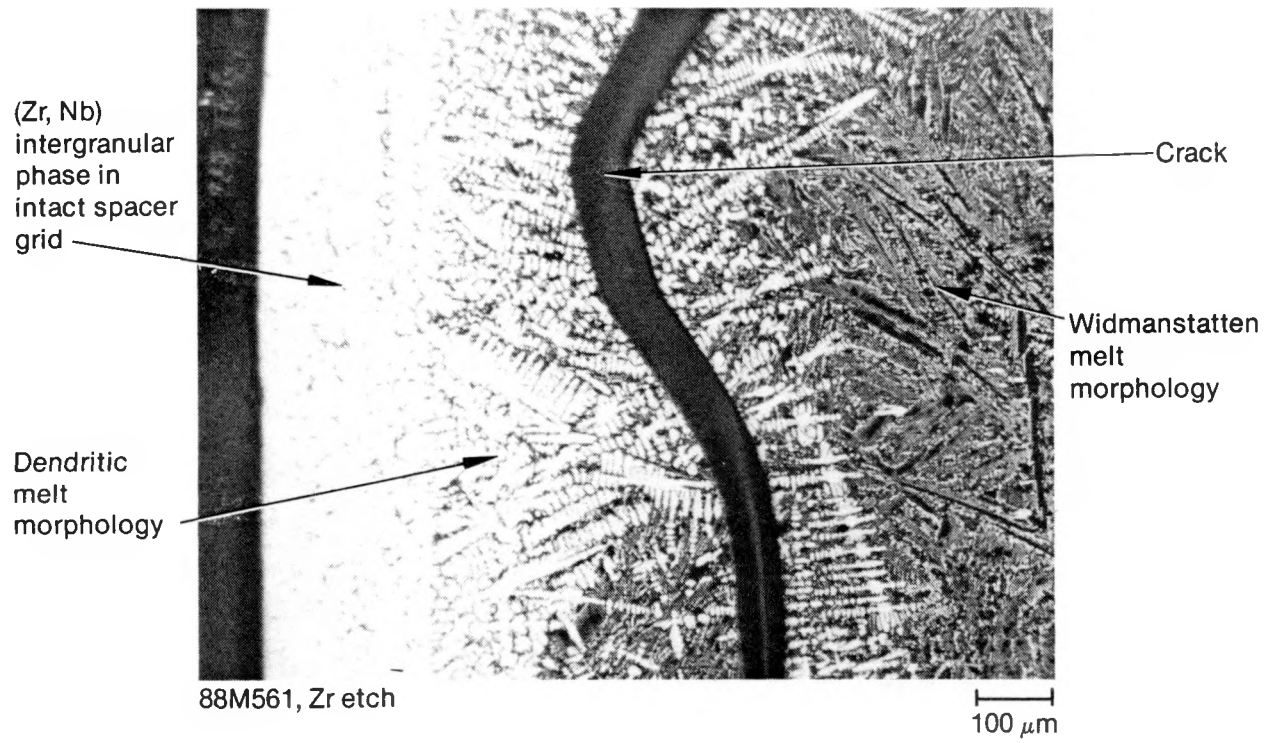

Figure 14. Damage gradient in metallic melt/spacer grid interactions at 0.46 m.

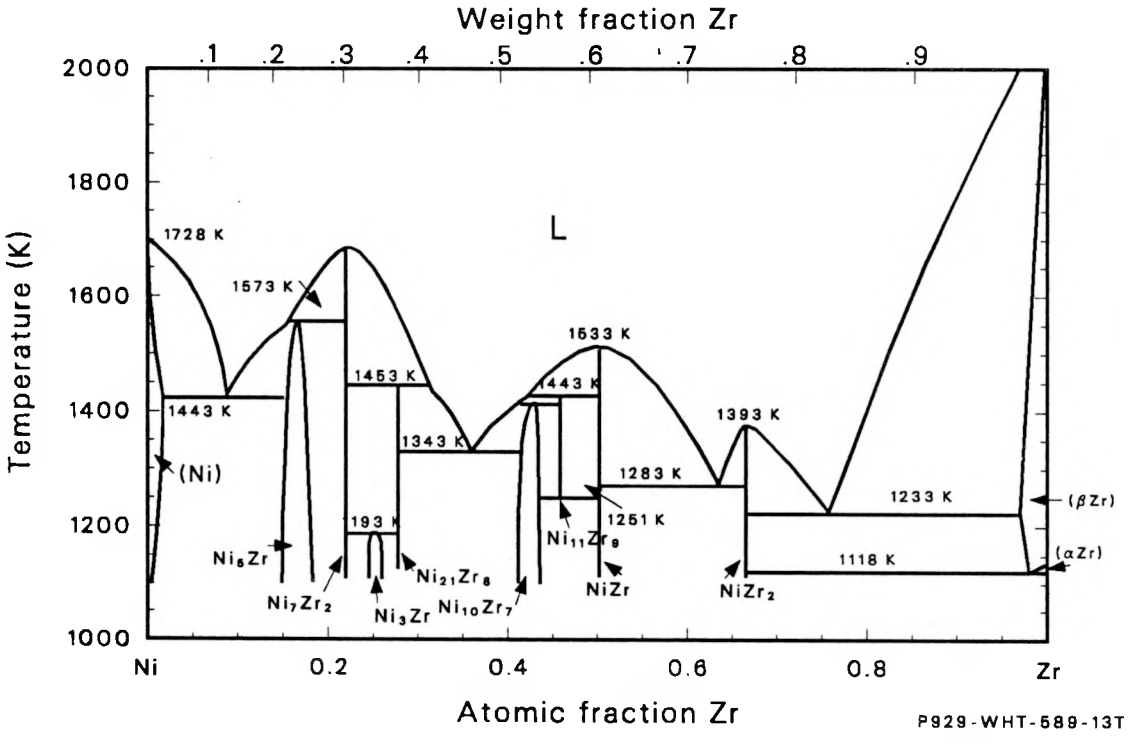

Figure 15. Ni-Zr phase diagram

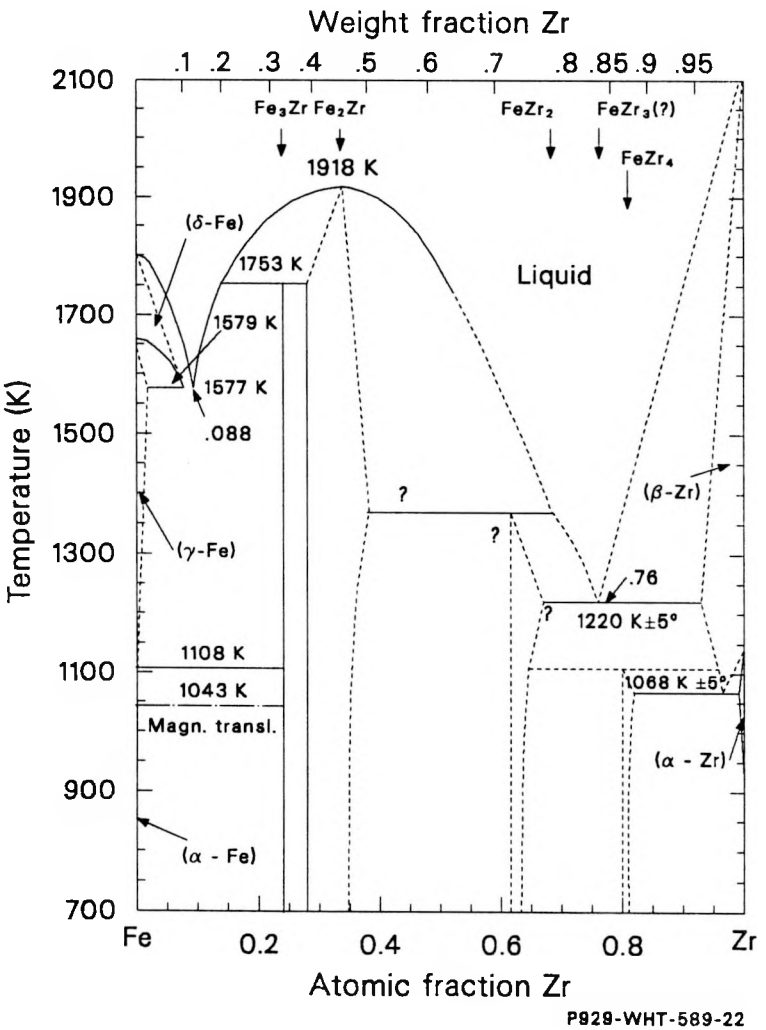

Figure 16. Fe-Zr phase diagram.

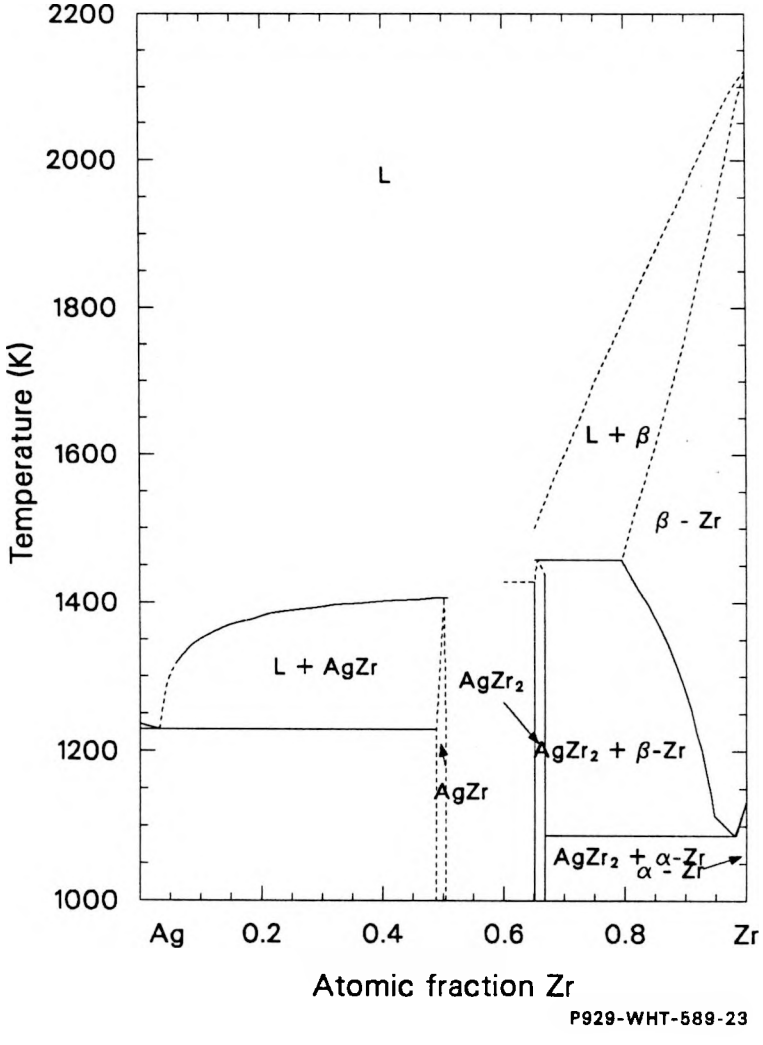

Figure 17. Ag-Zr phase diagram.

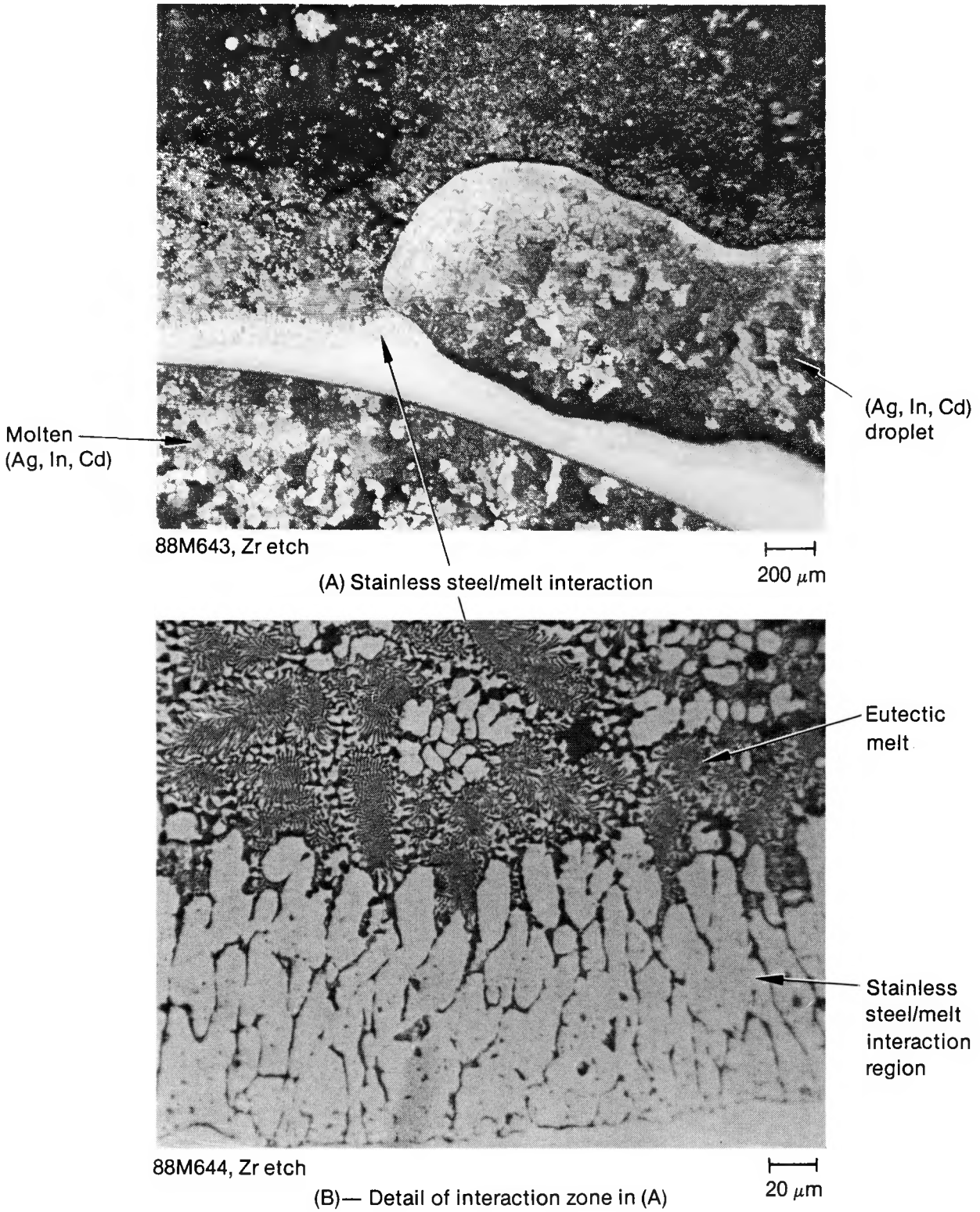

Figure 18. Interaction zone between metallic melt and stainless steel cladding at 0.46 m.

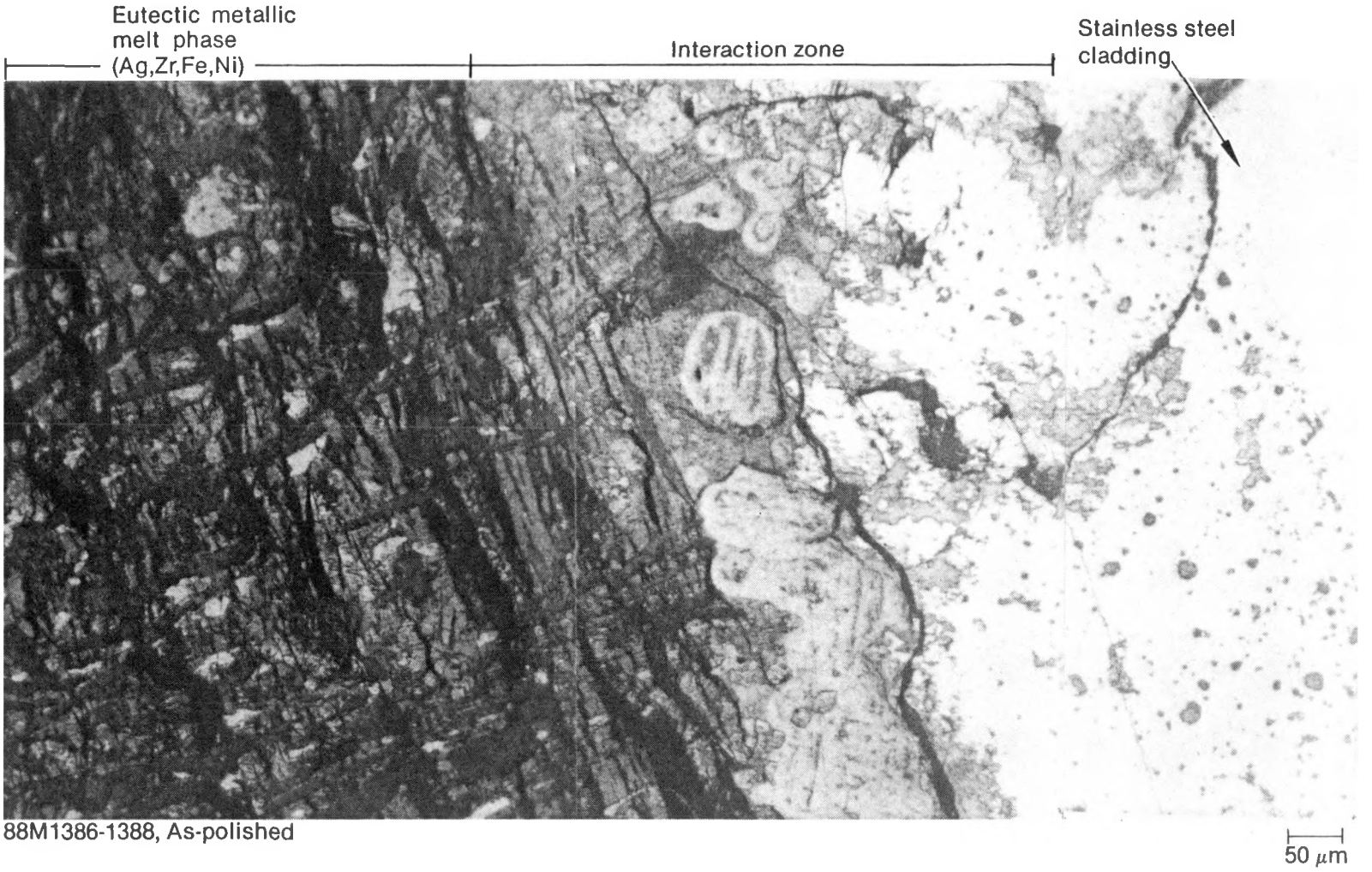

Figure 19. Details of metallic melt/stainless steel interaction zone shown in Figure 174 at 0.43 m.

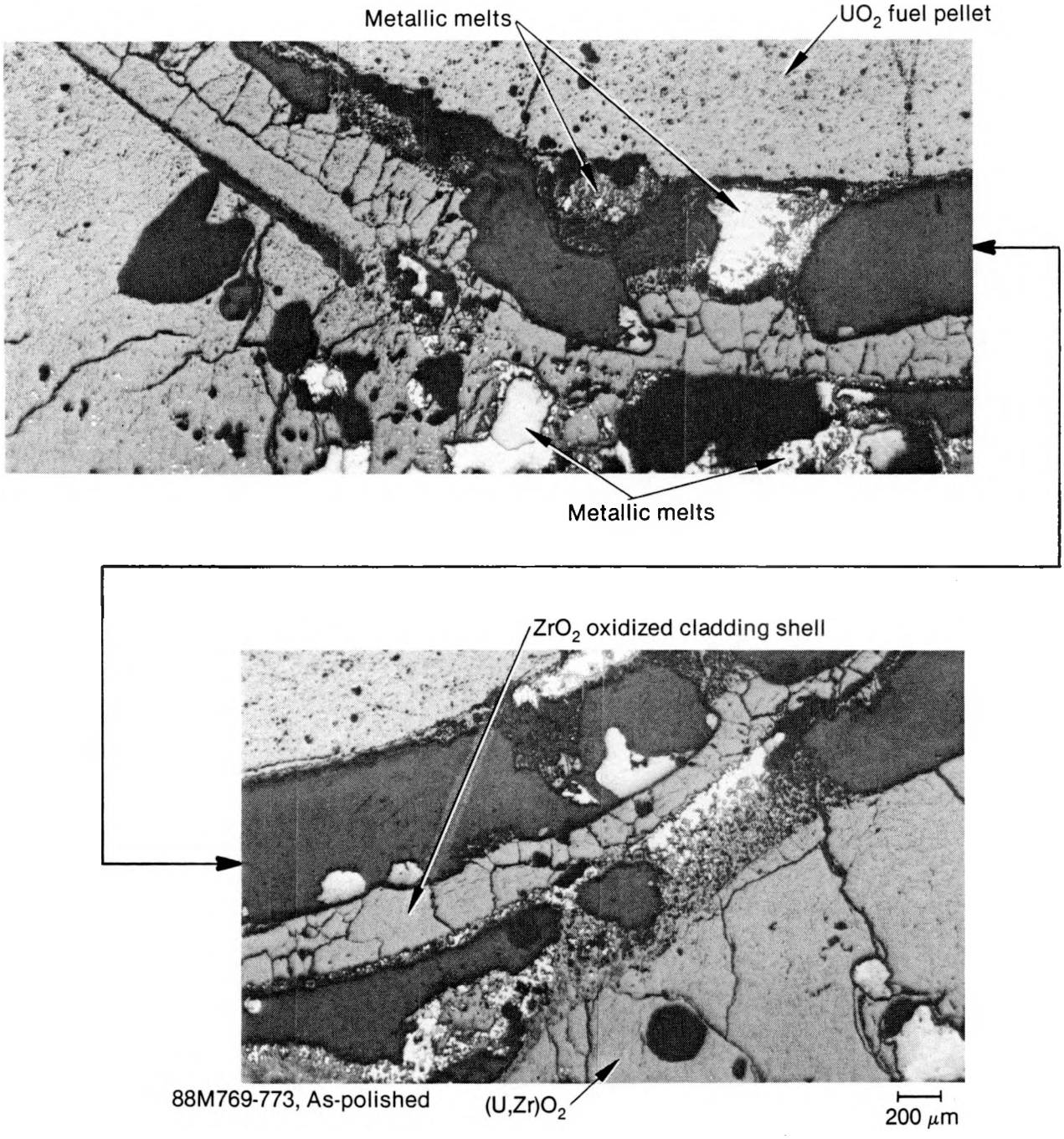

Figure 20. Melt and relocation of unoxidized zircaloy on cladding inner surface at 0.58m.

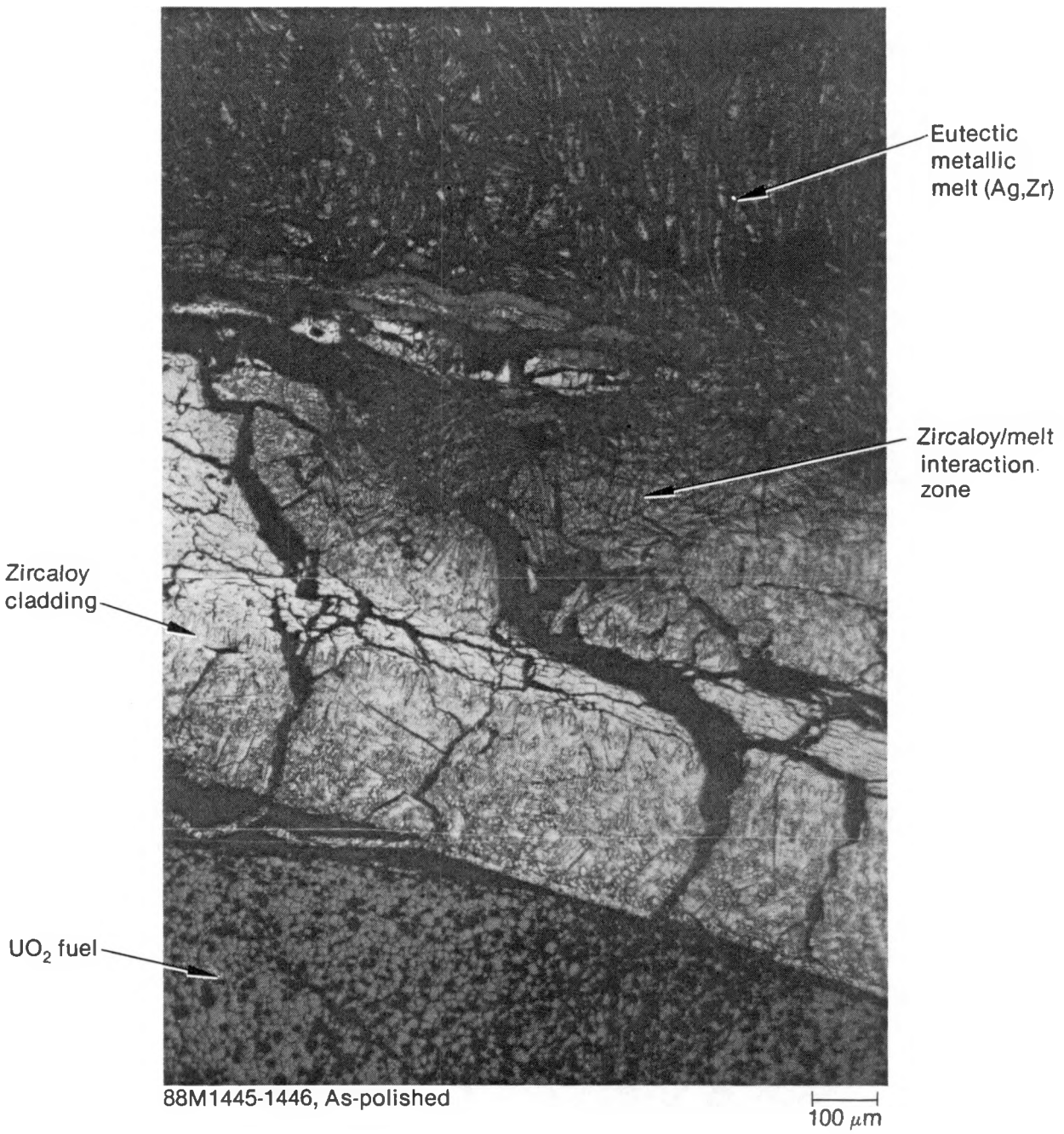

Figure 21. Formation of laminar eutectic metallic melt phase from interactions between metallic melt and zircaloy cladding at 0.43 m.

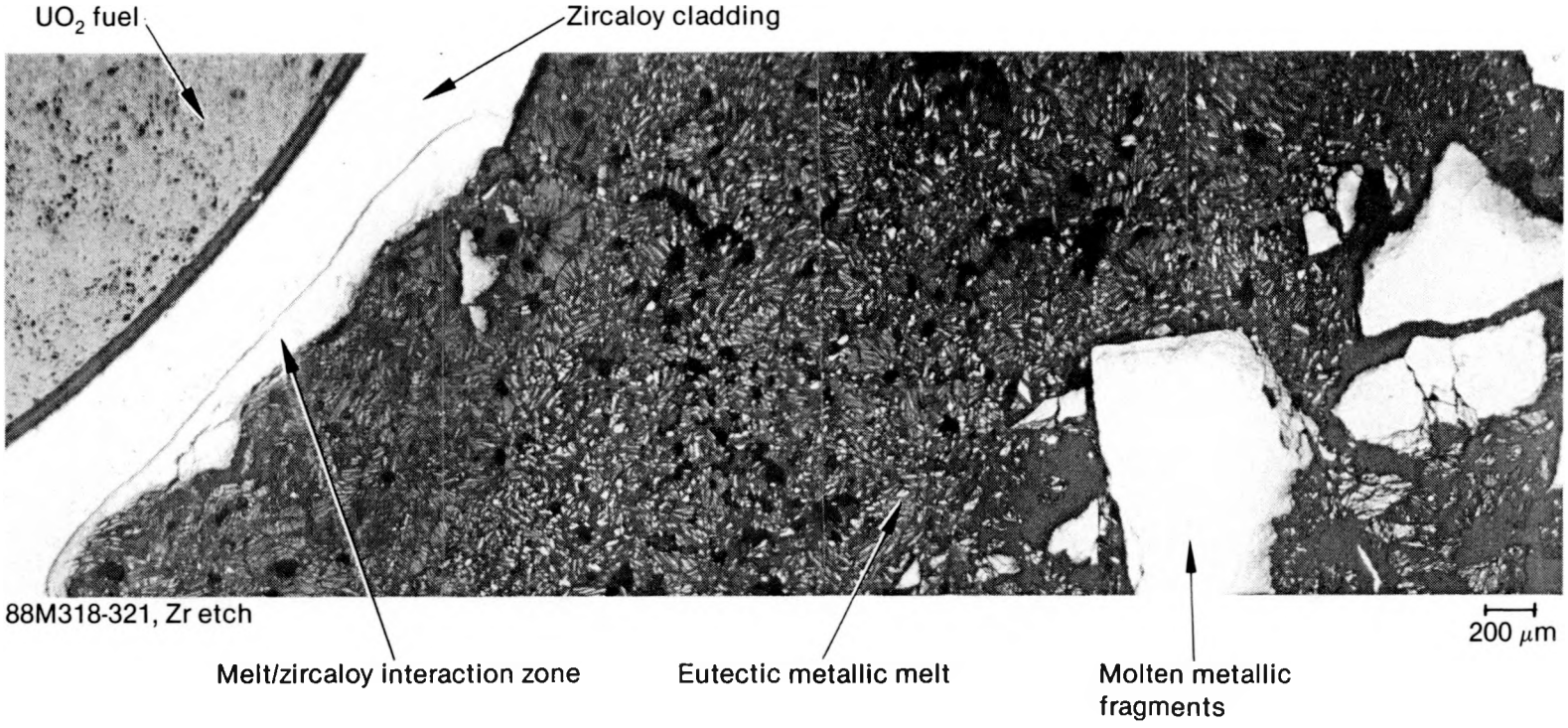

Figure 22. Laminar eutectic metallic melt material in lower blockage region at 0.22 m.

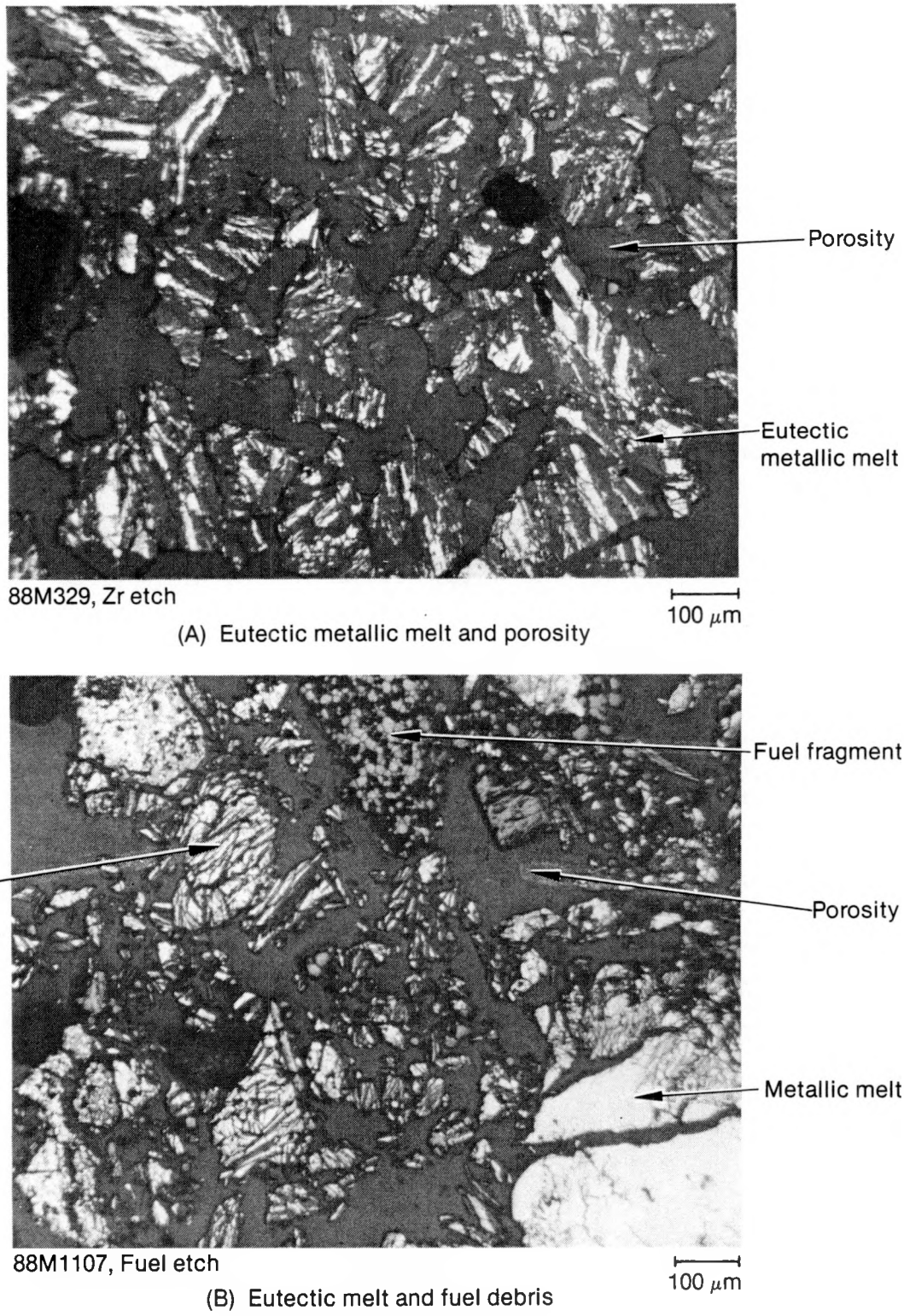

Figure 23. Details of laminar eutectic metallic melt phase at 0.22 m.

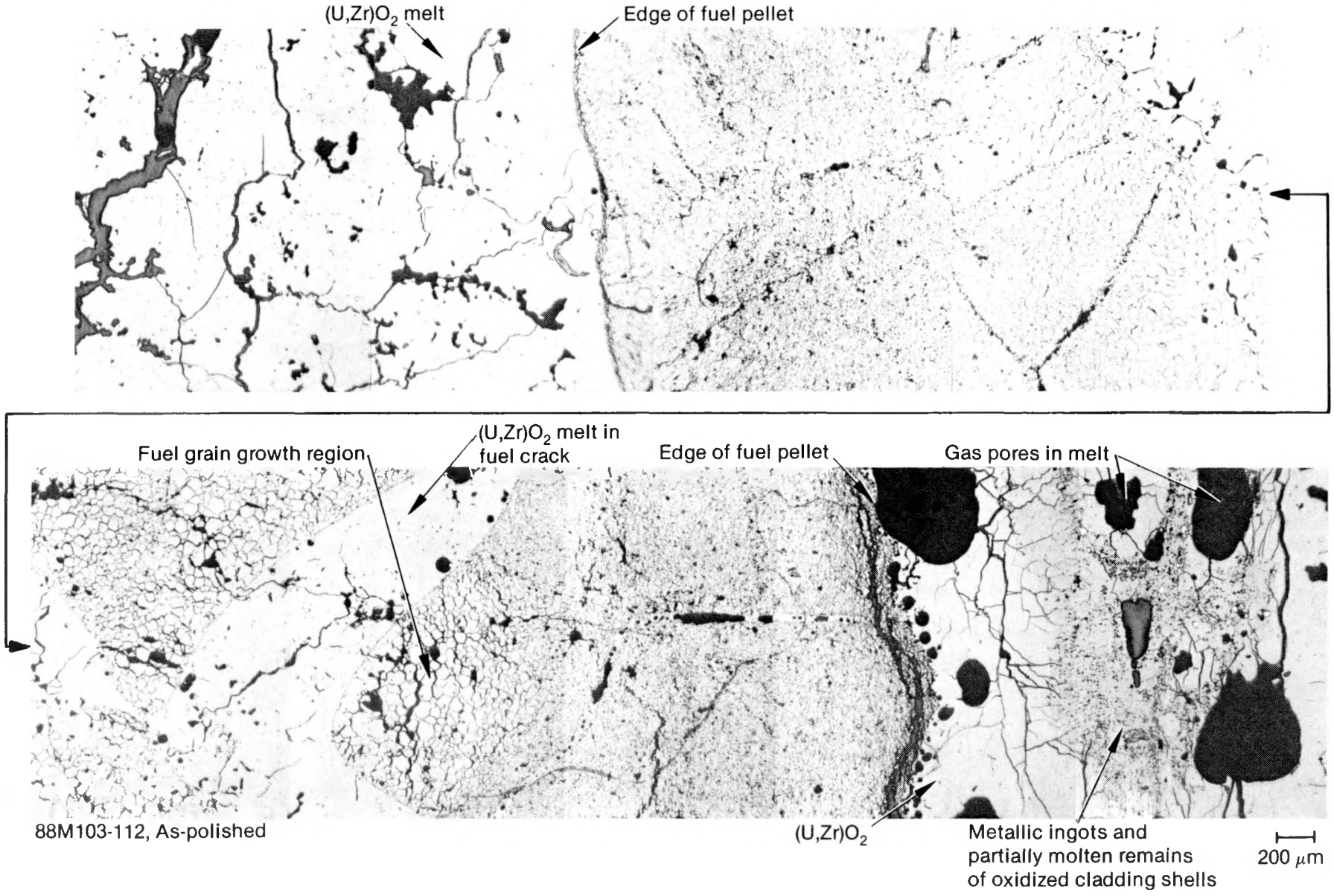

Figure 24. Interactions between $(U,Zr)O_2$ melt and fuel and oxidized cladding remnants at 0.66 m.

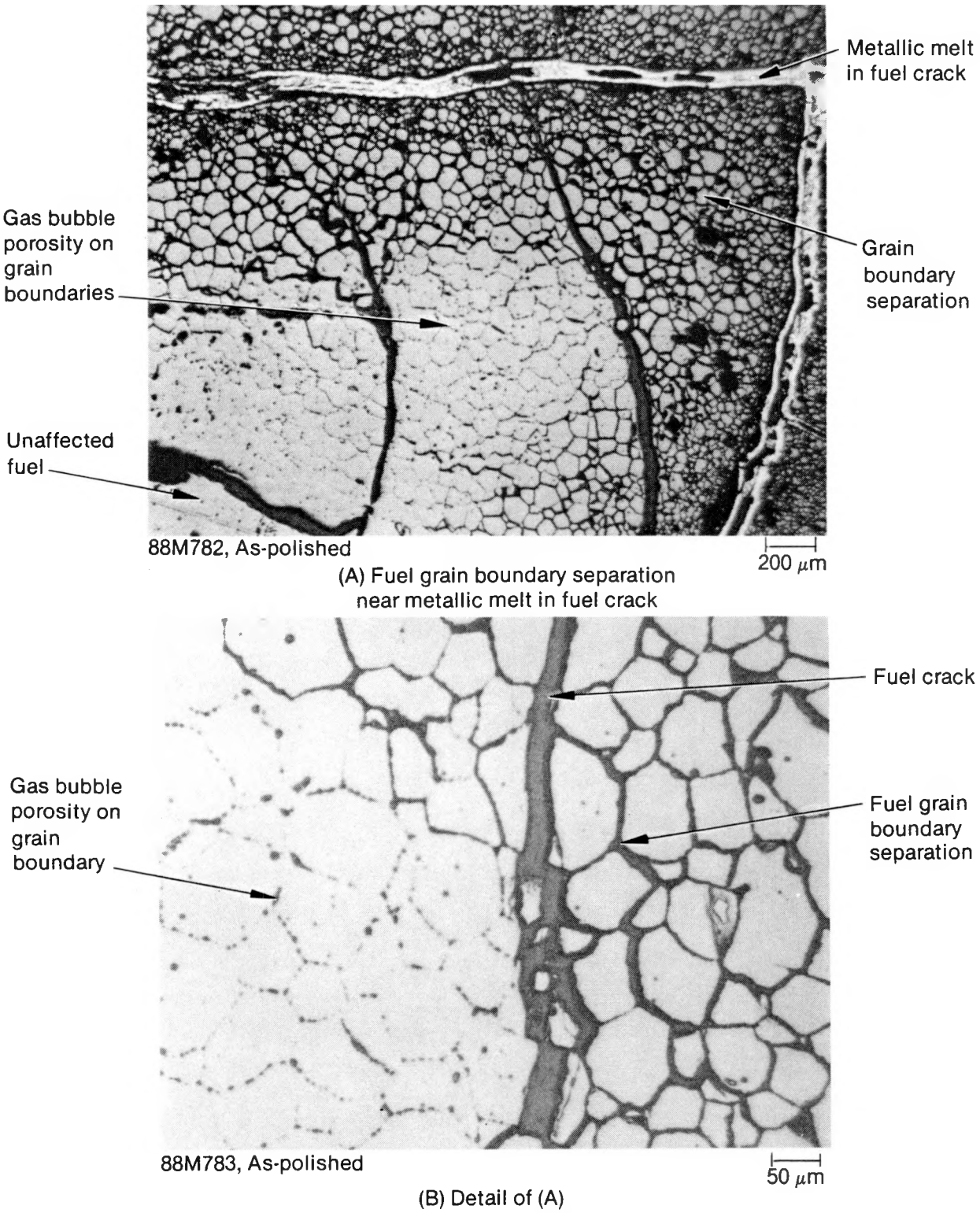

Figure 25. Gradient in fuel behavior near a metallic melt in a fuel crack at 0.58 m.

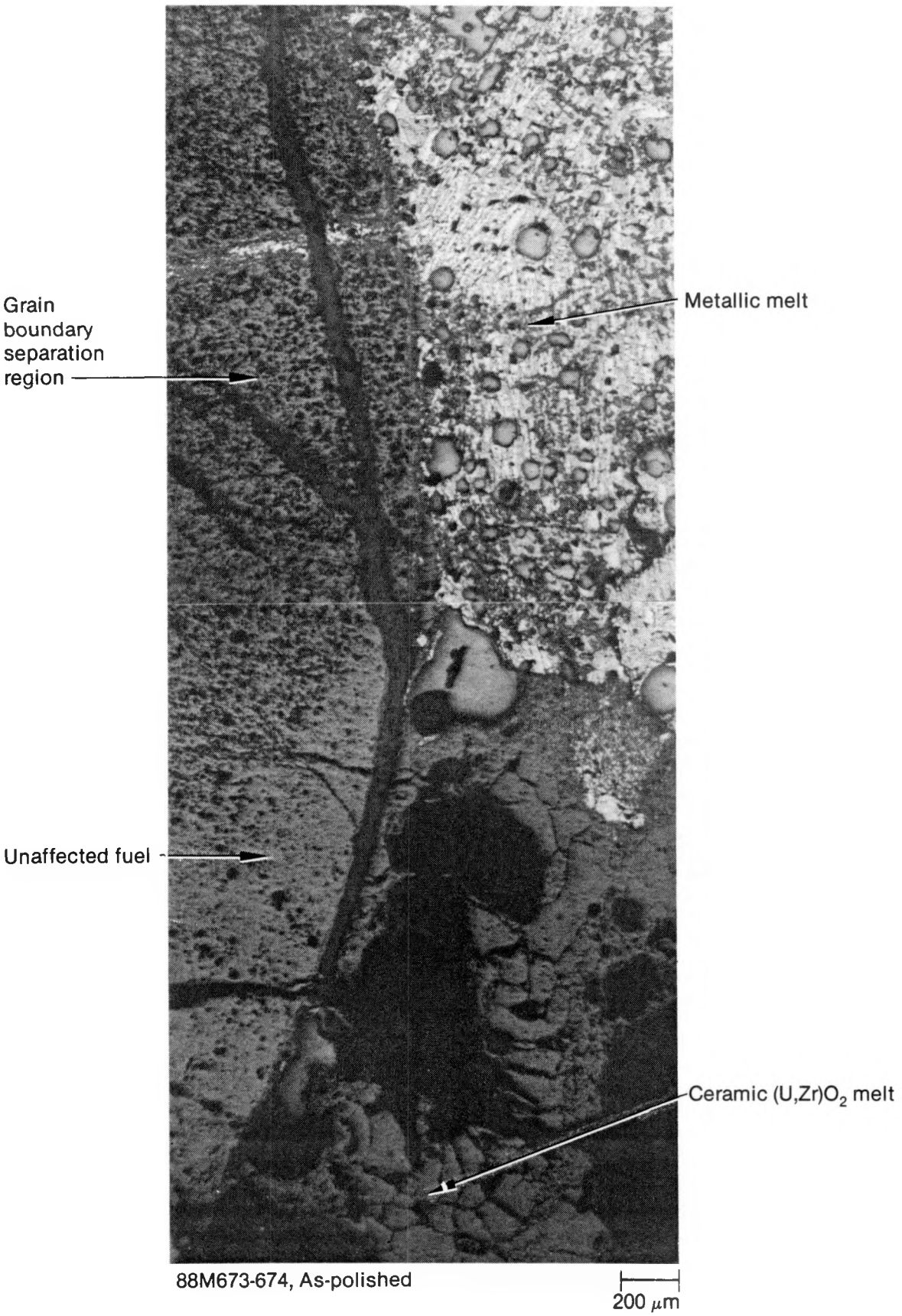

Figure 26. Different fuel structures adjacent to metallic and ceramic melts at 0.66 m.

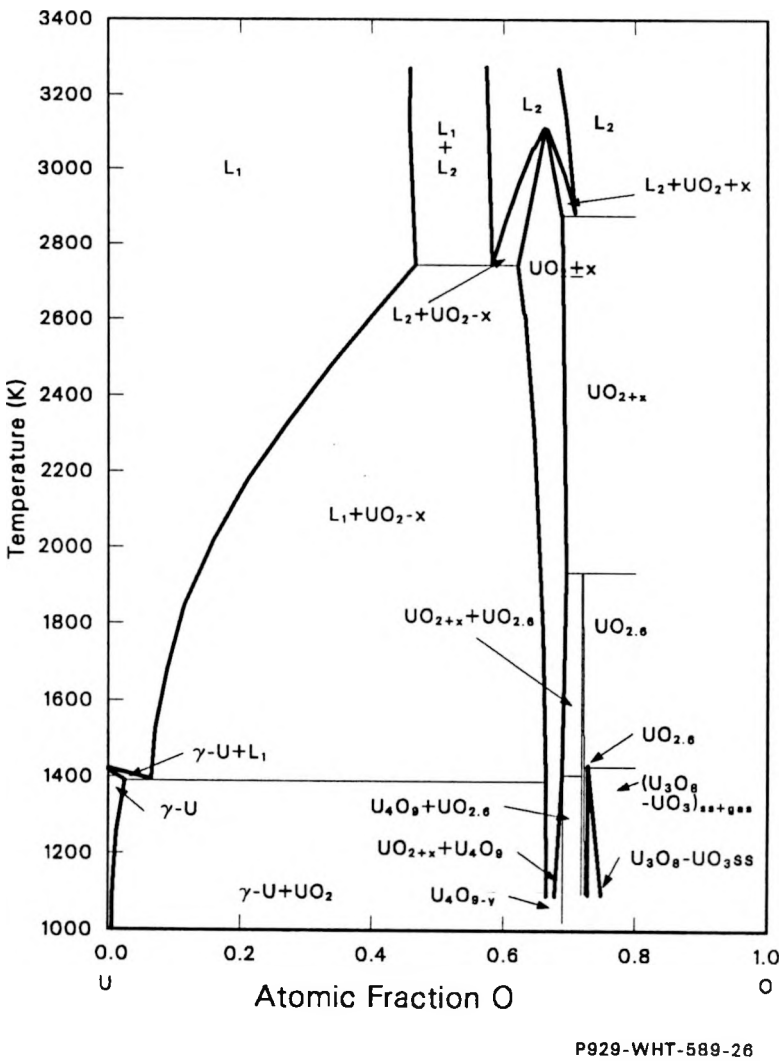

Figure 27. U-O phase diagram.

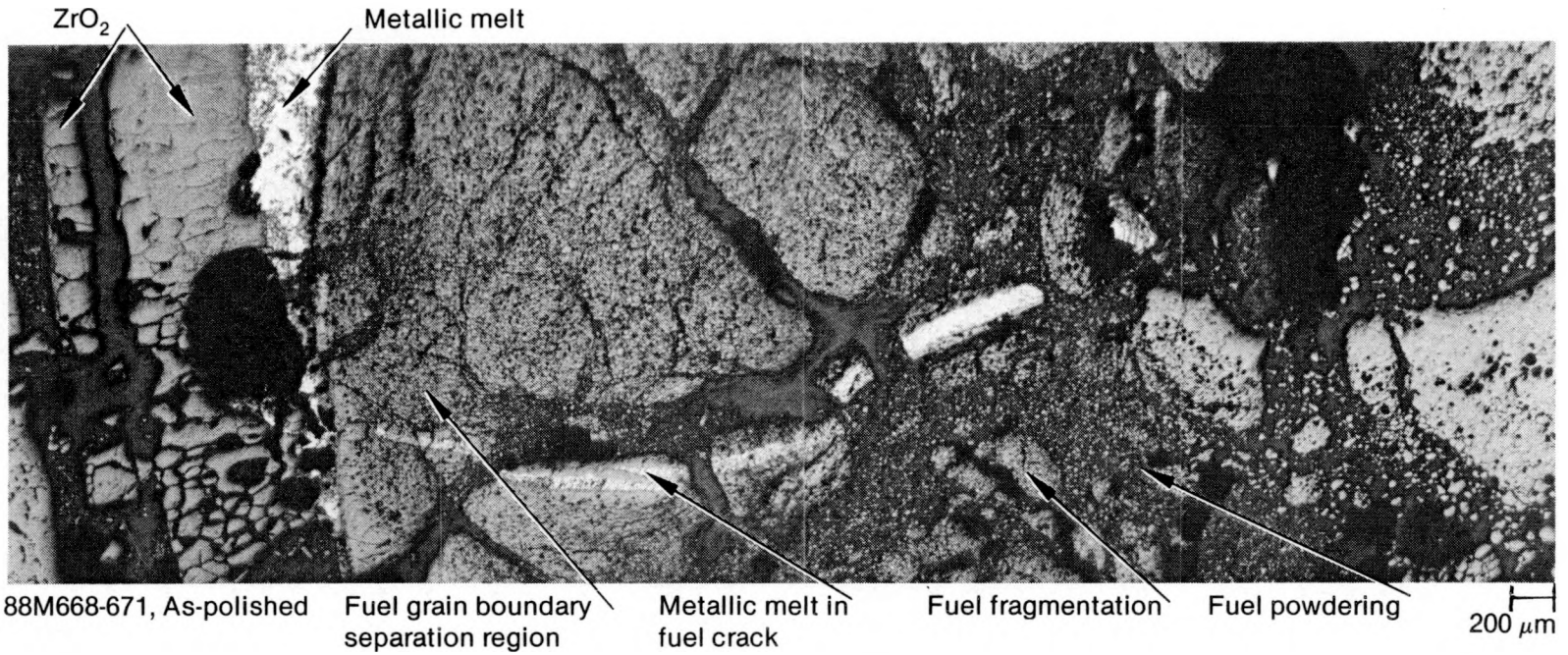

Figure 28. Fuel grain boundary separation, fragmentation, and powdering at 0.66 m.

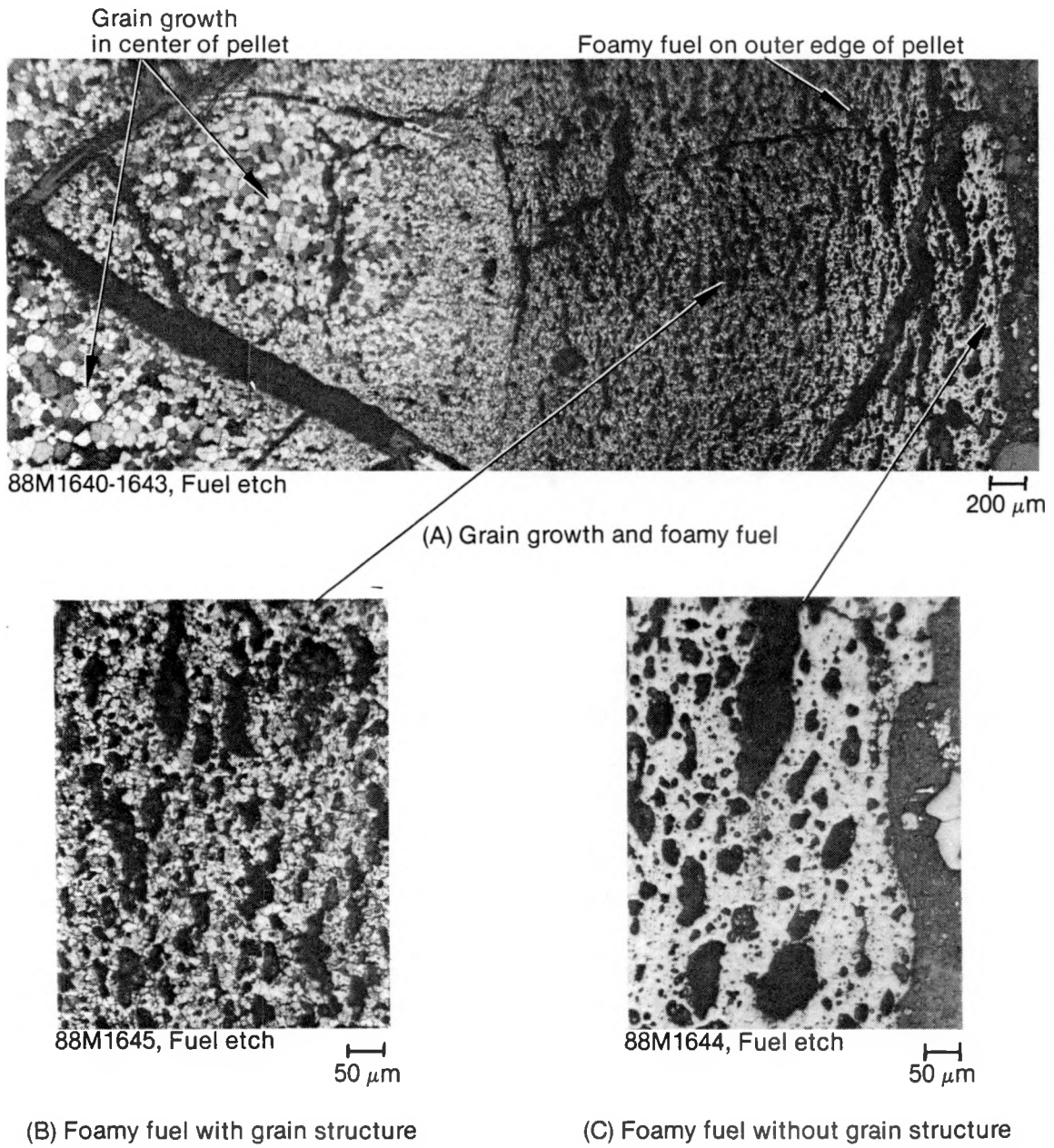

Figure 29. Foamy fuel structure on outer periphery of fuel pellet at 0.77 m.

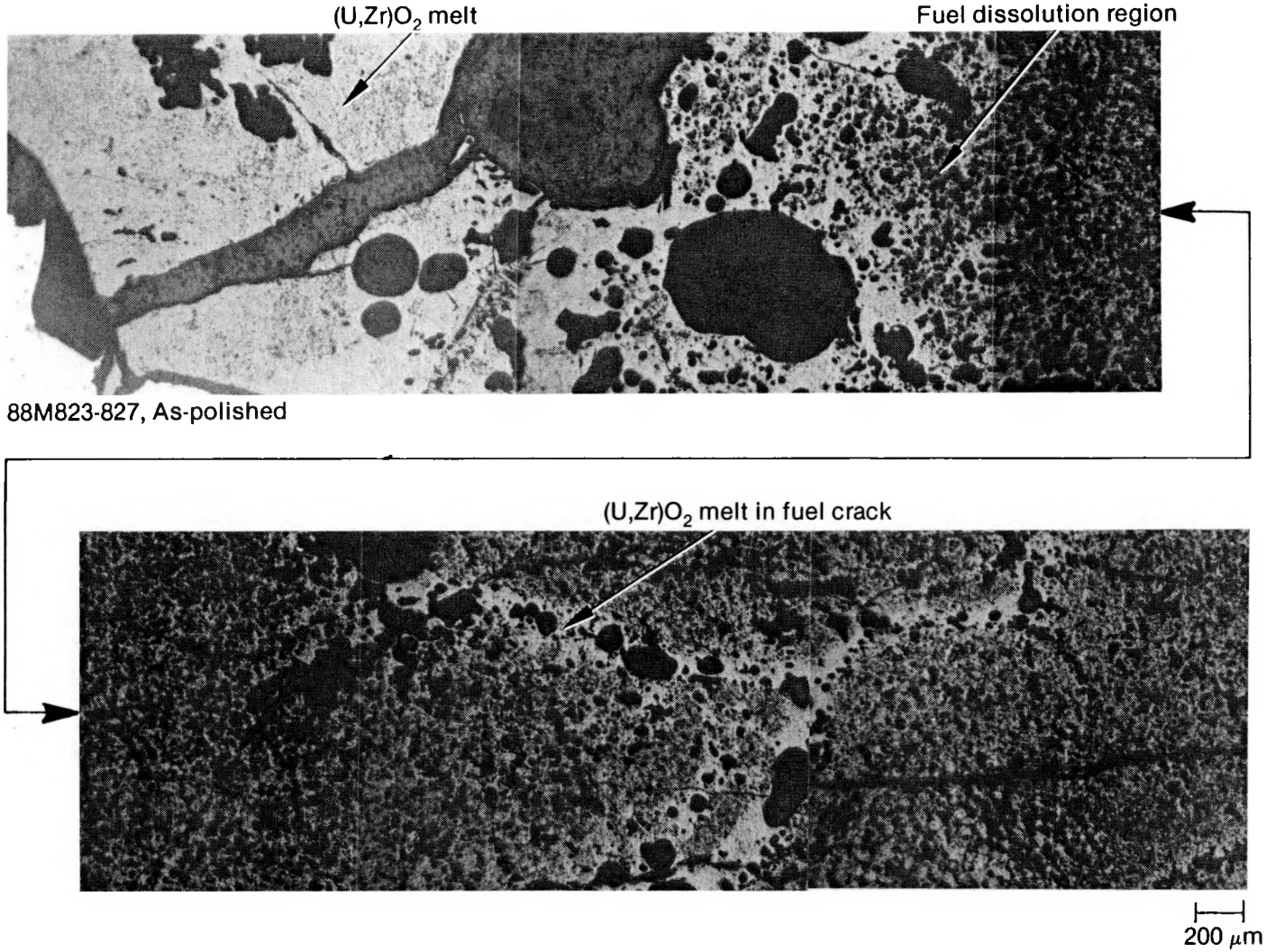

Figure 30. Fuel dissolution in $(U,Zr)O_2$ melt at 0.77 m.

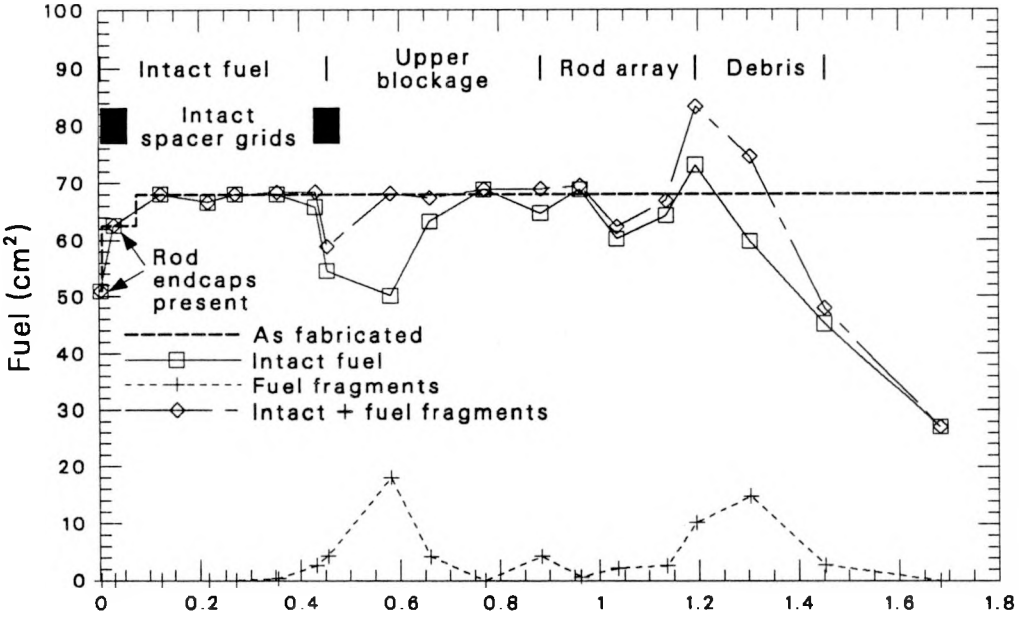

Figure 31. Fuel distribution

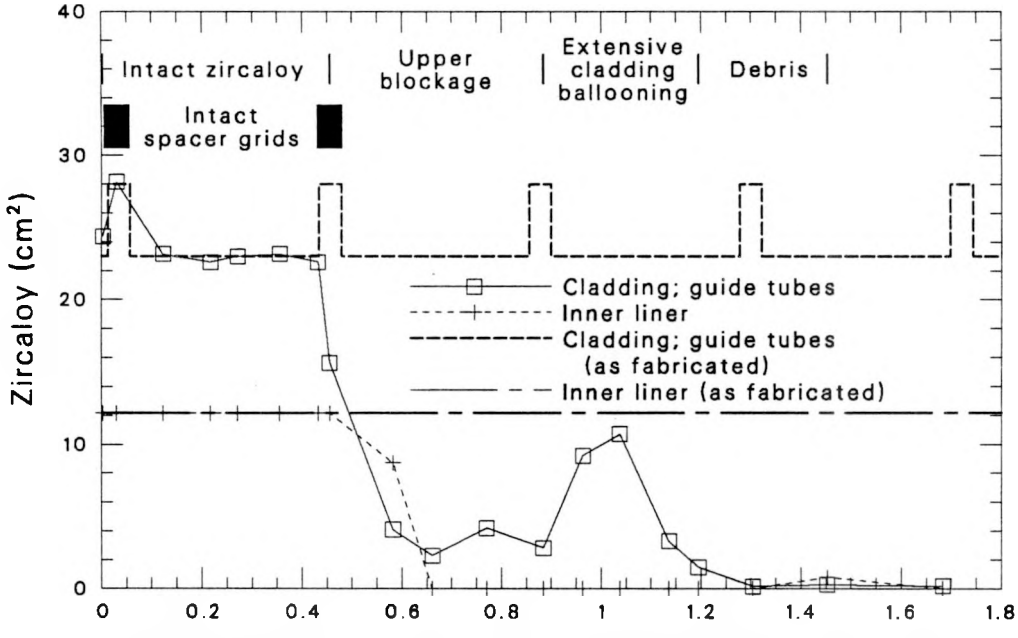

Figure 32. Zircaloy distribution

S202 SMJ-0490-05

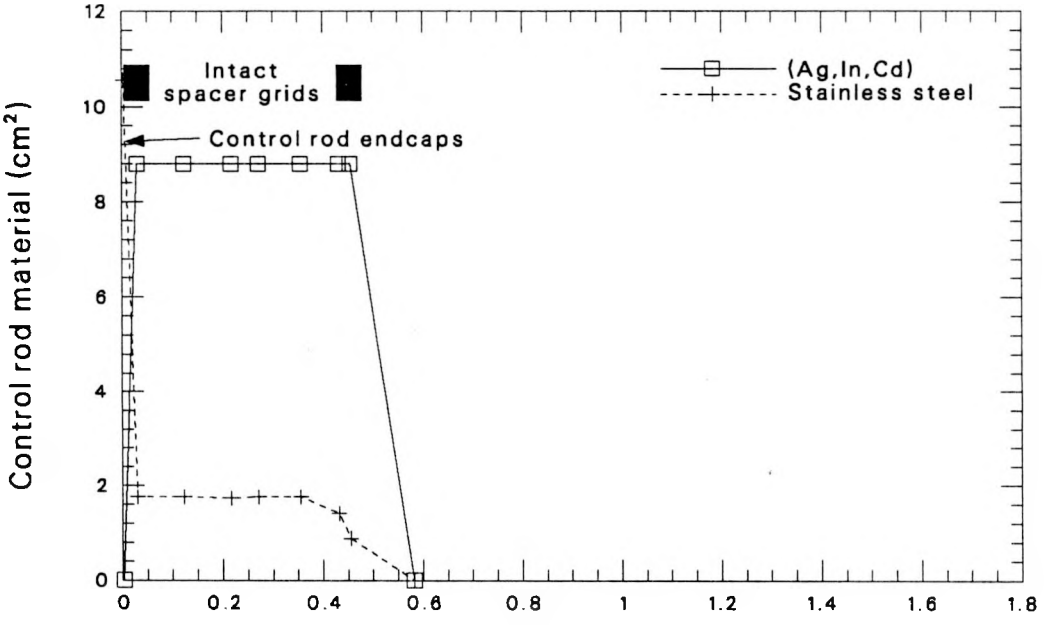

Figure 33. Distribution of control rod materials

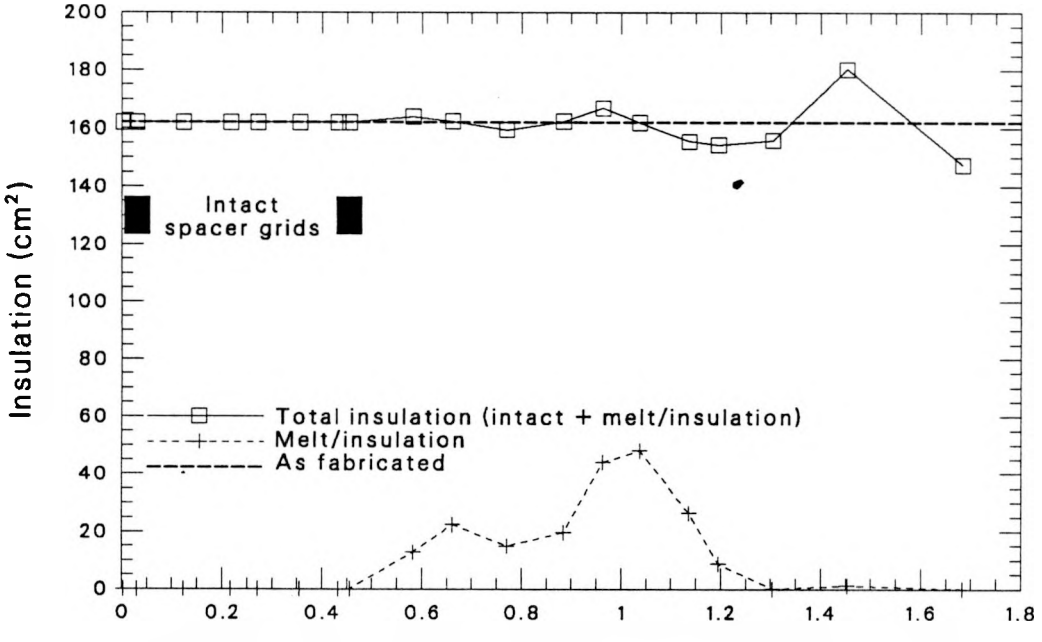

Figure 34. Distribution of insulation

S202 SMJ-0490-06

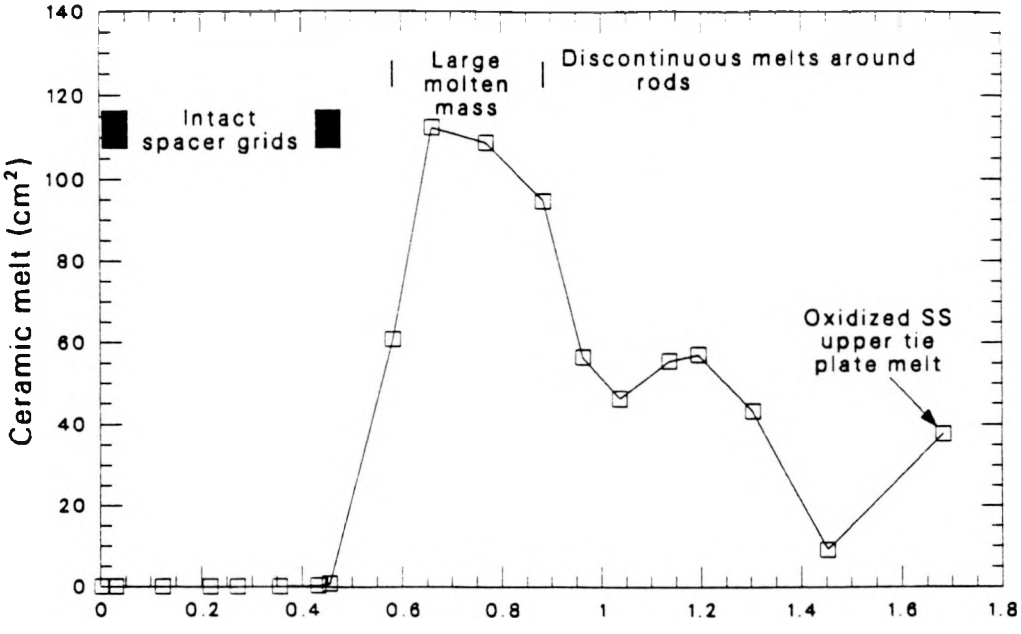

Figure 35. Ceramic melt distribution

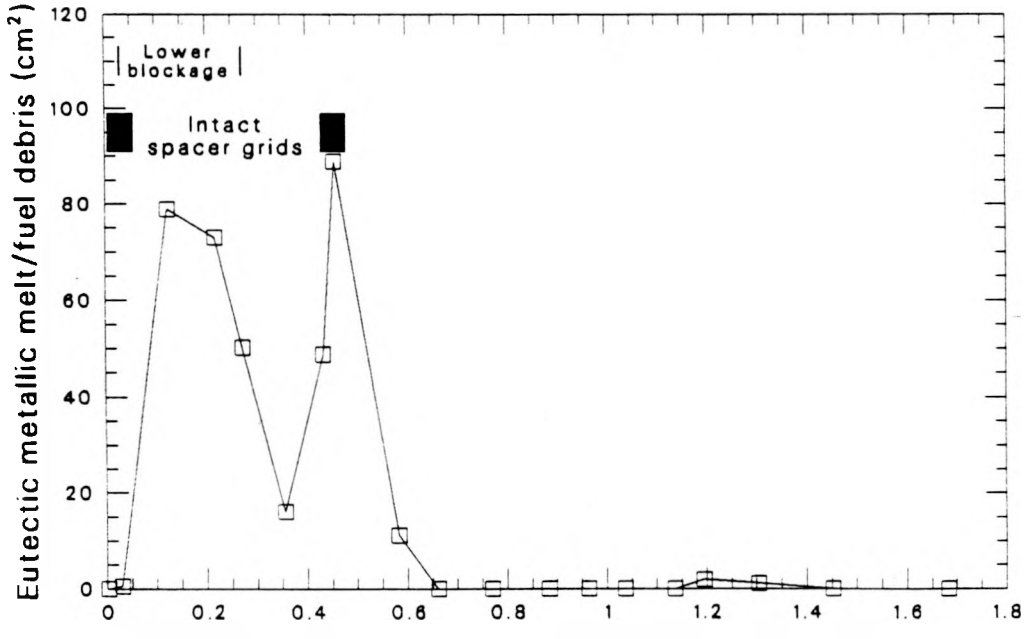

Figure 36. Distribution of eutectic melt/fuel debris

S202 SMJ-0480-03

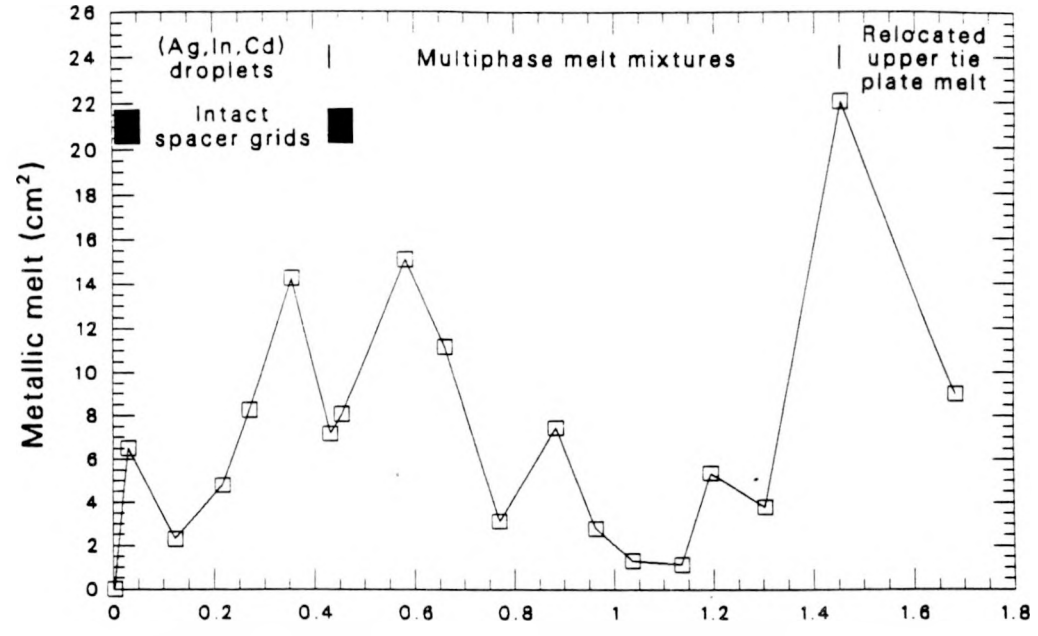

Figure 37. Distribution of metallic melt

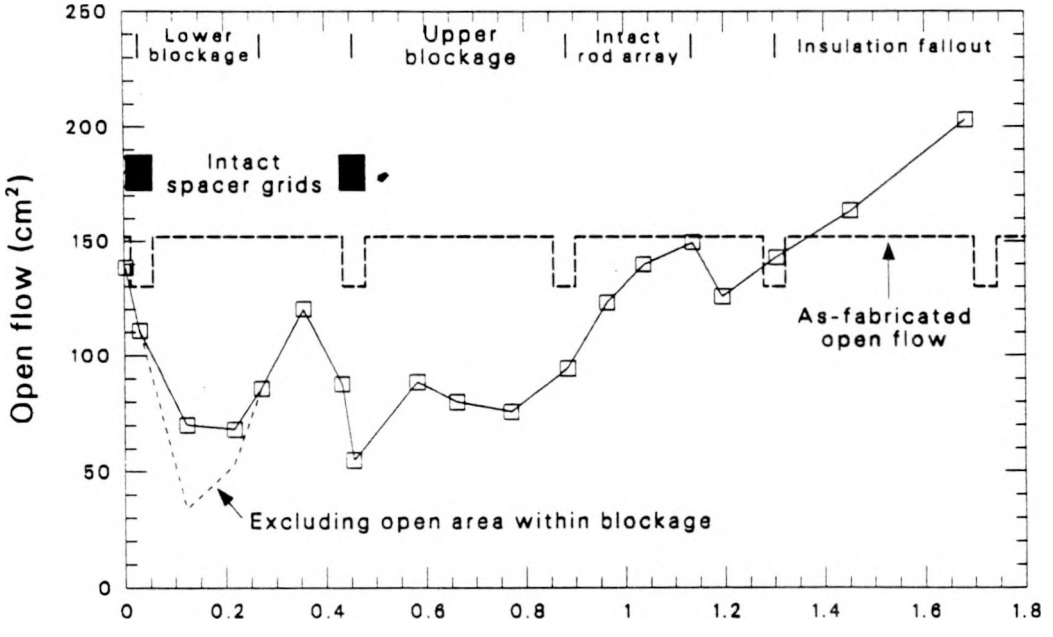

Figure 38. Posttest open flow distribution

S202 SMJ-0490-04

TABLE 1. INTEGRAL VOLUMES OF MATERIAL IN LP-FP-2

Material	Pretest (cm^3)	Lower Limit (cm^3)	Nominal (cm^3)	Upper Limit (cm^3)
Fuel				
Intact		8919 (79%)	10025 (89%)	11133 (99%)
Fuel fragments		495 (4%)	688 (6%)	908 (8%)
Total	11273	9414 (84%)	10713 (95%)	12041 (107%)
Zircaloy				
Cladding	4163	1363 (33%)	1575 (38%)	1806 (43%)
Liner	2207	758 (34%)	767 (35%)	776 (35%)
Control material				
Ag,In,Cd	1475	386 (26%)	442 (30%)	498 (34%)
Stainless steel	319	88 (28%)	88 (28%)	88 (28%)
Spacer grid	366	124 (34%)	126 (34%)	129 (35%)
Insulation				
Intact		25974 (91%)	27251 (95%)	28528 (100%)
Melt/insulation		1495 (5%)	1760 (6%)	2024 (7%)
Total	28585	27469 (96%)	29011 (101%)	30552 (107%)

TABLE 2. INTEGRAL VOLUME OF MELT AND DEBRIS IN LP-FP-2

Material	Lower Limit (cm^3)	Nominal (cm^3)	Upper Limit (cm^3)
Ceramic melt	6070	6744	7418
Metallic melt	1181	1389	1598
Eutectic metallic melt/fuel debris	2517	2796	3076
Miscellaneous debris	10	20	30

TABLE 3. URANIUM MASS BALANCE IN LP-FP-2

Location	Low Estimate (g)	Nominal Estimate (g)	Upper Estimate (g)
Ceramic melt	1.5E4 (14%)[a]	1.8E4 (15%)[a]	2.2E4 (16%)[a]
Eutectic melt/fuel debris	2.1E3 (2%)	2.3E3 (2%)	2.6E3 (2%)
Metallic melt	3.8E2 (0.3%)	9.6E2 (1%)	2.1E3 (2%)
Intact fuel	8.2E4 (79%)	9.2E4 (77%)	1.0E5 (74%)
Fuel fragments	4.5E3 (4%)	6.3E3 (5%)	8.3E3 (6%)
Posttest total	1.0E5	1.2E5	1.4E5
Pretest total	1.0E5	1.0E5	1.0E5
Δ%	0%	20%	40%

a. Percentages are normalized to posttest total.

TABLE 4. ZIRCONIUM MASS BALANCE IN LP-FP-2

Location	Low Estimate (g)	Nominal Estimate (g)	Upper Estimate (g)
Ceramic melt	9.1E3 (28%)[a]	1.2E4 (29%)[a]	1.6E4 (32%)[a]
Eutectic melt/fuel debris	4.9E3 (15%)	5.4E3 (13%)	6.0E3 (12%)
Metallic melt	1.5E3 (5%)	3.0E3 (7%)	5.2E3 (10%)
Melt/insulation	4.1E3 (13%)	5.6E3 (14%)	6.9E3 (14%)
Intact cladding and liner	1.3E4 (40%)	1.5E4 (37%)	1.6E4 (32%)
Posttest total	3.3E4	4.1E4	5.0E4
Pretest total	4.1E4	4.1E4	4.1E4
Δ%	-20%	0%	22%

a. Percentages are normalized to posttest total.

TABLE 5. BEST ESTIMATE OF HYDROGEN GENERATION FROM ZIRCALOY

	H_2 (g)		
	Lower	Nominal	Upper
Upper limit from zircaloy oxidation = 1226 g			
Unoxidized Zr in eutectic metallic melt	-197	-118	-54
Unoxidized Zr in melt/insulation	-226	-114	-42
Unoxidized Zr in metallic melts	-228	-132	-66
Total hydrogen from zircaloy oxidation	575	862	1064

TABLE 6. HYDROGEN GENERATION FROM ZIRCALOY OXIDATION IN VARIOUS REGIONS OF LP-FP-2[a]

	LOWER	NOMINAL	UPPER
Oxidized ZrO_2 cladding shells	36	63	93
Eutectic metallic melt	54	118	197
Ceramic melt in large blockage (<0.92m)	225	327	471
Ceramic melt above large blockage (>0.92m)	175	195	214
Melt/insulation	56	133	229
Total from Zirconium	546	836	1204

a. These values were calculated using alternate methods than those used to estimate the hydrogen from zircaloy oxidation in Table 5.

TABLE 7. OXIDATION OF NONZIRCALOY COMPONENTS

	H_2 (g)		
	Lower	Nominal	Upper
Oxidation of SS upper tie plate	51	103	155
Oxidation of molten SS cladding	20	40	60
Oxidation of molten spacer grid	9	20	31
Total hydrogen from nonzircaloy components	80	163	246

TABLE 8. BEST ESTIMATE OF TOTAL HYDROGEN PRODUCTION IN LP-FP2

	H_2 (g)		
	Lower	Nominal	Upper
Upper limit from zircaloy oxidation = 1226 g			
Unoxidized Zr in eutectic metallic melt	-197	-118	-54
Unoxidized Zr in melt/insulation	-226	-114	-42
Unoxidized Zr in metallic melts	-228	-132	-66
Total hydrogren from zircaloy	575	862	1064
Oxidation of SS upper tie plate	51	103	155
Oxidation of molten SS cladding	20	40	60
Oxidation of molten spacer grid	9	20	31
Total hydrogen from nonzircaloy components	80	163	246
Total hydrogen generation in LP-FP-2	655	1025	1310

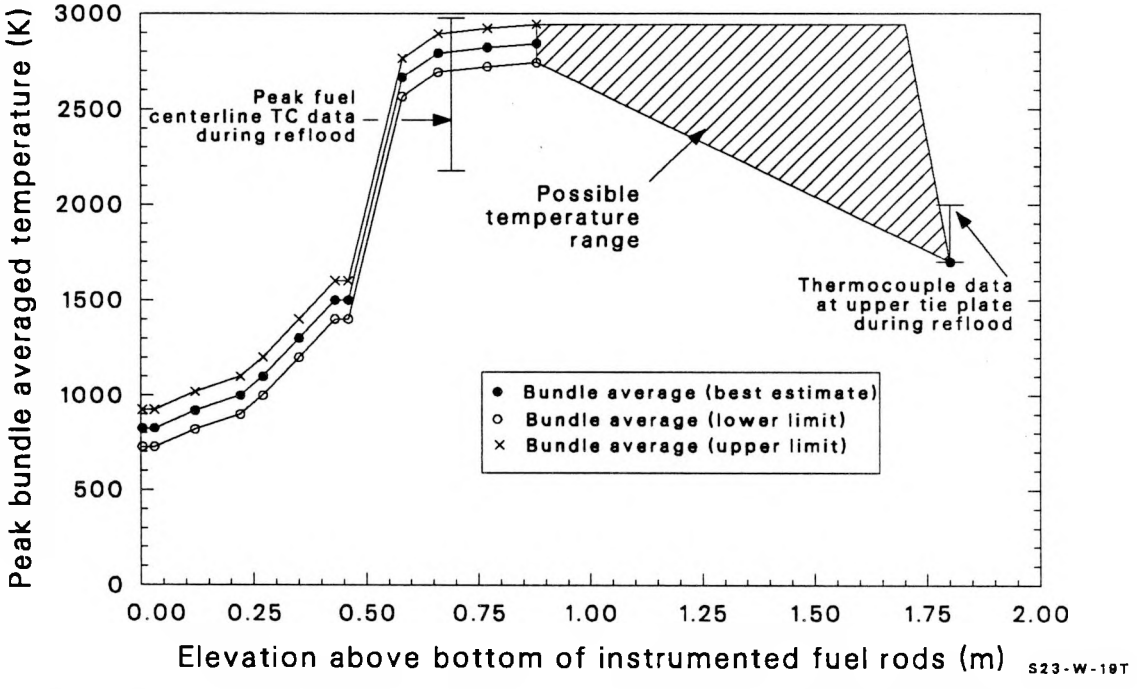

Figure 39. Axial peak bundle averaged temperature distribution

CONF-9005179

Postirradiation Examination Results from the LP-FP-2 Center Fuel Module

AC07-76ID01570

By:

S. M. Jensen

OECD LOFT Conference

Madrid, Spain

May, 1990

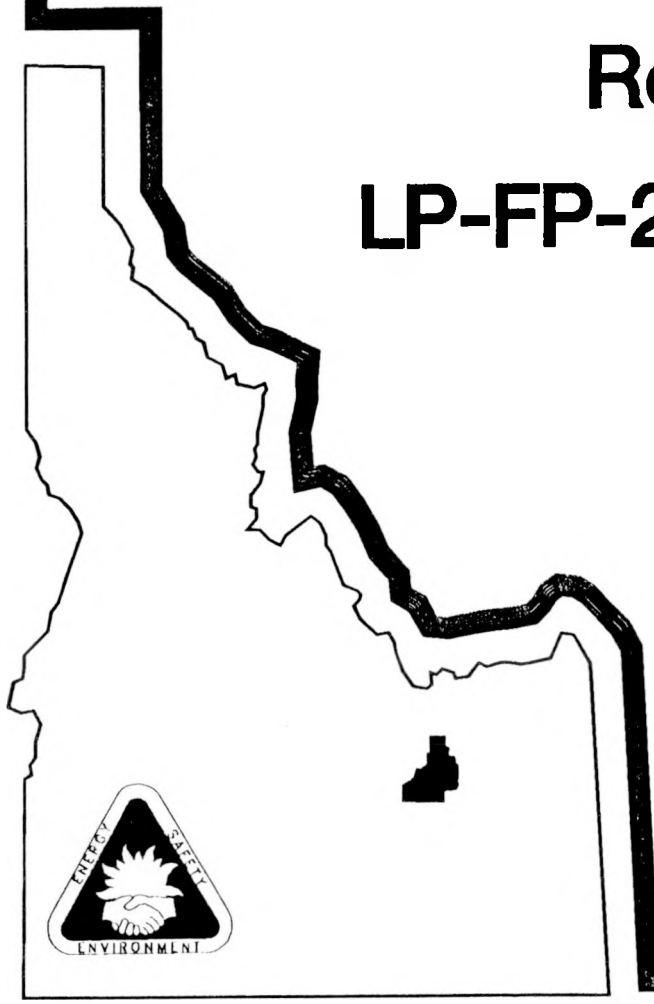

EG&G Idaho, Inc.

Attachment 6
May 22, 1990
SMJ-09-90

Outline

- Fuel bundle description
- Objectives and scope of postirradiation examinations
- Overall characteristics
- Material distribution
- Material interactions
- Oxidation and hydrogen generation
- Fuel grain size
- Peak bundle average temperatures
- Retained fission product analyses
- Summary

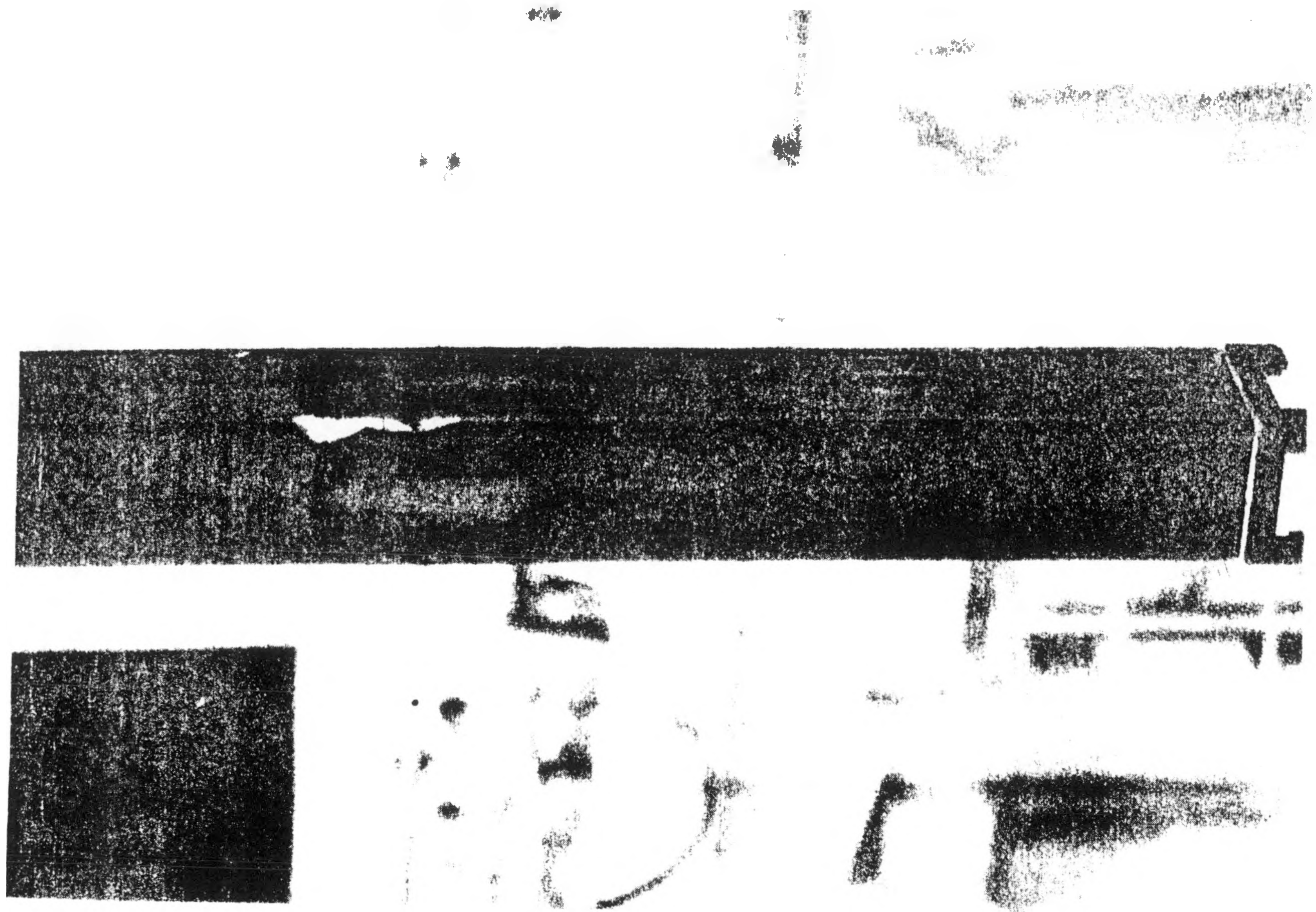

LP-FP-2 Bundle Cross-Section

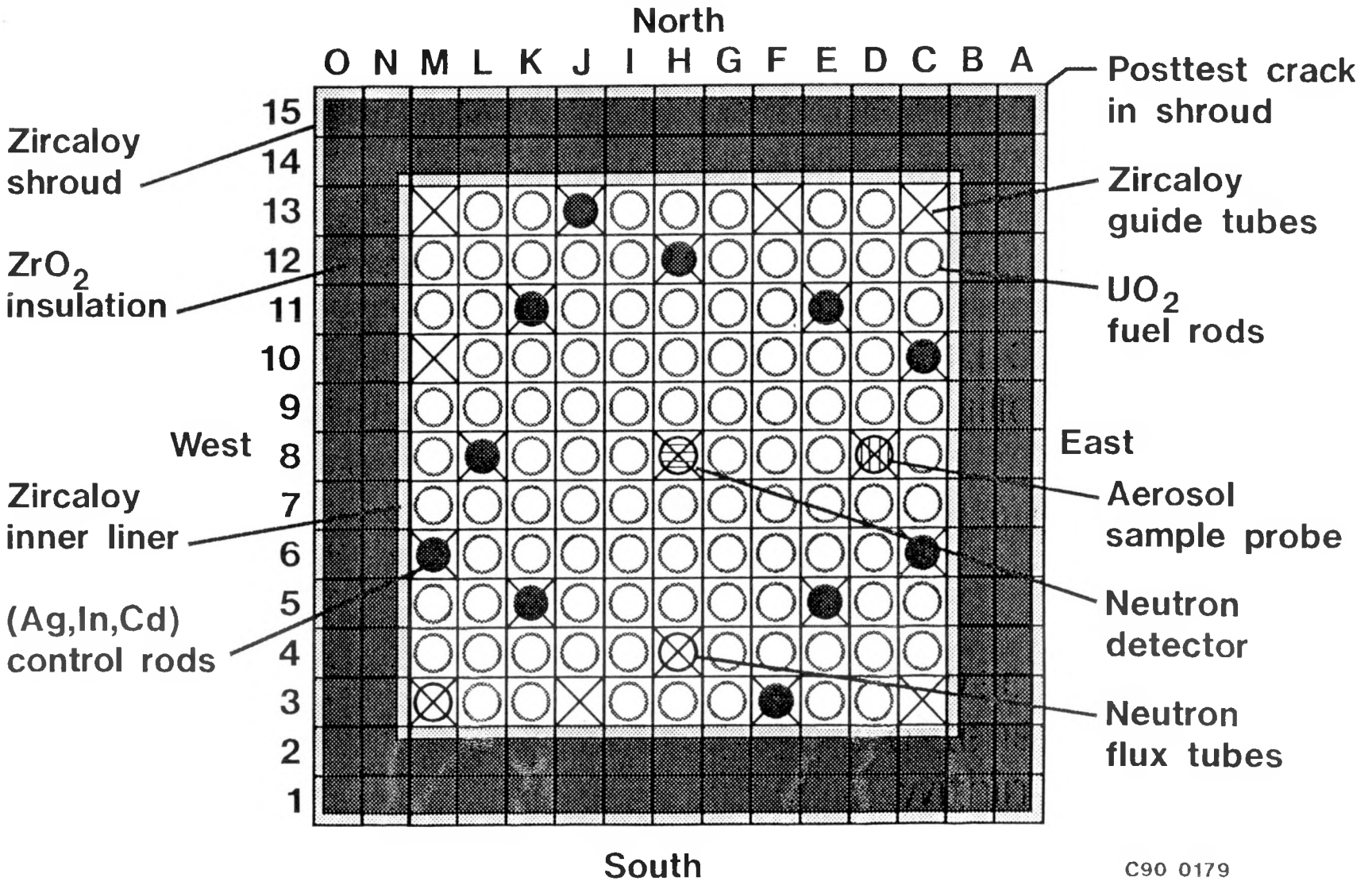

Postirradiation Examination Program Objectives

- Distribution of fuel and control rod materials
- Metallurgical and chemical form of materials
- Maximum temperatures throughout the bundle
- Retained fission product concentrations in specific materials

S23-WHT-889-03

Scope of Examinations

- Visual examinations
- Fuel bundle gamma scans
- Neutron radiographs at 2 angles
- 19 cross-sectional metallographic slabs
- 76 quartered samples (polish and photograph 84 surfaces)
- 42 metallographic samples
- 30 retained fission product samples
- 30 scanning electron microscope samples

S220-WHT-490-03

LP-FP-2 (North view)

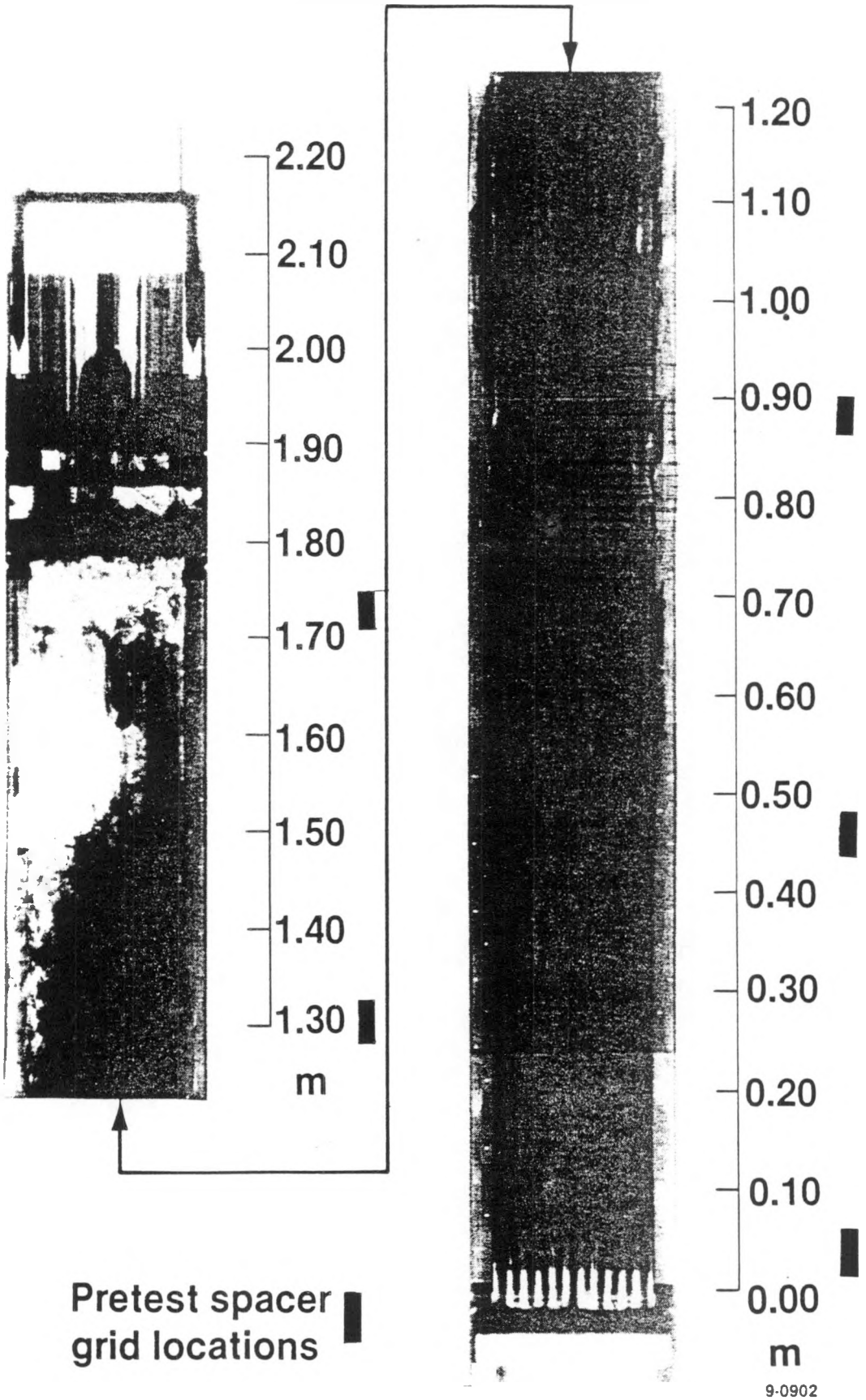

LP-FP-2 (East view)

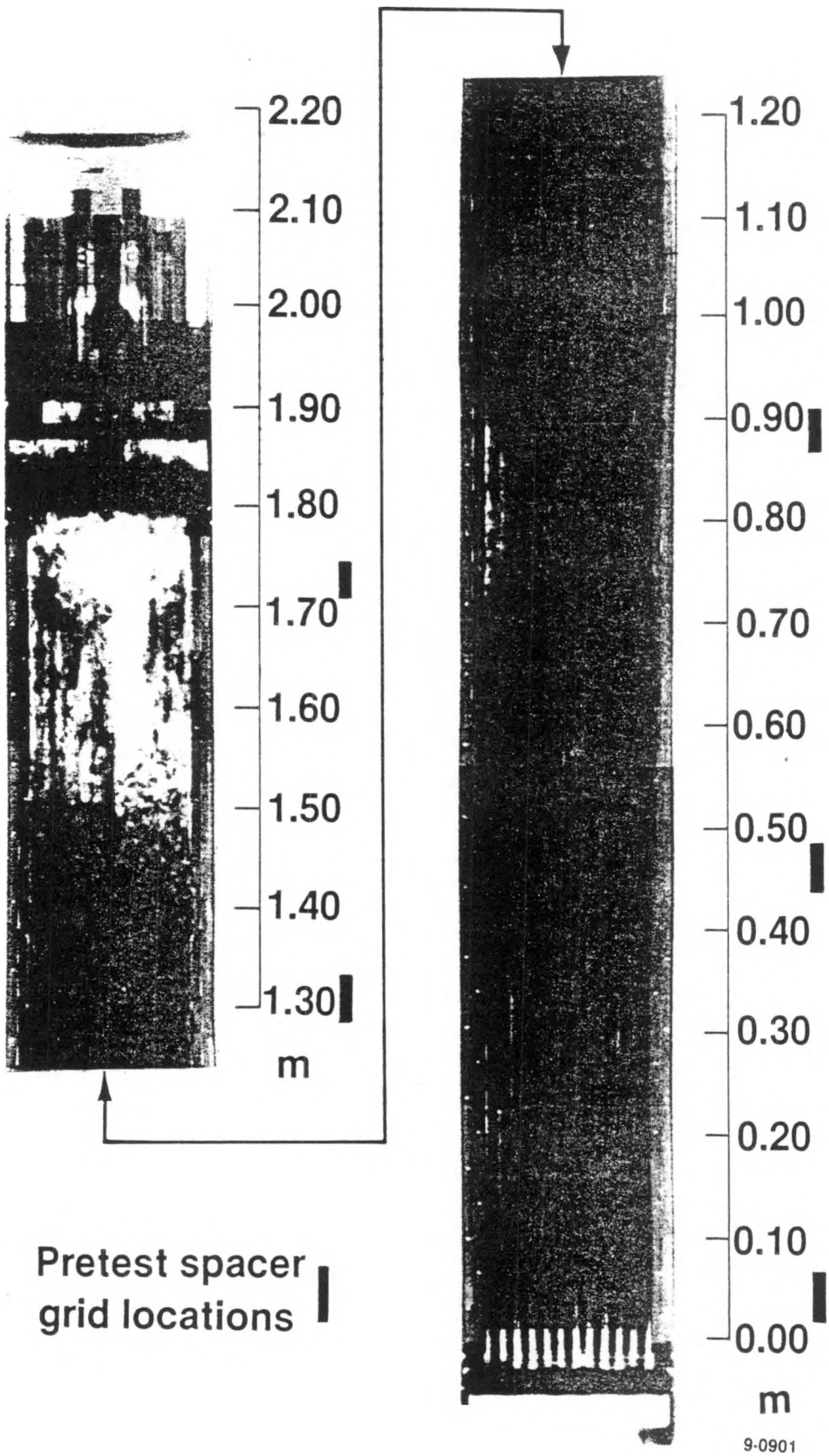

Overall Characteristics

- ($<$ 0.1 m): intact rod array and no interactions at lowest spacer grid and below

- ($\sim$ 0.1 - 0.23 m): lower blockage situated on lowest spacer grid primarily composed of metallic melts and fuel debris
  - zircaloy cladding oxidation observed on central rods within blockage

- ($\sim$ 0.23 - 0.44 m): intact rod array between blockages
  - zircaloy oxidation becomes more extensive
  - molten control material contained within cladding

S23-WHT-889-04

Overall Characteristics (continued)

- (~ 0.44 - 0.85 m): upper blockage situated on second spacer grid primarily composed of fuel rods surrounded by ceramic melt
  - ceramic melt temperatures were > 2800 K, with peak temperature ~ 3120 K
  - all remaining zircaloy above 27 inch thermocouple location was fully oxidized
  - all control rods ruptured above second spacer grid
  - fuel grain boundary separation and fragmentation occurred
- (~ 0.85 - 1.15 m): extensive cladding ballooning and rupture in region above upper blockage
- (~ 1.15 - 1.70 m): debris bed consisted of fuel pellets surrounded by small amounts of ceramic melt
- (1.8 m): stainless steel upper tie plate was molten and oxidized

Bottom Spacer Grid Remained Intact (0.03m)

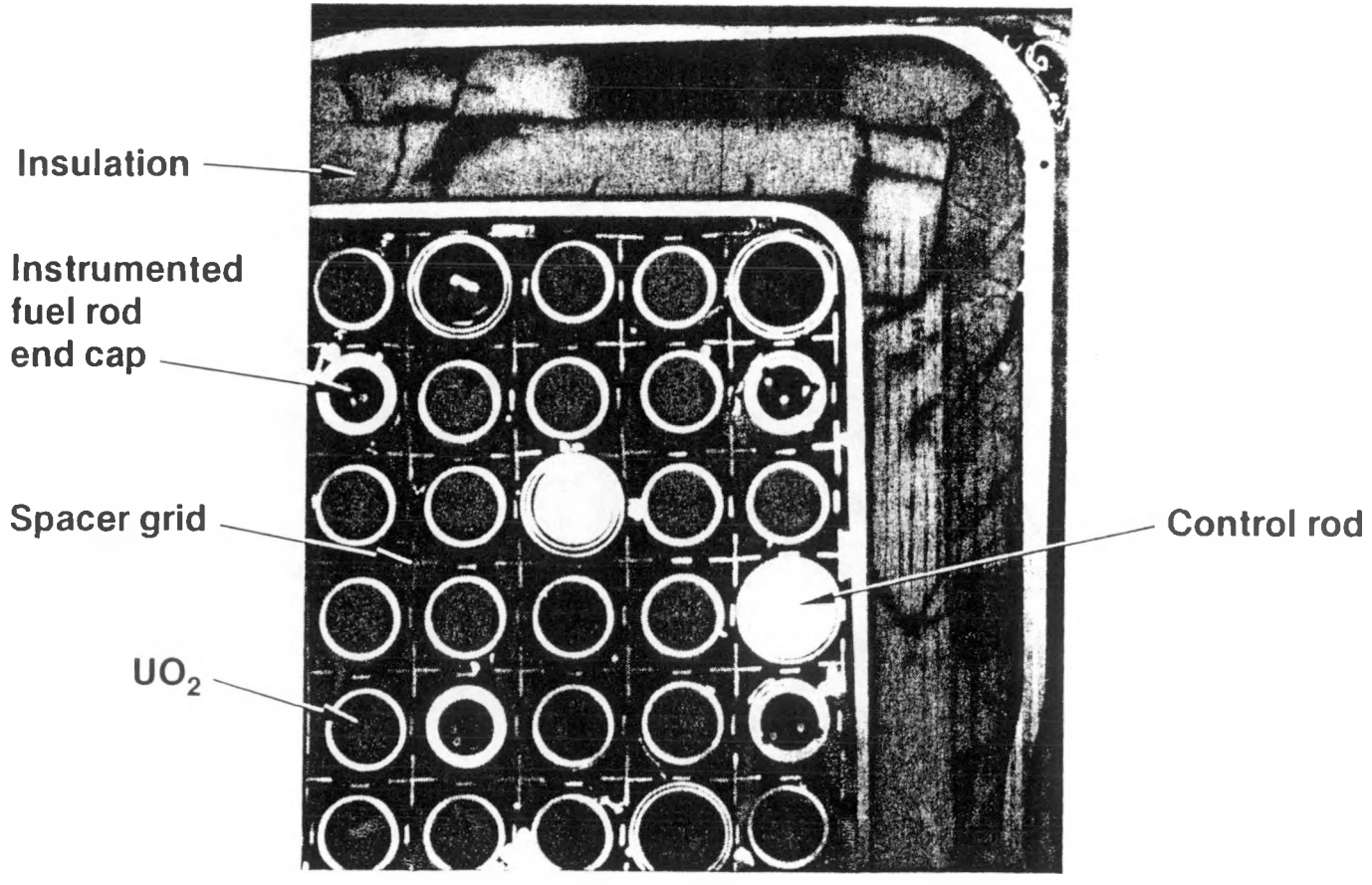

9-0288

Metallic Melts and Fuel Debris Formed Lower Blockage (0.12m)

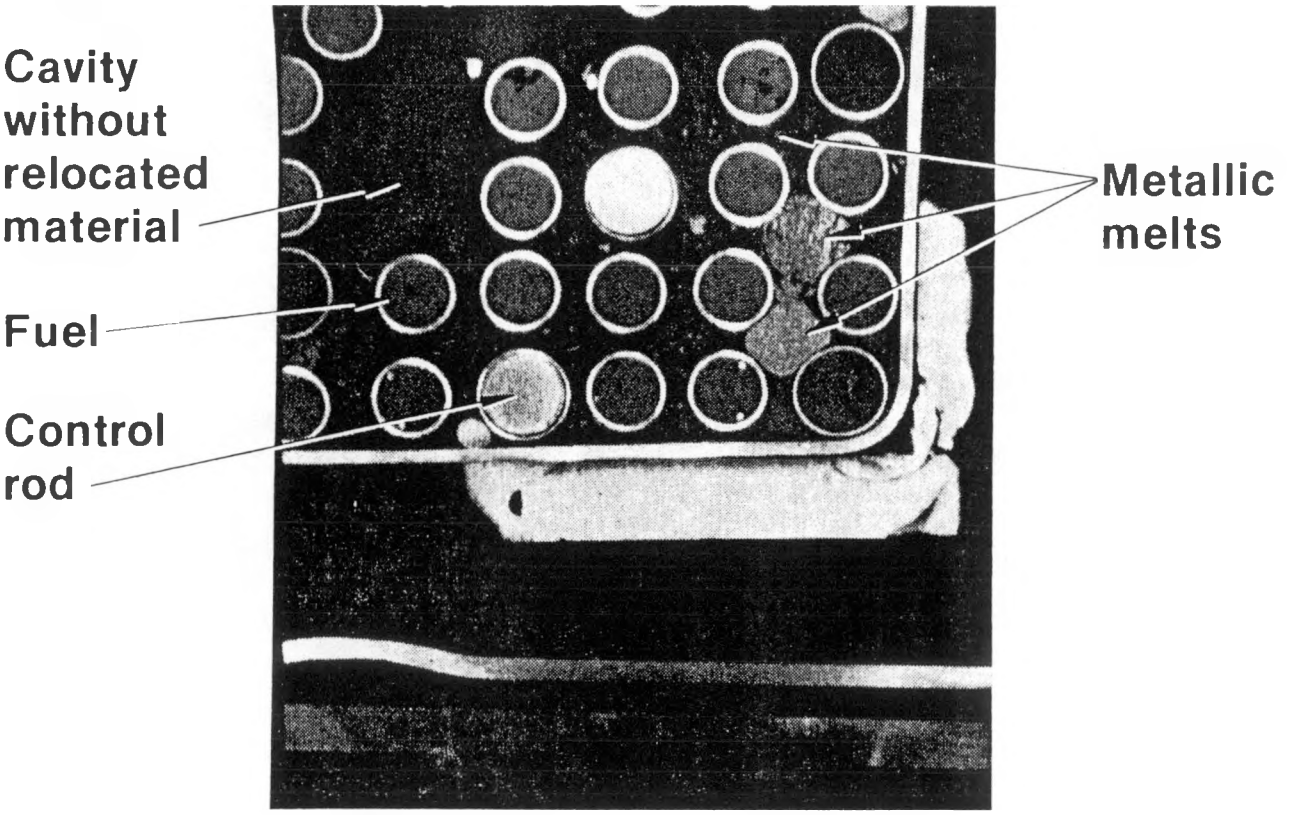

8-4573

Lower Blockage Was Primarily Composed of Eutectic Metallic Melts

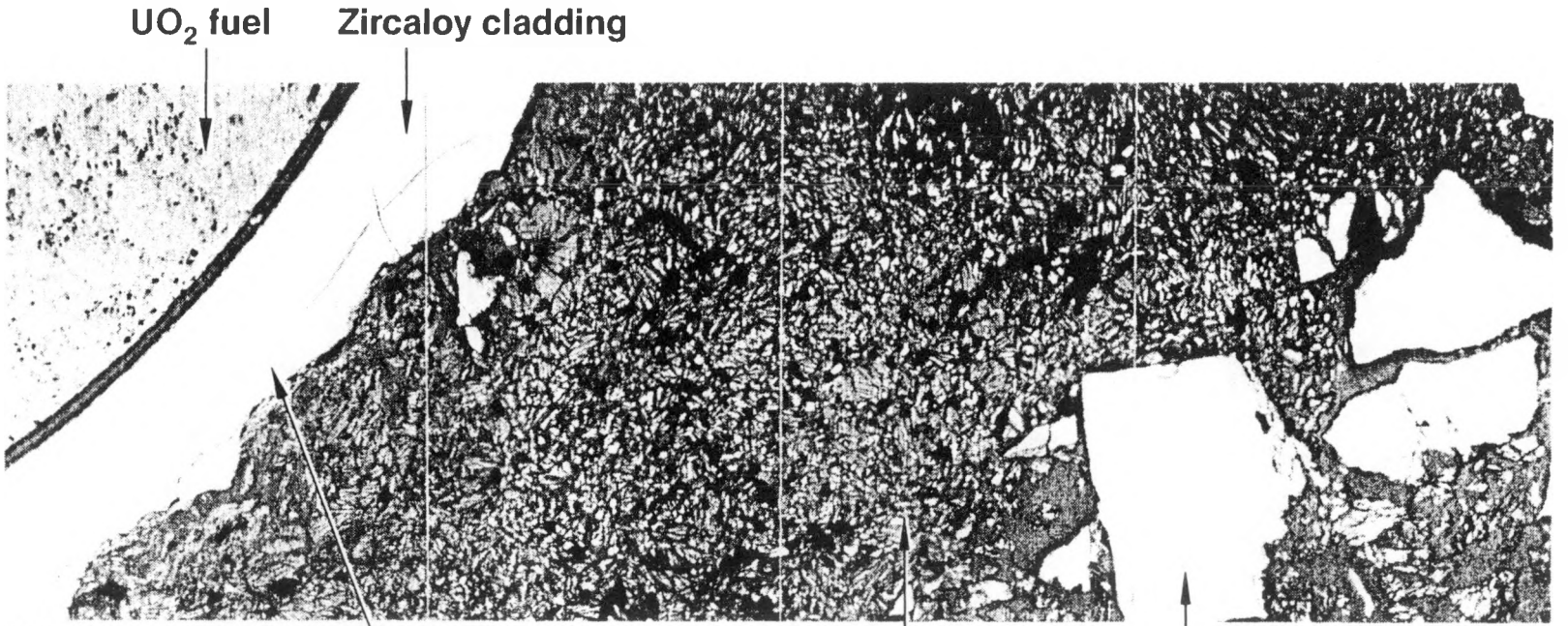

0-0369

Metallic Eutectic Melts Formed Lower Blockage

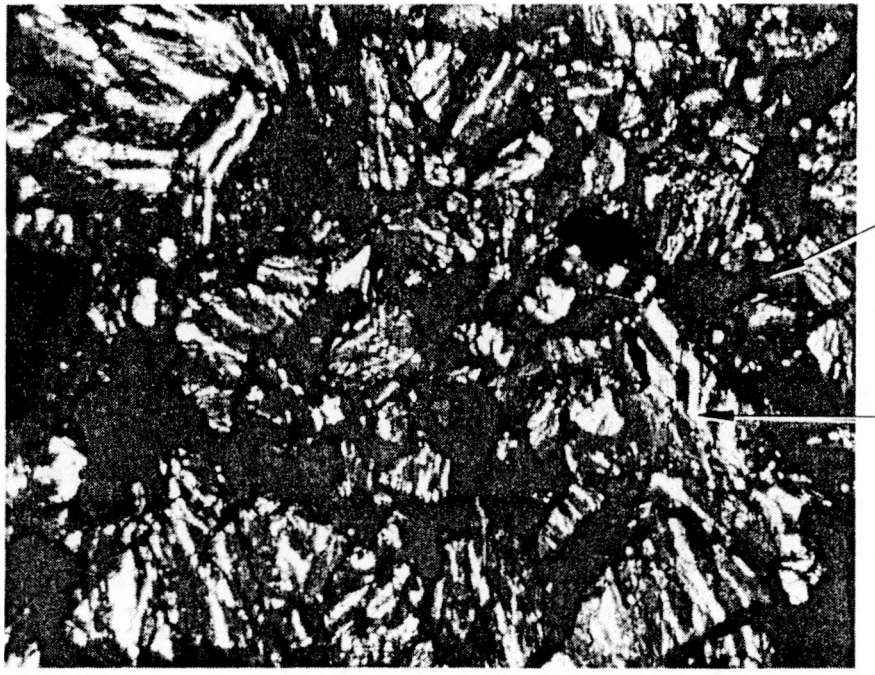

0-0365

Intact Rod Region Existed Between Blockages (0.36m)

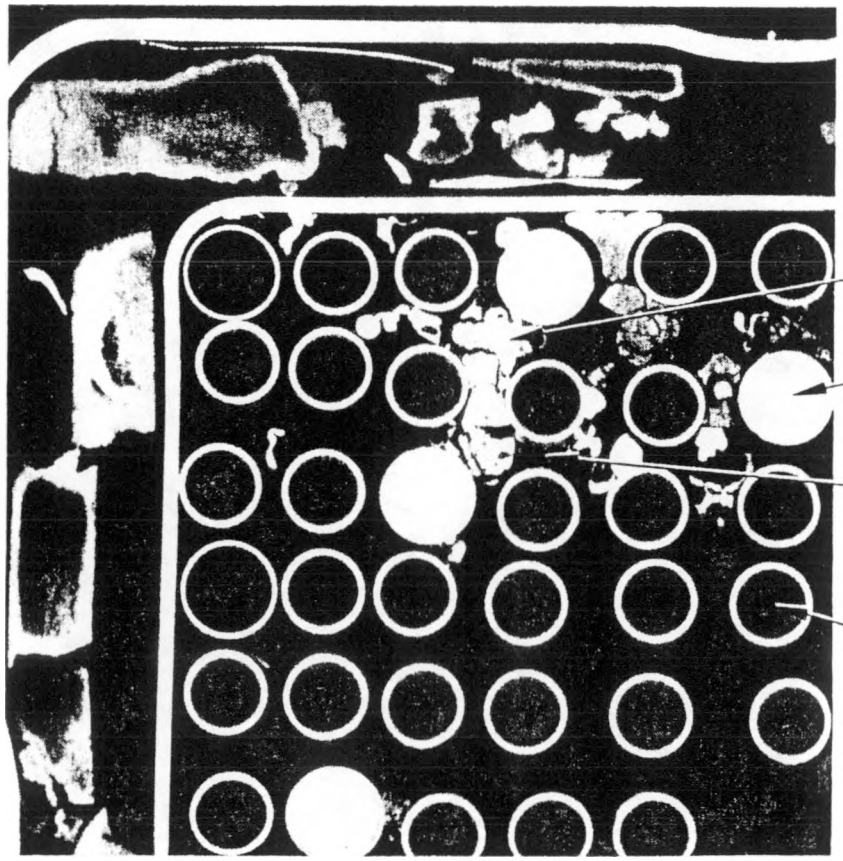

9-0289

Second Spacer Grid Was Partially Liquefied and Impeded Material Relocation (0.46m)

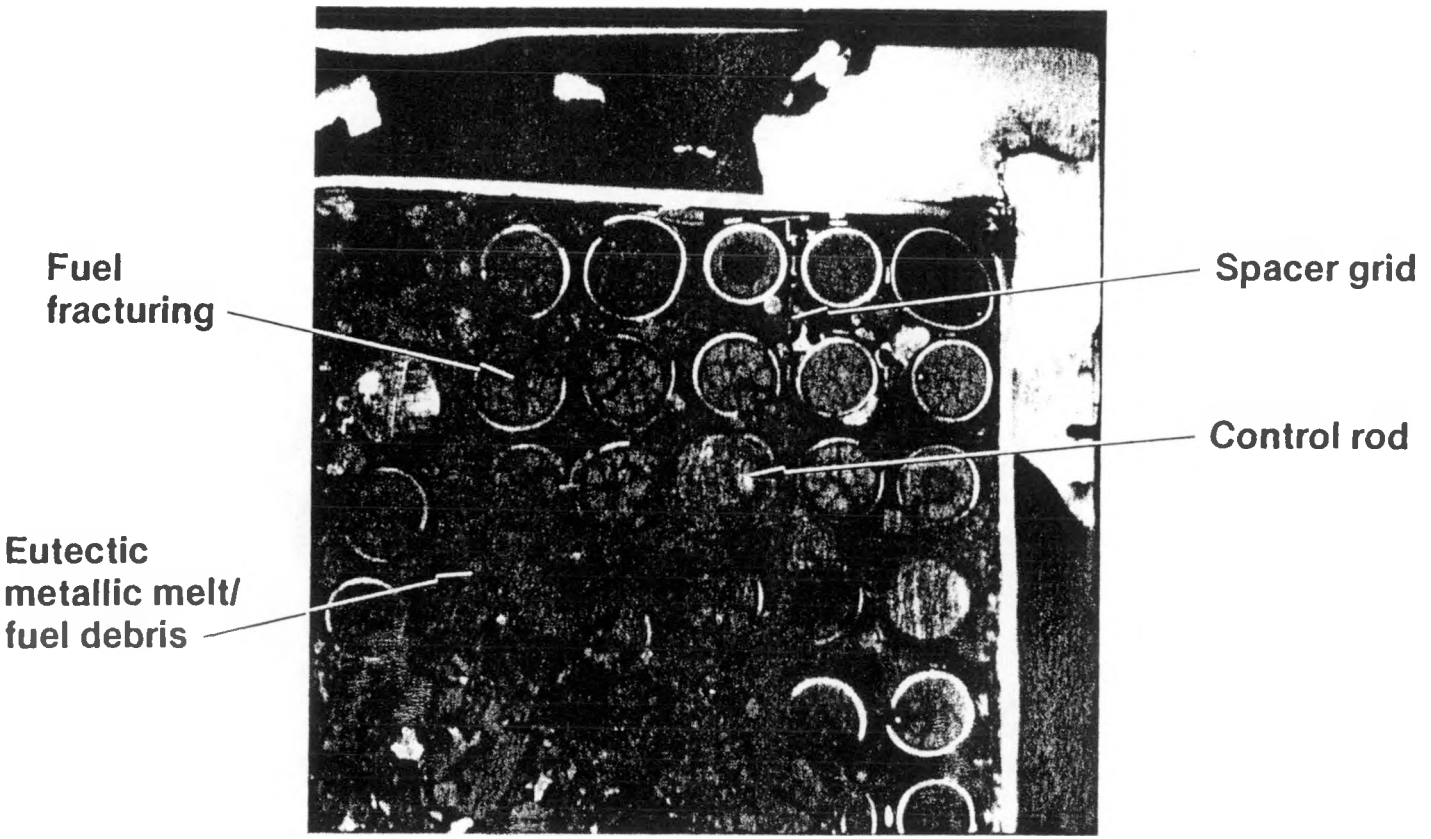

9-0286

LP-FP-2
Severe Fuel Damage Test

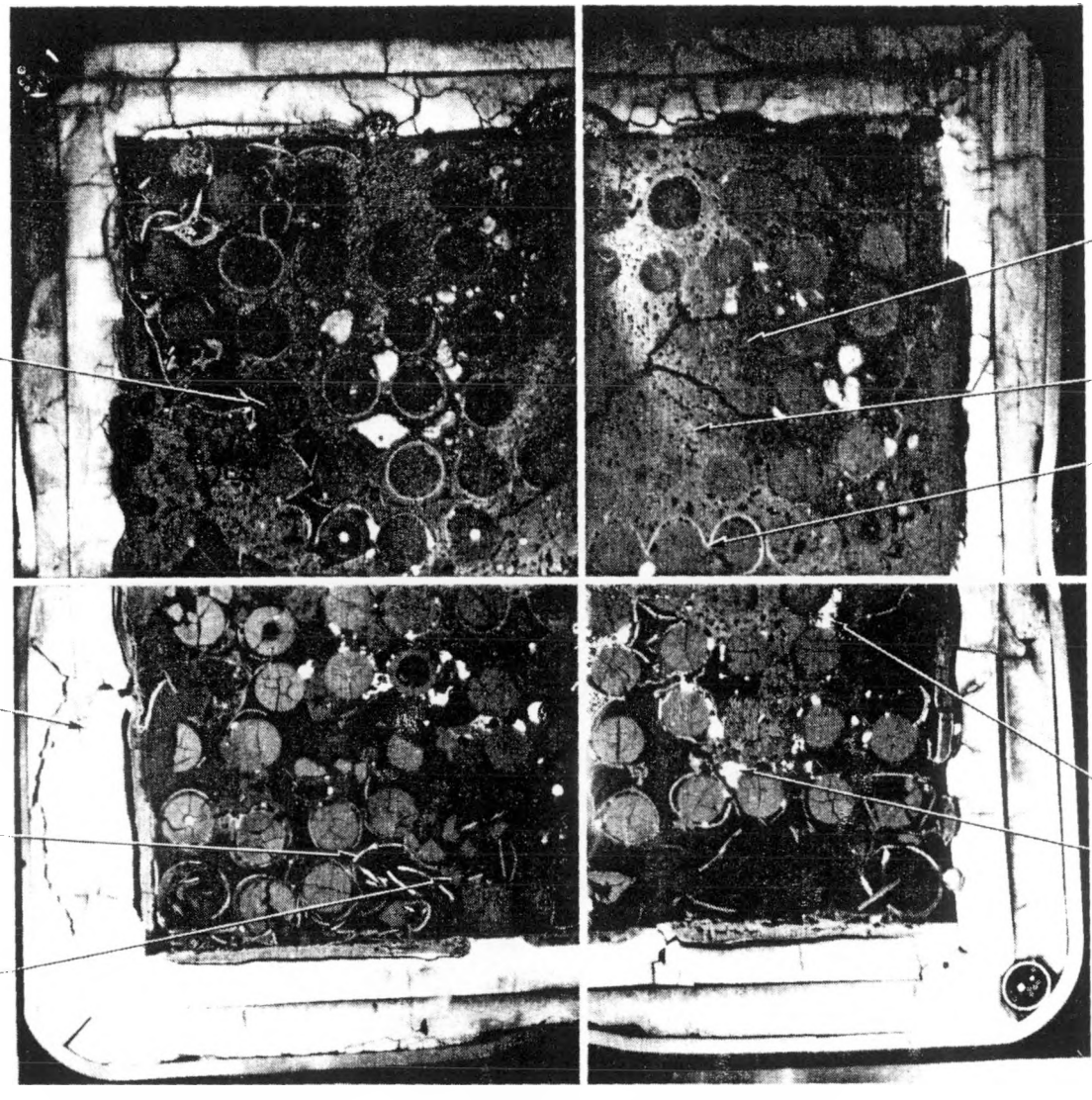

77 cm above bottom of instrumented fuel rods

Ceramic Melt/Fuel/Cladding Interaction in Upper Blockage

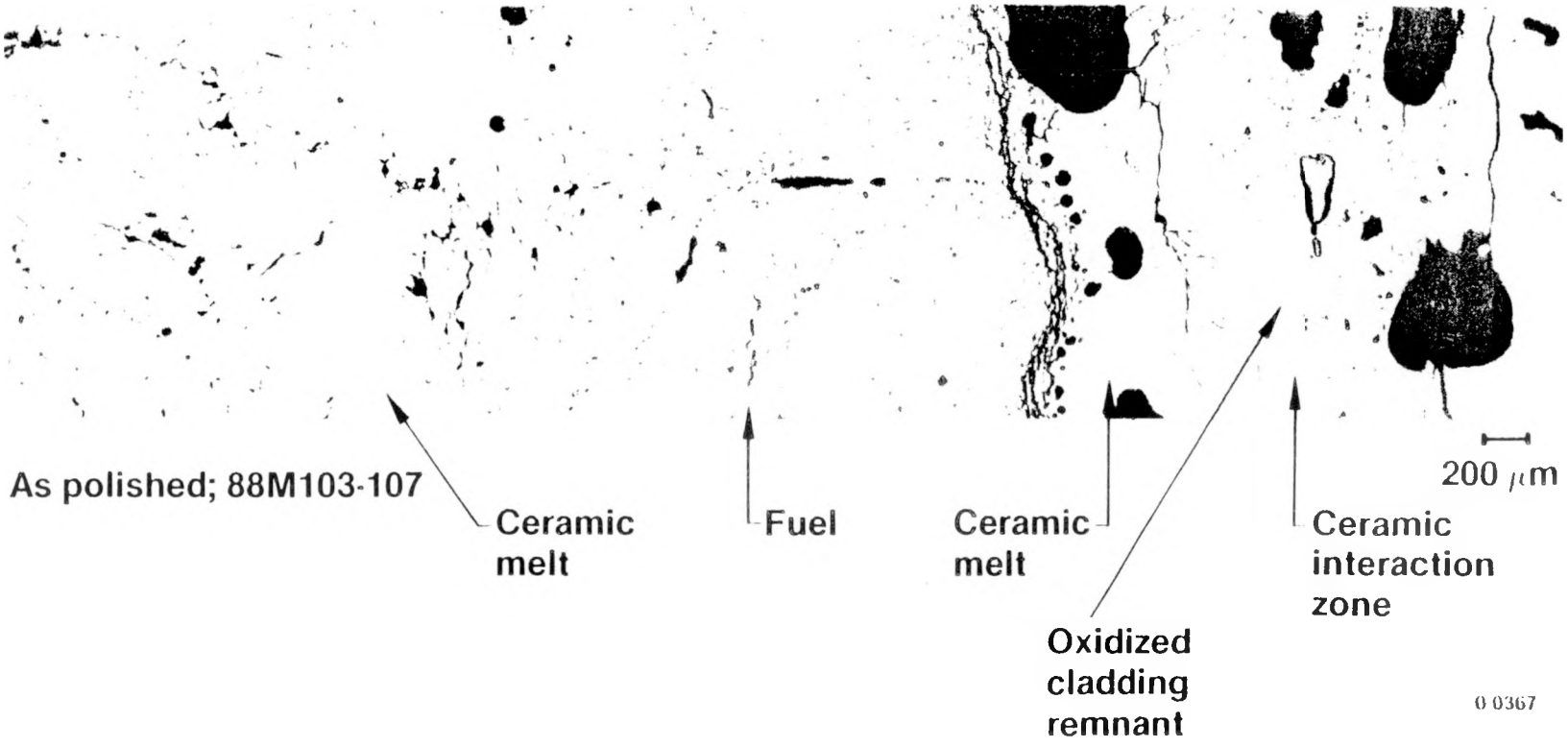

Extensive Cladding Ballooning Occurred in Bundle (1.04m)

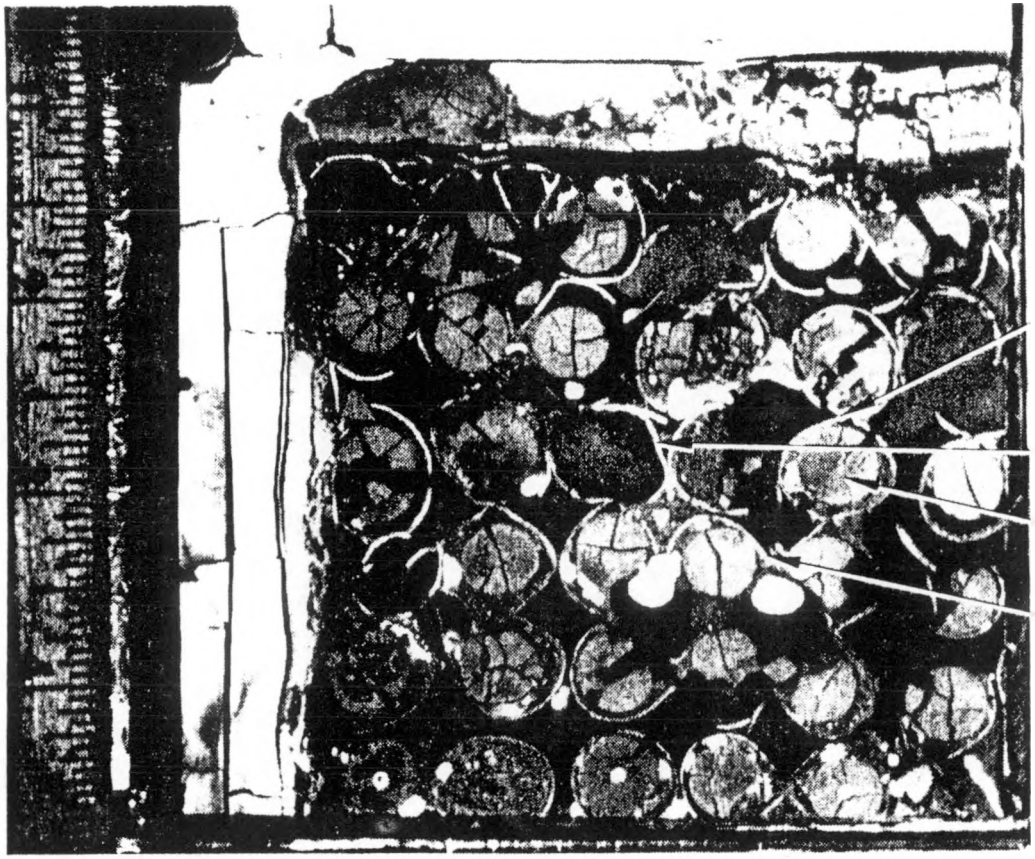

8 4566

Debris Bed Formed in the Upper Bundle (1.3m)

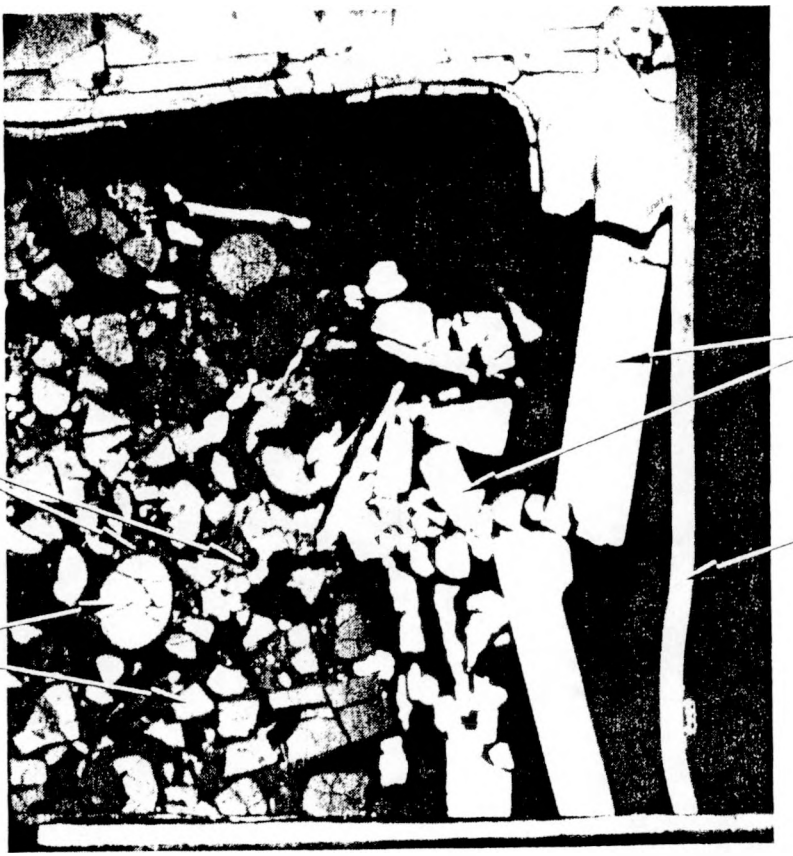

9 0287

Stainless Steel Upper Tie Plate Melted and Oxidized During Reflood (1.8m)

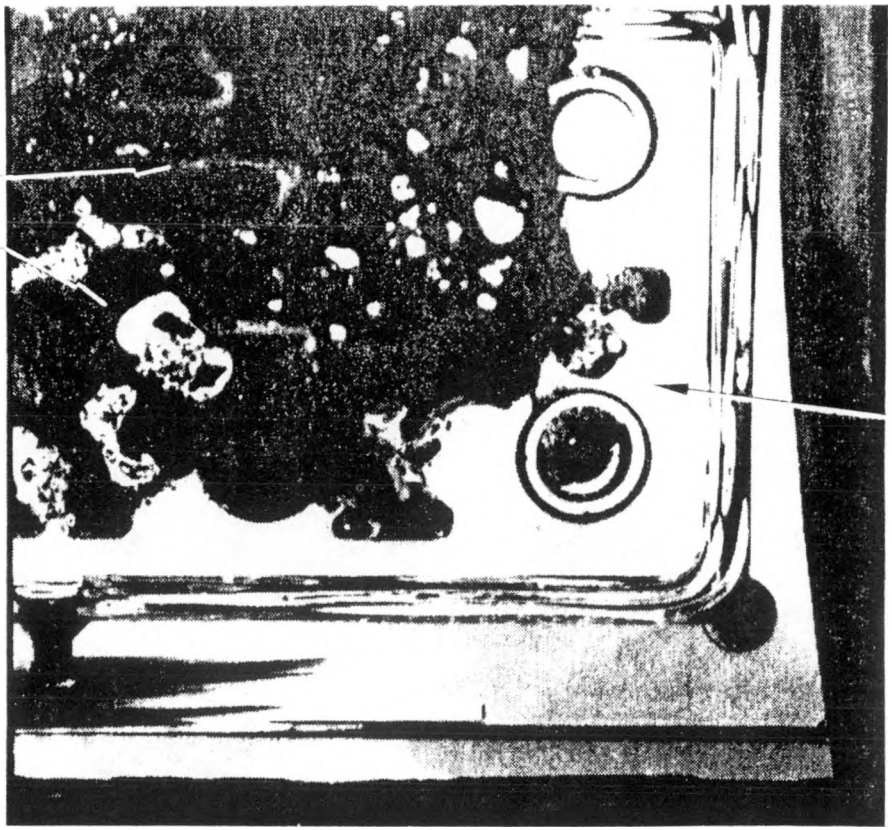

8-4568

Fuel and Melt Debris Relocated to Upper End Box During Reflood

Upper support structure

Relocated debris

Upper end box

Reflood caused significant damage to upper tie plate.

- Thermocouples indicate temperatures <1000 K during transient; >1700 K during reflood
- Significant melting and oxidation of upper tie plate occurred during reflood
- Material transport to upper end box occurred during reflood

Limited fuel relocation occurred

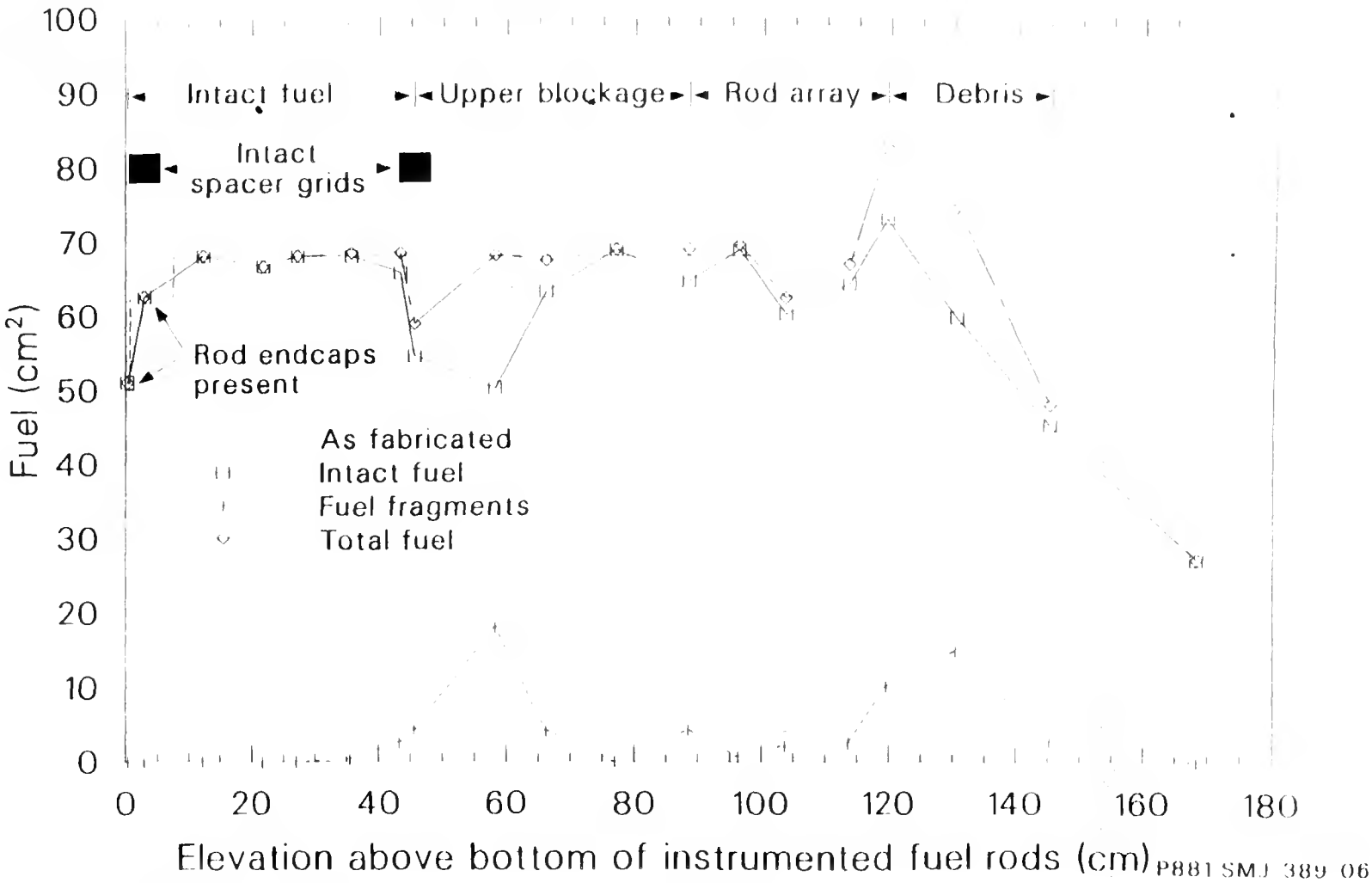

P881 SMJ 389 06

Extensive zircaloy melting in upper bundle

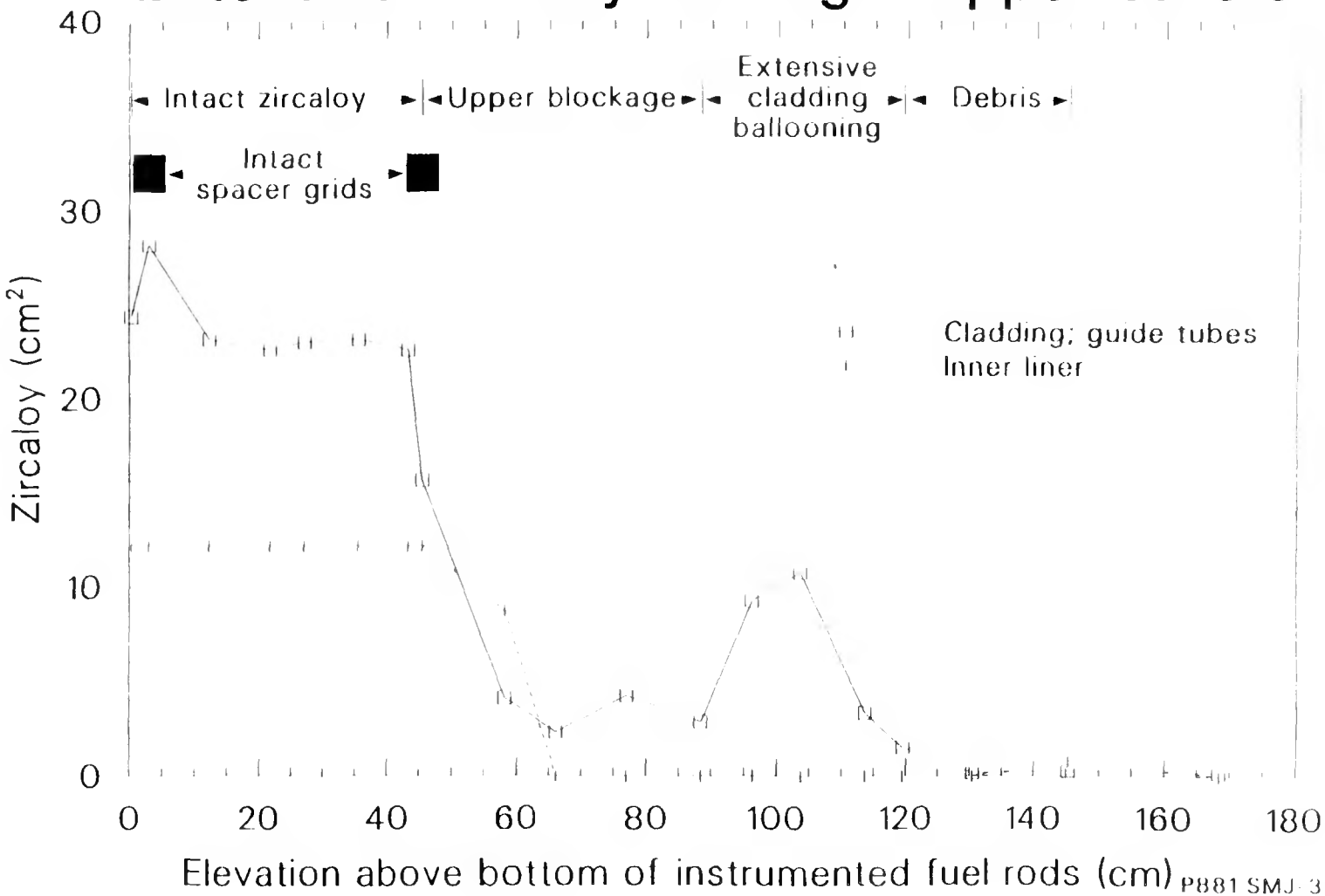

P881 SMJ-389-07

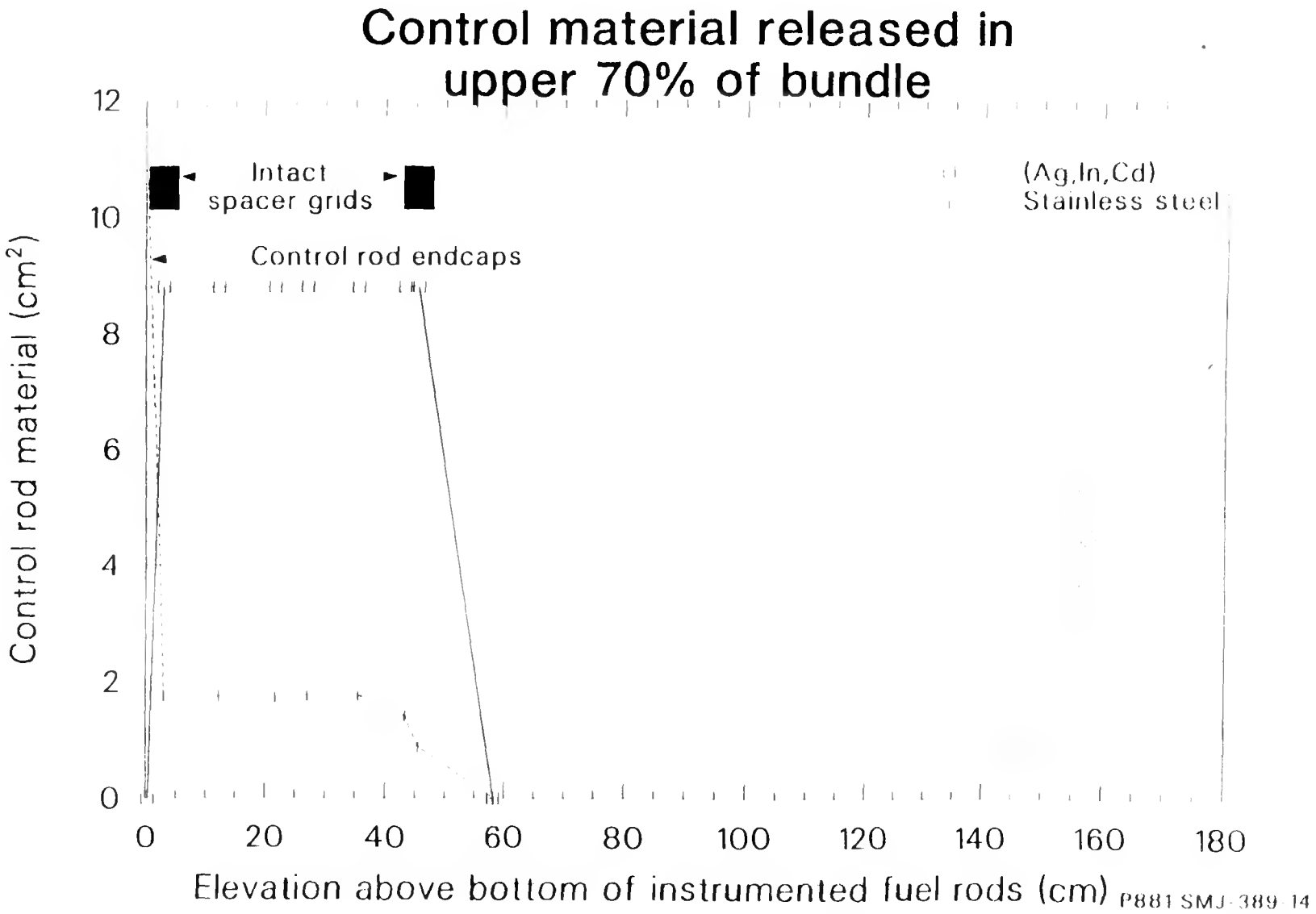
Control material released in upper 70% of bundle
Intact spacer grids
Control rod endcaps
(Ag,In,Cd)
Stainless steel
Control rod material (cm²)
0
2
4
6
8
10
12
0
20
40
60
80
100
120
140
160
180
Elevation above bottom of instrumented fuel rods (cm)
P881 SMJ-389-14

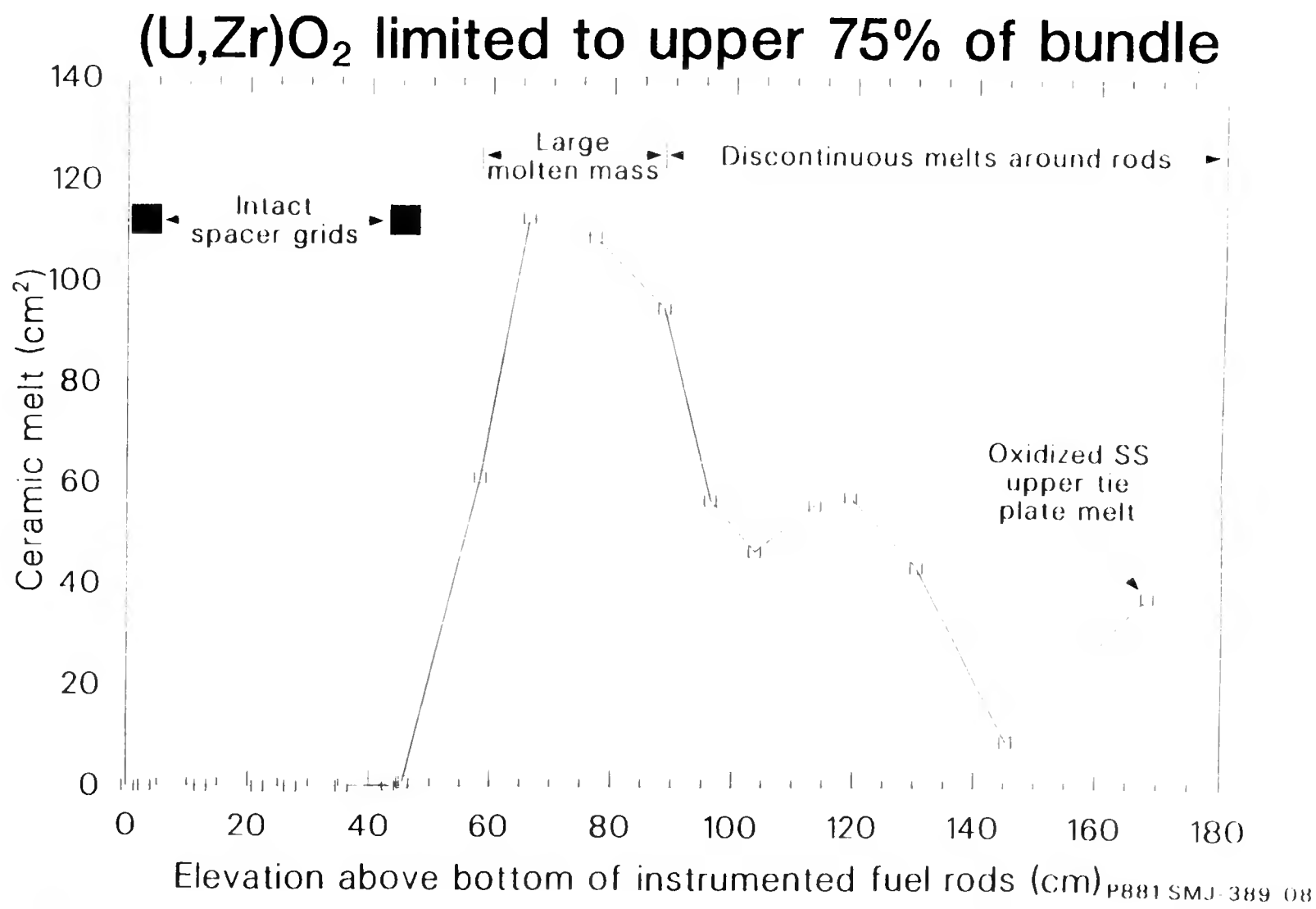
(U,Zr)O2 limited to upper 75% of bundle
Large molten mass
Discontinuous melts around rods
Intact spacer grids
Oxidized SS upper tie plate melt
Ceramic melt (cm2)
Elevation above bottom of instrumented fuel rods (cm)
P881 SMJ-389 08

Eutectic metallic melt/fuel debris distributed above remaining spacer grids

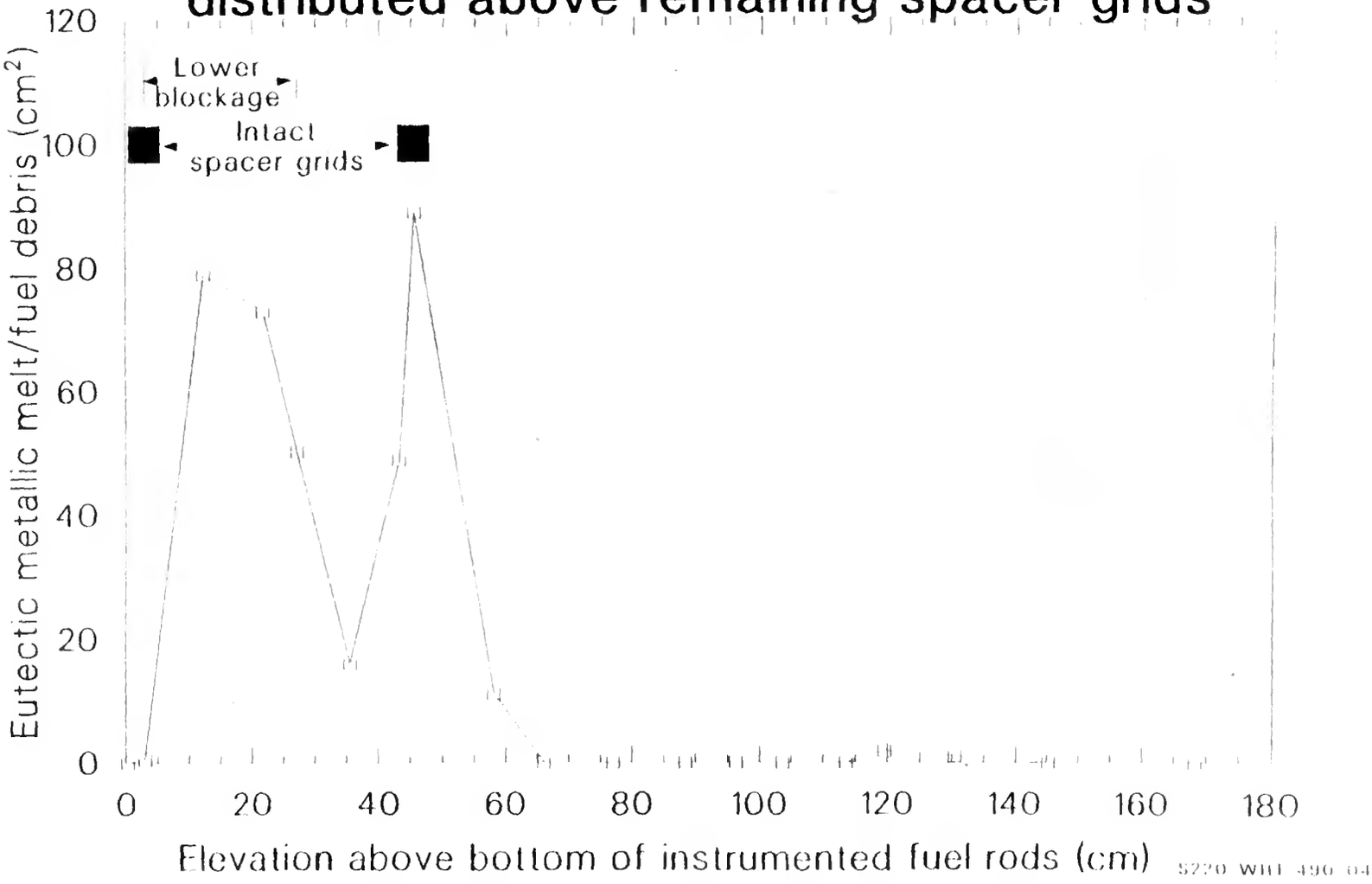

Small amounts of metallic melt throughout bundle

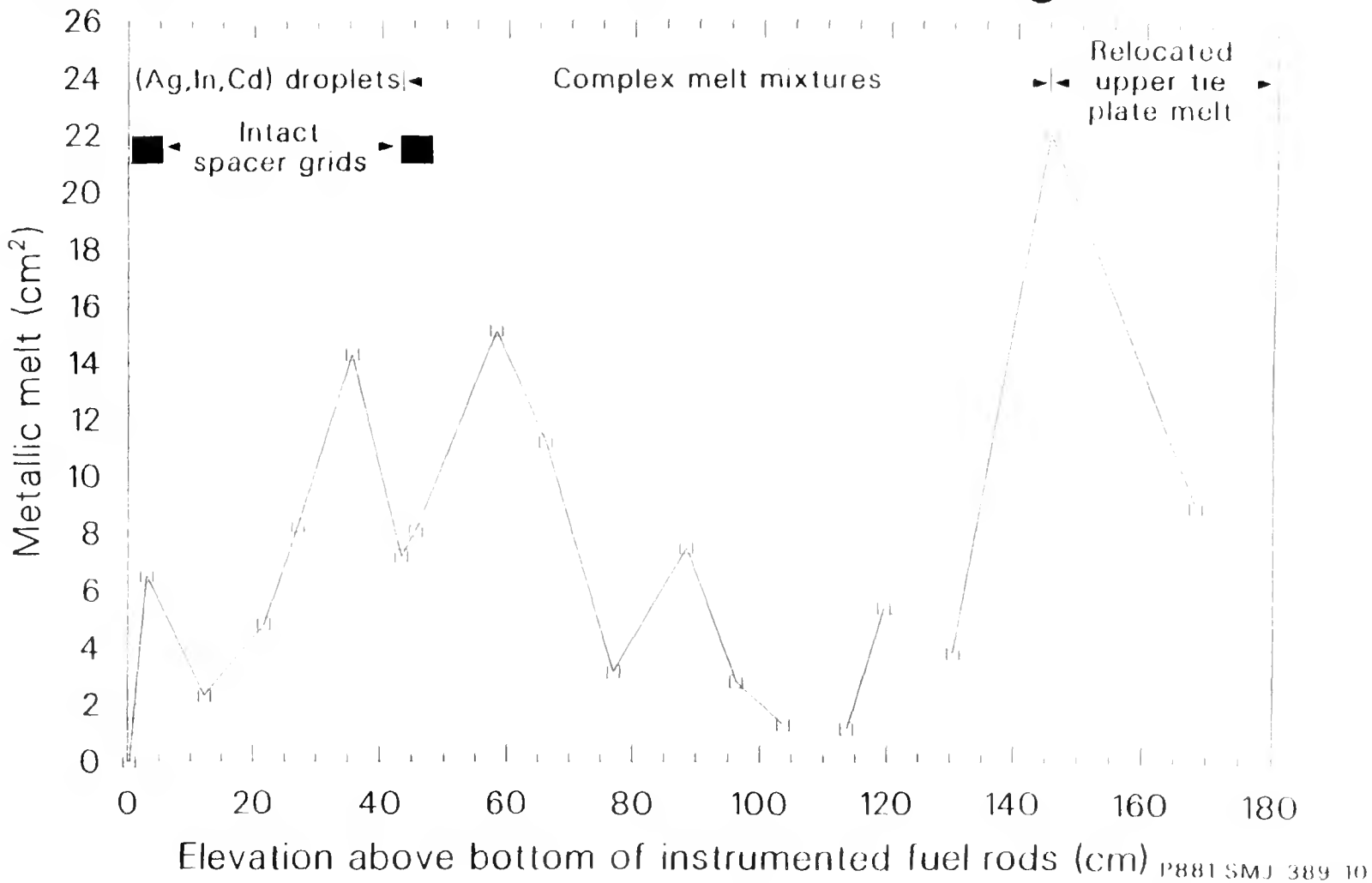

Melt penetrated into insulation where inner liner melted

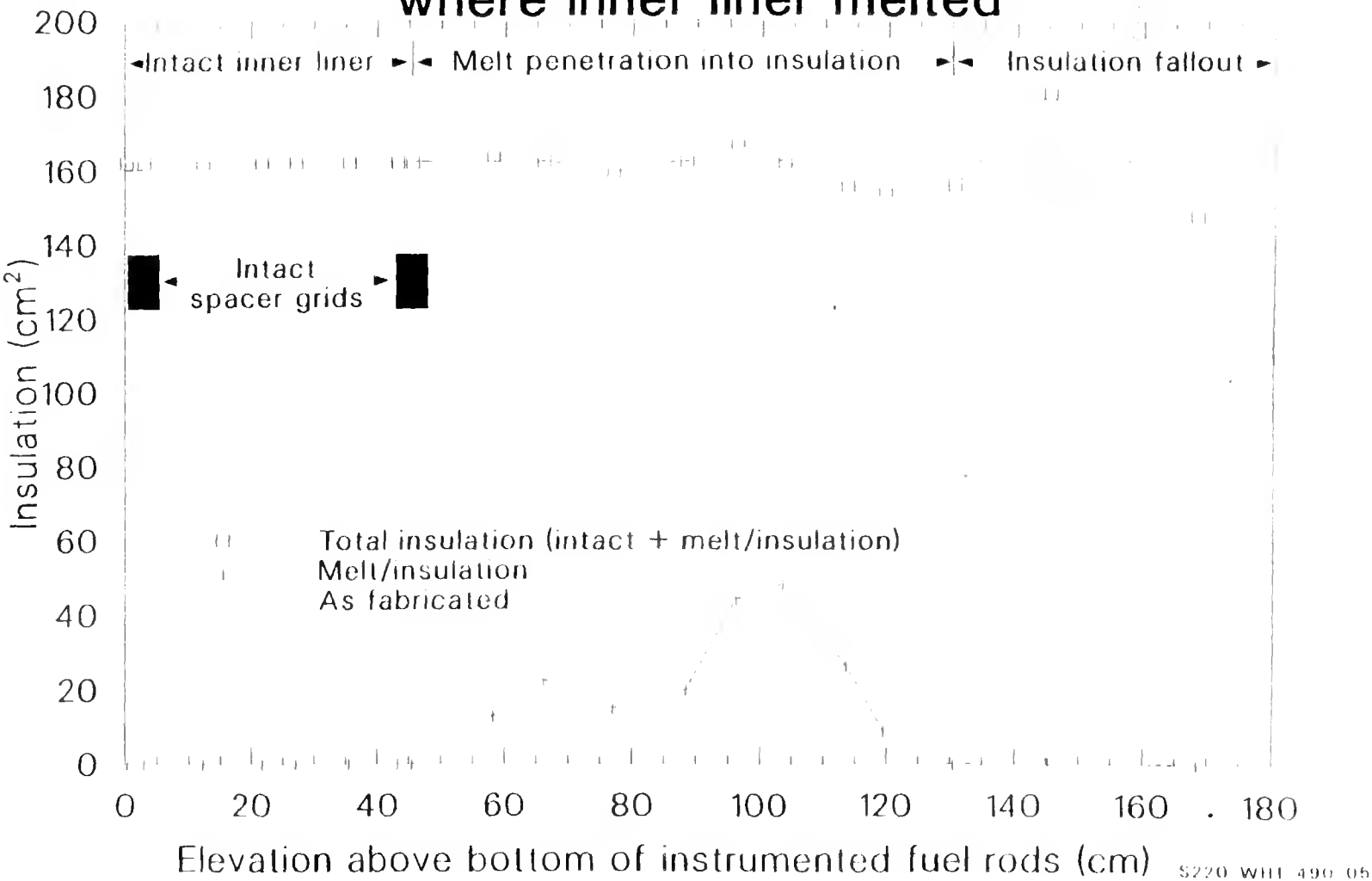

Complete flow blockage did not occur in LP-FP-2.

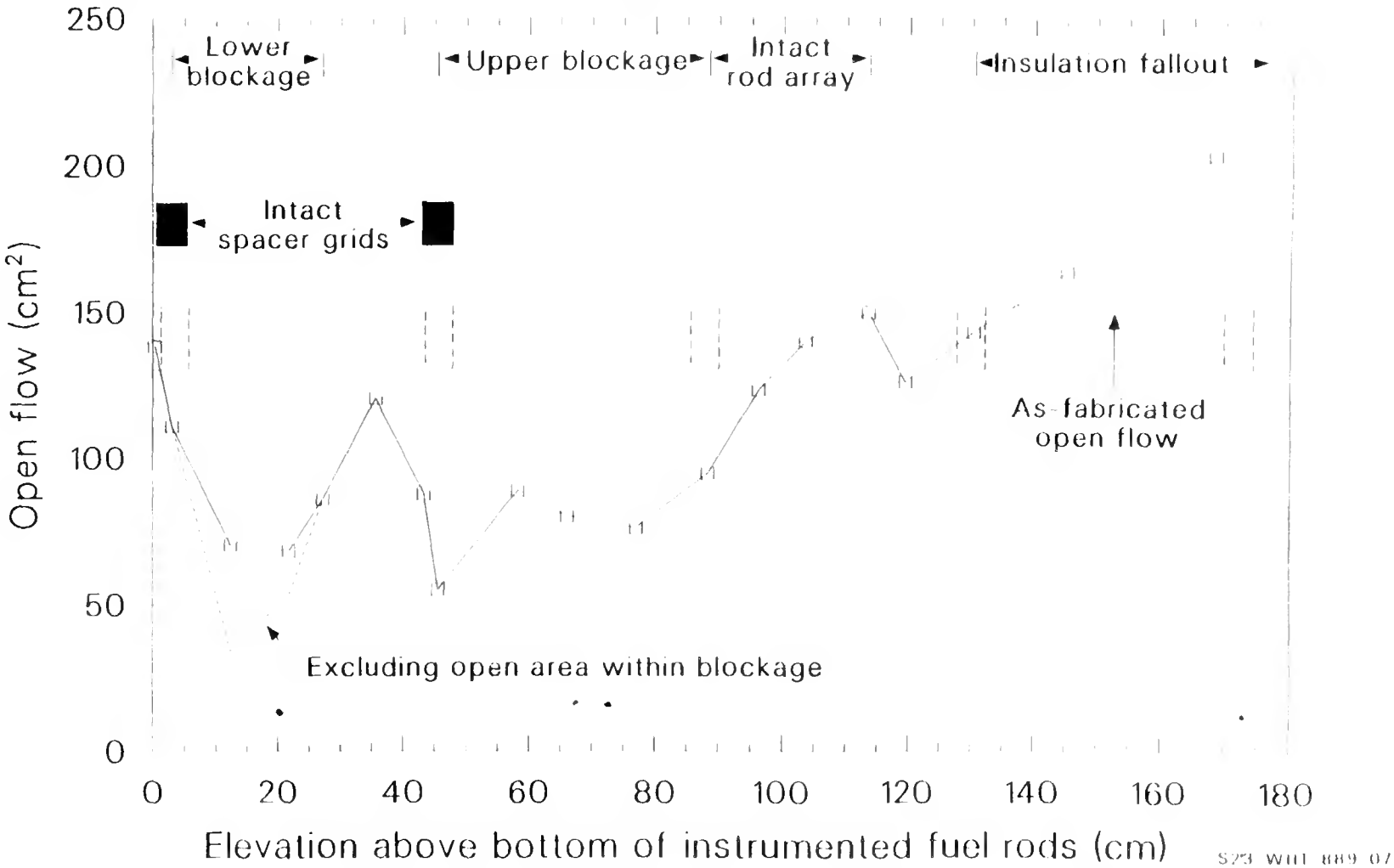

LP-FP-2 Component Integral Data

Material	Pretest cm^3	Lower Limit cm^3	Nominal cm^3	Upper Limit cm^3
Fuel				
Intact		8919 (79%)	10025 (89%)	11133 (99%)
Fuel fragments		495 (4%)	688 (6%)	908 (8%)
(Total)	11273	9414 (84%)	10713 (95%)	12041 (107%)
Zircaloy				
Cladding	4163	1363 (33%)	1575 (38%)	1806 (43%)
Liner	2207	758 (34%)	767 (35%)	776 (35%)
Control Material				
Ag,In,Cd	1475	386 (26%)	442 (30%)	498 (34%)
Stainless Steel	319	88 (28%)	88 (28%)	88 (28%)
Spacer Grid	366	124 (34%)	126 (34%)	129 (35%)
Insulation				
Intact		25974 (91%)	27251 (95%)	28528 (100%)
Interacted		1495 (5%)	1760 (6%)	2024 (7%)
(Total)	28585	27469 (96%)	29011 (101%)	30552 (107%)

LP-FP-2 Melt and Debris Integral Data

Material	Lower limit cm^3	Nominal cm^3	Upper Limit cm^3
Ceramic melt	6070	6744	7418
Metallic melt	1181	1389	1598
Eutectic metallic melt/ fuel debris	2517	2796	3076
Miscellaneous debris	10	20	30

Uranium Mass Balance in LP-FP-2

Location	Low (g)	Nominal (g)	Upper (g)
Ceramic melt	1.5E4 (14%) *	1.8E4 (15%) *	2.2E4 (16%) *
Eutectic melt/fuel debris	2.1E3 (2%)	2.3E3 (2%)	2.6E3 (2%)
Metallic melt	3.8E2 (0.3%)	9.6E2 (1%)	2.1E3 (2%)
Intact fuel	8.2E4 (79%)	9.2E4 (77%)	1.0E5 (74%)
Fuel fragments	4.5E3 (4%)	6.3E3 (5%)	8.3E3 (6%)
Posttest total	1.0E5	1.2E5	1.4E5
Pretest total	1.0E5	1.0E5	1.0E5
Δ%	0%	20%	40%

* % are normalized to posttest total

S220 WHT 490 08

Zirconium Mass Balance in LP-FP-2

Location	Low (g)	Nominal (g)	Upper (g)
Ceramic melt	9.1E3 (28%) *	1.2E4 (29%) *	1.6E4 (32%) *
Eutectic melt/fuel debris	4.9E3 (15%)	5.4E3 (13%)	6.0E3 (12%)
Metallic melt	1.5E3 (5%)	3.0E3 (7%)	5.2E3 (10%)
Melt/insulation	4.1E3 (13%)	5.6E3 (14%)	6.9E3 (14%)
Intact cladding and liner	1.3E4 (40%)	1.5E4 (37%)	1.6E4 (32%)
Posttest total	3.3E4	4.1E4	5.0E4
Pretest total	4.1E4	4.1E4	4.1E4
Δ%	-20%	0%	22%

* % are normalized to posttest total

U, Zr mass balances indicate material distribution measurements are reasonably accurate.

Uranium

- Nominal estimate overpredicts total U content by 20%
- Low estimate for U distribution agrees with total U content
  - fuel cracking may have contributed to overprediction of intact fuel for nominal case
- Approximately 85% of fuel was intact or fragmented; ~15% was liquefied

Zirconium

- Nominal estimate agrees with total Zr content
- Nominally 37% of cladding and liner remained intact; greatest amount of molten Zr was in ceramic region (~29%)

Low temperature liquefaction of metallic components occurred in LP-FP-2.

- All control rods ruptured near bottom of upper blockage
  - approximately 2/3 of bundle inventory (10 kg) was molten and relocated

- Metallic melts containing control material interacted with zircaloy, stainless steel, and Inconel

Ag-Zr Interactions Liquefied Zircaloy and Formed Lower Blockage

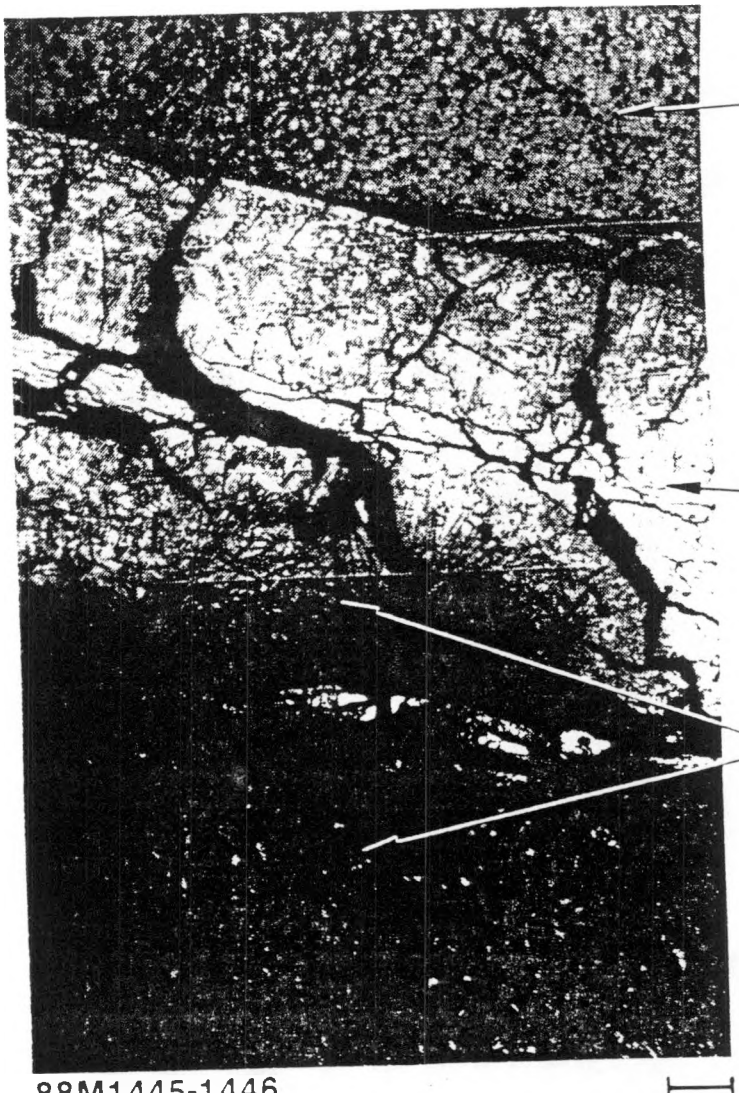

88M1445-1446

100 μm

8-4570

Stainless Steel Liquefaction Contributed to Formation of Lower Blockage

88M1386-1388

Eutectic Interactions Liquefied Stainless Steel Below Its Melting Point

88M643

200 μm

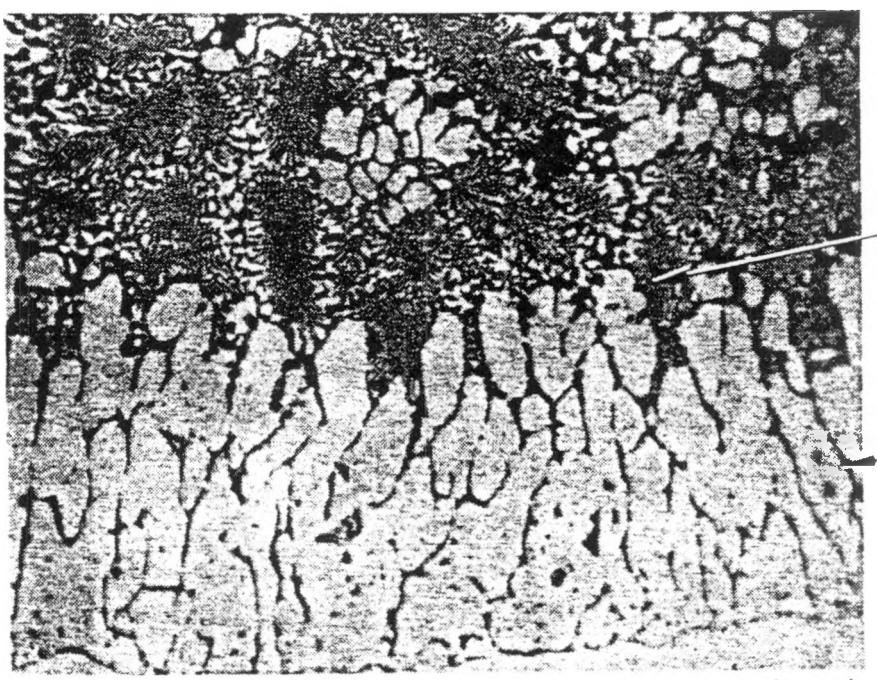

88M644

20 μm

8-4582

Zr-Ni Eutectic Interactions Liquefied Spacer Grids

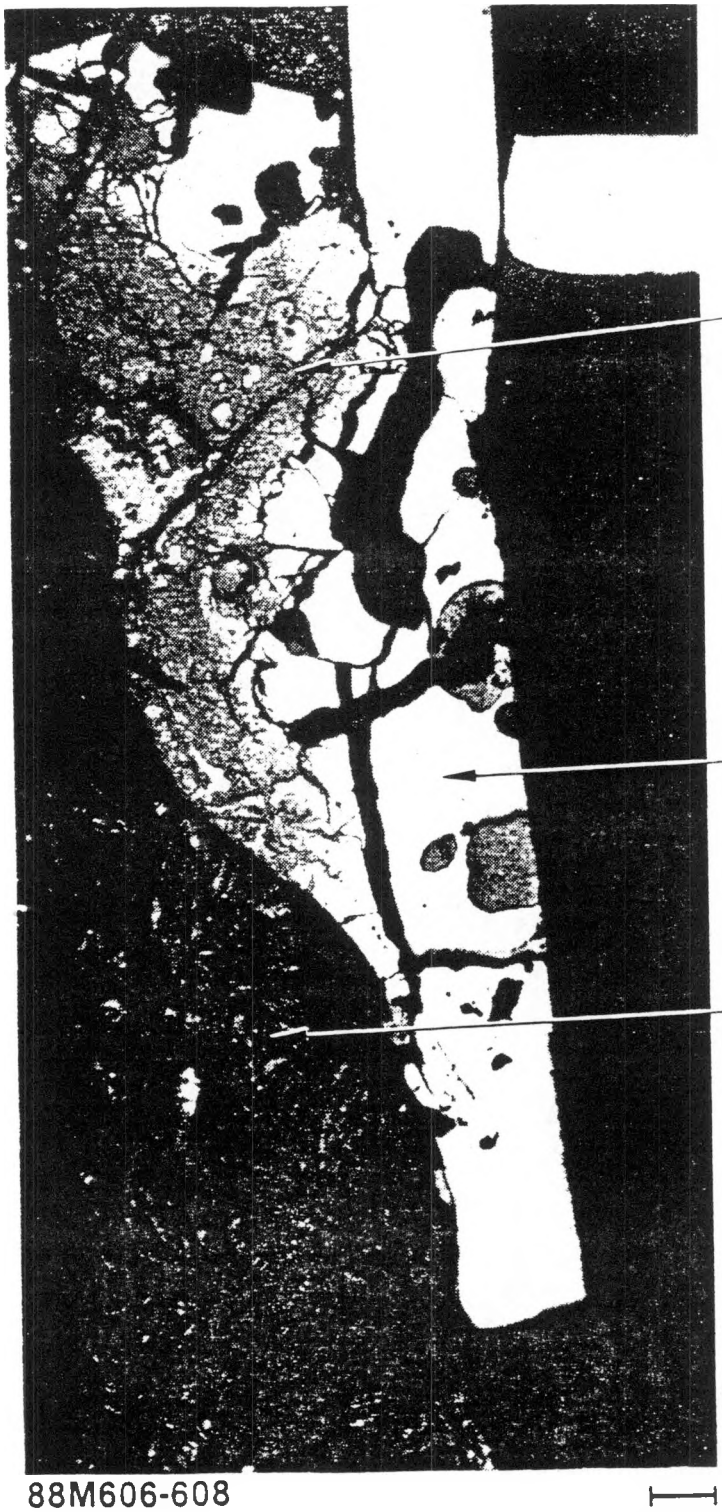

Fuel grain boundary separation and fragmentation occurred in LP-FP-2.

- Metallic melts caused fuel grain boundary separation and fragmentation
- Additional fuel fragmentation probably occurred from thermal shock at reflood

Metallic Melts Caused Grain Boundary Separation

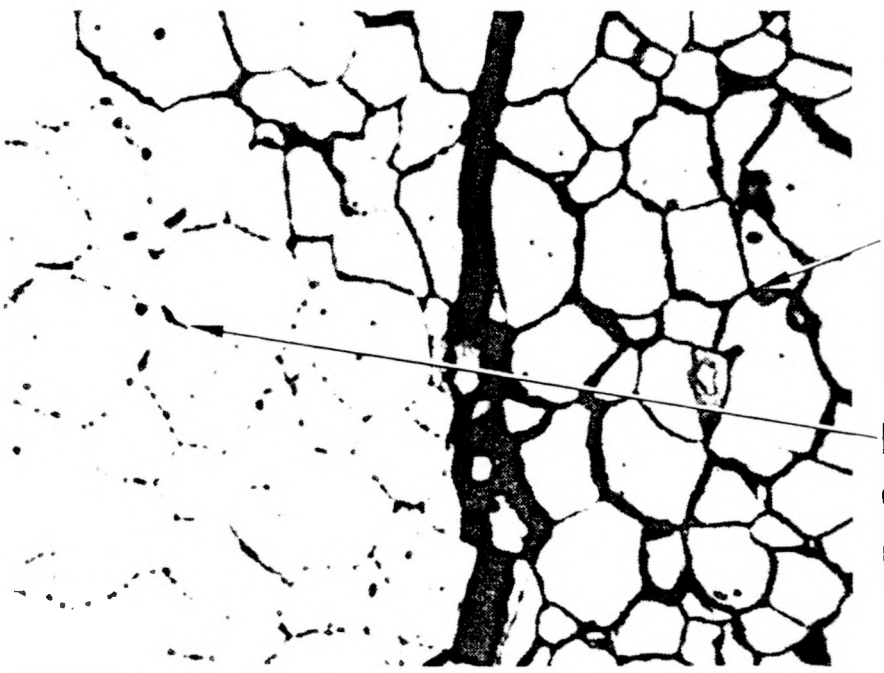

8-4585

Fragmentation May Have Enhanced Fuel Liquefaction

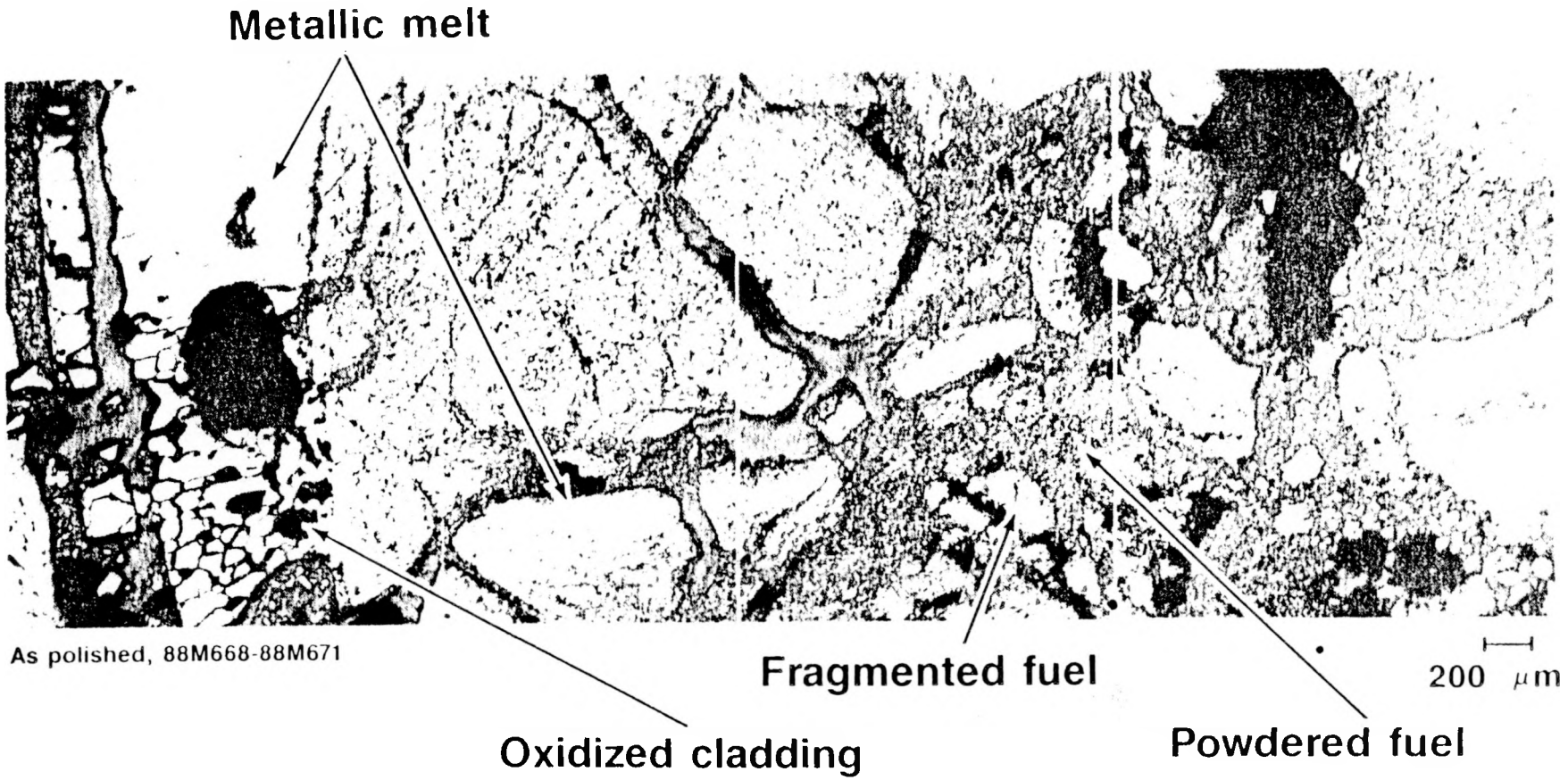

9 0807

Both Fuel Liquefaction and Melting Occurred in LP-FP-2

- Some fuel liquefaction occurred as a result of Fe-oxides contacting exposed fuel
- Some fuel melting occurred in center of $(U,Zr)O_2$ upper blockage

Fe-oxides Caused Fuel Liquefaction

Grain growth

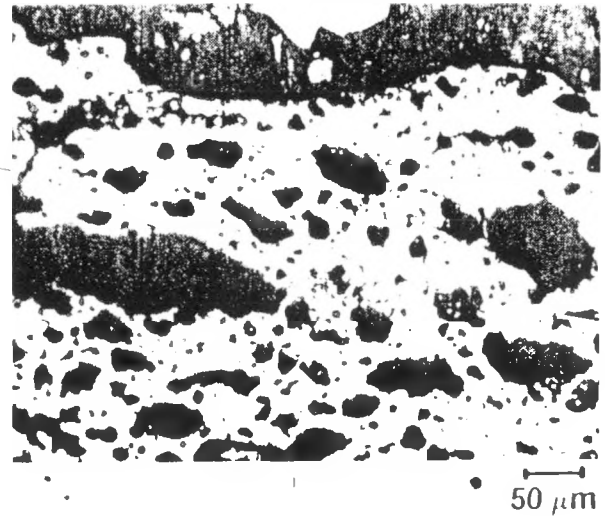

Porous fuel without grains at edge of pellet

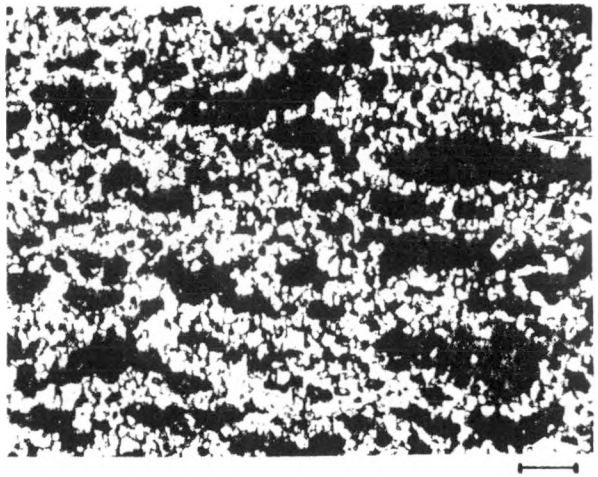

Porous fuel with grains

0 0366

$(U,Zr)O_2$ Was Hot Enough to Melt Fuel in Some Places

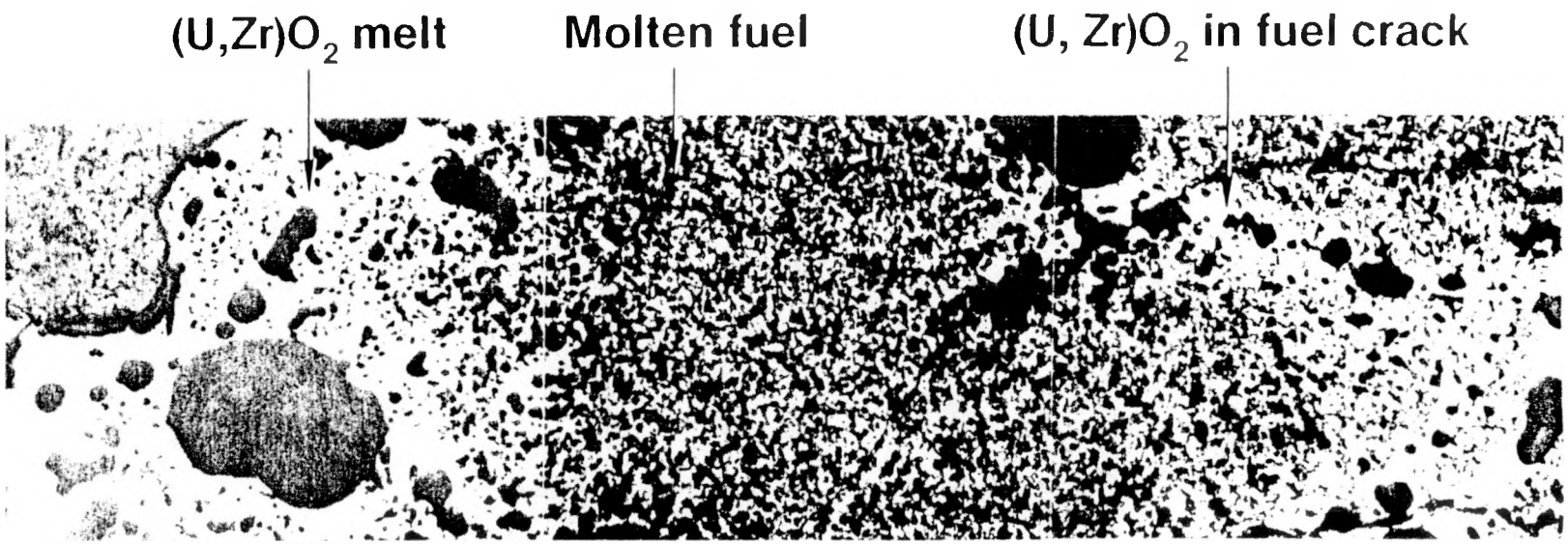

88,824-826 as polished

200 μm

0 0368

Best Estimate Hydrogen Generation in LP-FP-2

	H_2 (g)		
Zircaloy Oxidation	Lower	Nominal	Upper
Upper limit on zircaloy oxidation = 1226 g			
Unoxidized Zr in eutectic metallic melt	-197	-118	-54
Unoxidized Zr in melt/insulation	-226	-114	-42
Unoxidized Zr in metallic melts	-228	-132	-66
Total hydrogen	575	862	1064
Non-Zircaloy Oxidation			
Oxidation of SS upper tie plate	55	103	155
Oxidation of molten SS cladding	20	40	60
Oxidation of molten spacer grid	9	20	31
Total hydrogen	80	163	246
Total hydrogen generation	655	1025	1310

5220 WH1 490 11

Approximate Distribution of Hydrogen Generation in LP-FP-2

	H_2 (g)		
	Lower	Nominal	Upper
Oxidized ZrO_2 cladding shells	36	63	93
Eutectic metallic melt	54	118	197
Ceramic melt in large blockage (<0.92 m)	225	327	471
Ceramic melt above large blockage (>0.92 m)	175	195	214
Melt/insulation	56	133	229
Total from zirconium	546	836	1204

Independent methods of estimating total H_2 generation are in good agreement.

- Two alternative PIE methods
  - subtraction of unoxidized Zr from oxidation upper limit provides best estimate (nominally 862 g; range 575-1064 g)
  - addition of oxidized Zr in various types of materials provides distribution data (nominally 836 g; range 546-1204 g)

- Oxidation of stainless steel and Inconel components was added to zircaloy oxidation (163 $\pm$ 83 g)

- Best-estimate of hydrogen generation from PIE is 1025 g H_2 (58% equivalent zircaloy in bundle)
  - agrees with 1024 g nominally estimated to be in BST & PCS

Hydrogen partitioning is consistent with amounts in BST and PCS.

- Nominally 181 g came from oxidized cladding shells and relocated material in lower blockage
  - good agreement with 205 ± 11 g in BST estimated to have occurred during transient

- Nominally 818 g came from ceramic melt, melt/insulation regions and non-zircaloy components
  - good agreement with 819 ± 364 g estimated in PCS following reflood

Fuel Grain Size Measurements

- Average grain size in non grain growth regions = 14 μM
  2σ = 4 μm (107 measurements)

- Average grain size in grain growth regions (center of fuel pellet) = 27 μm
  2σ = 17 μm (30 measurements)

Peak bundle temperatures were estimated from PIE.

- Below second spacer grid (<0.4 m), temperatures were based on zircaloy microstructure
- At second spacer grid, temperatures were based on partial liquefaction of Inconel spacer grid
- In the ceramic upper blockage region (0.6-0.9 m), weighted temperatures for various regions were used
- Above the upper blockage, temperature ranges were based on limited data

Ceramic melt temperatures were based on weighted values.

(J Cross Section-0.77 m)

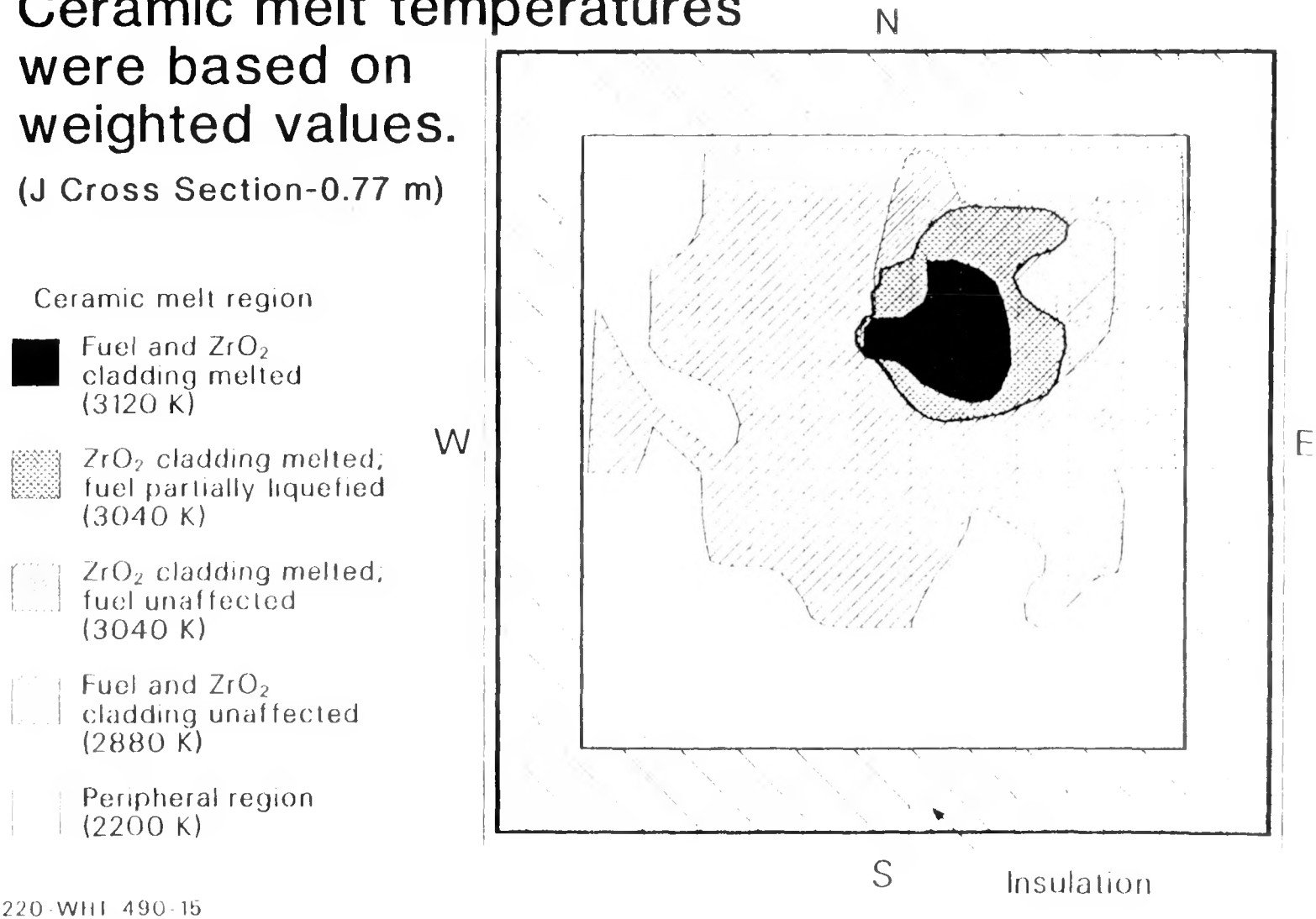

S220-WHT-490-15

Postirradiation examinations provided data on bundle temperatures after thermocouple failure.

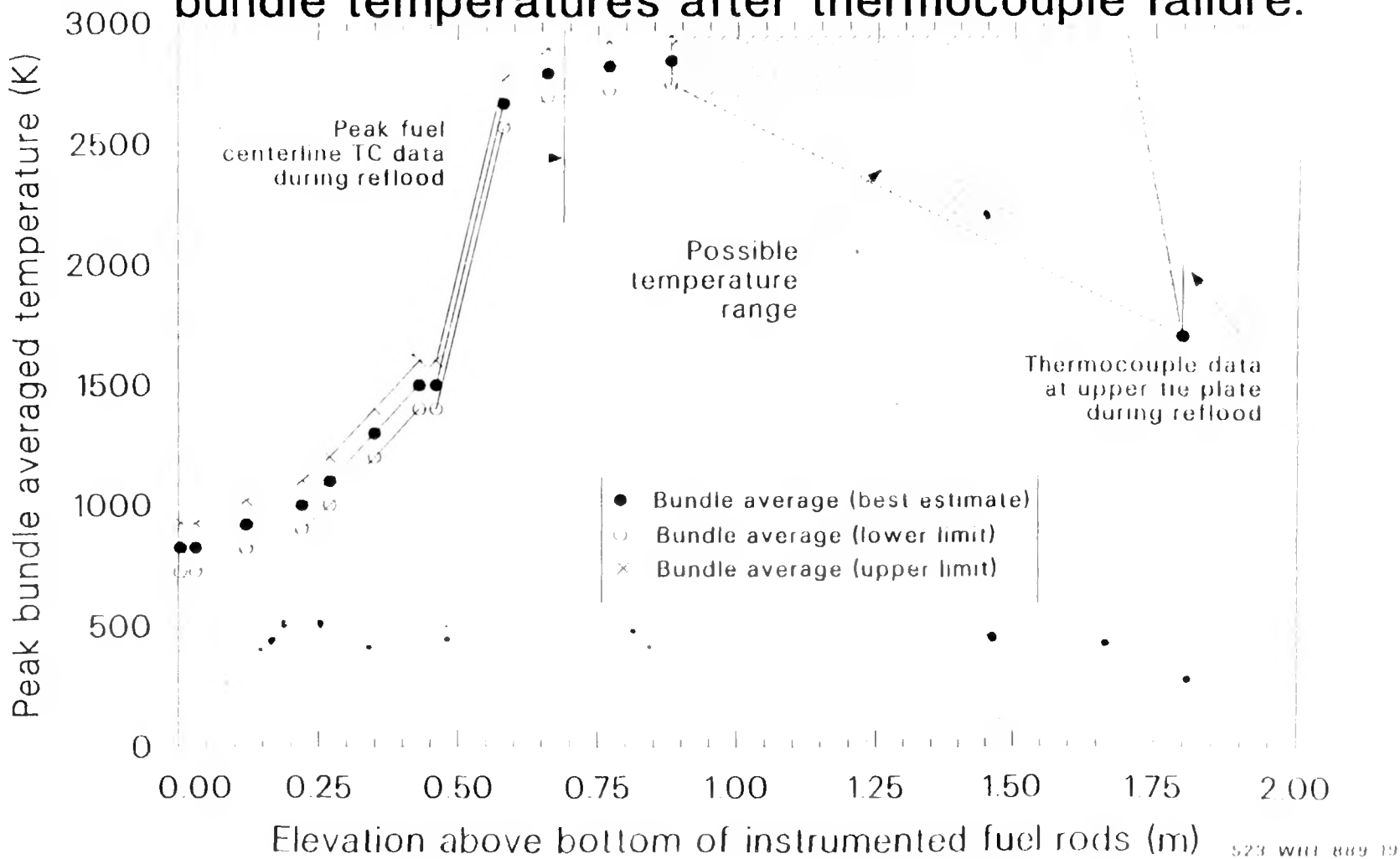

Summary of Retained Fission Product Analyses

- Initial fission product inventories generally in good agreement with ORIGEN2
- Large variations in radionuclide content were observed among seemingly similar samples
- No correlation between fission product release and peak temperature in melts
  - morphology and time at temperature probably affected release
- Cs was generally retained in intact and fragmented fuel, but significant releases (60-70%) occurred in partially liquefied or molten fuel
- I was retained in intact fuel, but significantly released in fragmented, liquefied, and molten fuel (50-80%)
- Cs and I release in the ceramic melt regions ranged from 50-100%
- Ag, In, Cs, I were transported and deposited on upper tie plate

Summary of Significant Results from Postirradiation Examinations of LP-FP-2

Distribution of fuel and control materials

- Stratification of material similar to TMI and SFD (metallic melts, ceramic melt, debris bed)
- Spacer grids impeded material relocation, resulting in greatest flow blockages (78-86%)
- Upward material relocation to the upper end box region occurred during reflood
- Approximately 15% of the fuel was liquefied
- Approximately 63% of zircaloy cladding & liner liquefied
- Approximately 70% of the control rod alloy (Ag,In,Cd) was released to the bundle

Summary of Significant Results (cont.)

Metallurgical and chemical form of materials

- Ag-Zr interactions resulted in significant zircaloy liquefaction above ~1400 K
- Zr-Ni and Zr-Fe interactions resulted in significant liquefaction of Inconel spacer grids and stainless steel cladding above ~1450 K
- Control rod failure resulted in the liquefaction of unoxidized zircaloy in the upper bundle from Ag-Zr interactions
  - these liquefied materials relocated to form lower blockage
- Fuel grain boundary separation was enhanced adjacent to metallic melts, suggesting localized fuel reduction on grain boundaries
- Very little grain growth occurred, with most fuel retaining as-fabricated grain size of 14 μm

Summary of Significant Results (cont.)

Metallurgical and chemical form of materials(continued)

- Total hydrogen generation nominally estimated to be 1025 g H_2 (58% equivalent zircaloy in bundle)
  - agrees with 1024 g nominally estimated to be in BST and PCS

- Oxidation partitioning indicates 181 g H_2 were generated during the transient and 818 g H_2 were released upon reflood
  - good agreement with estimated amounts of 205 in BST (transient release) and 819 in PCS (reflood release)

Summary of Significant Results
(continued)

Maximum temperatures throughout the fuel bundle

- Localized peak temperatures exceeded fuel melting (>3120 K), however peak bundle averaged temperatures in the ceramic melt region were approximately 2700-2900 K

- Temperatures exceeded 1700 K at the upper tie plate during reflood

Summary of Significant Results
(continued)

Fission product distribution in specific materials

- Cs and I were retained within intact fuel, but large releases were measured from ceramic melt regions
- Fission product release in melts affected by morphology and time at temperature
- Ag, In, Cs, I transported and deposited on upper tie plate